Exploiting Secondary Electrons in Transmission Electron Microscopy for 3D Characterization of Nanoparticle Morphologies

Evgenii Vlasov

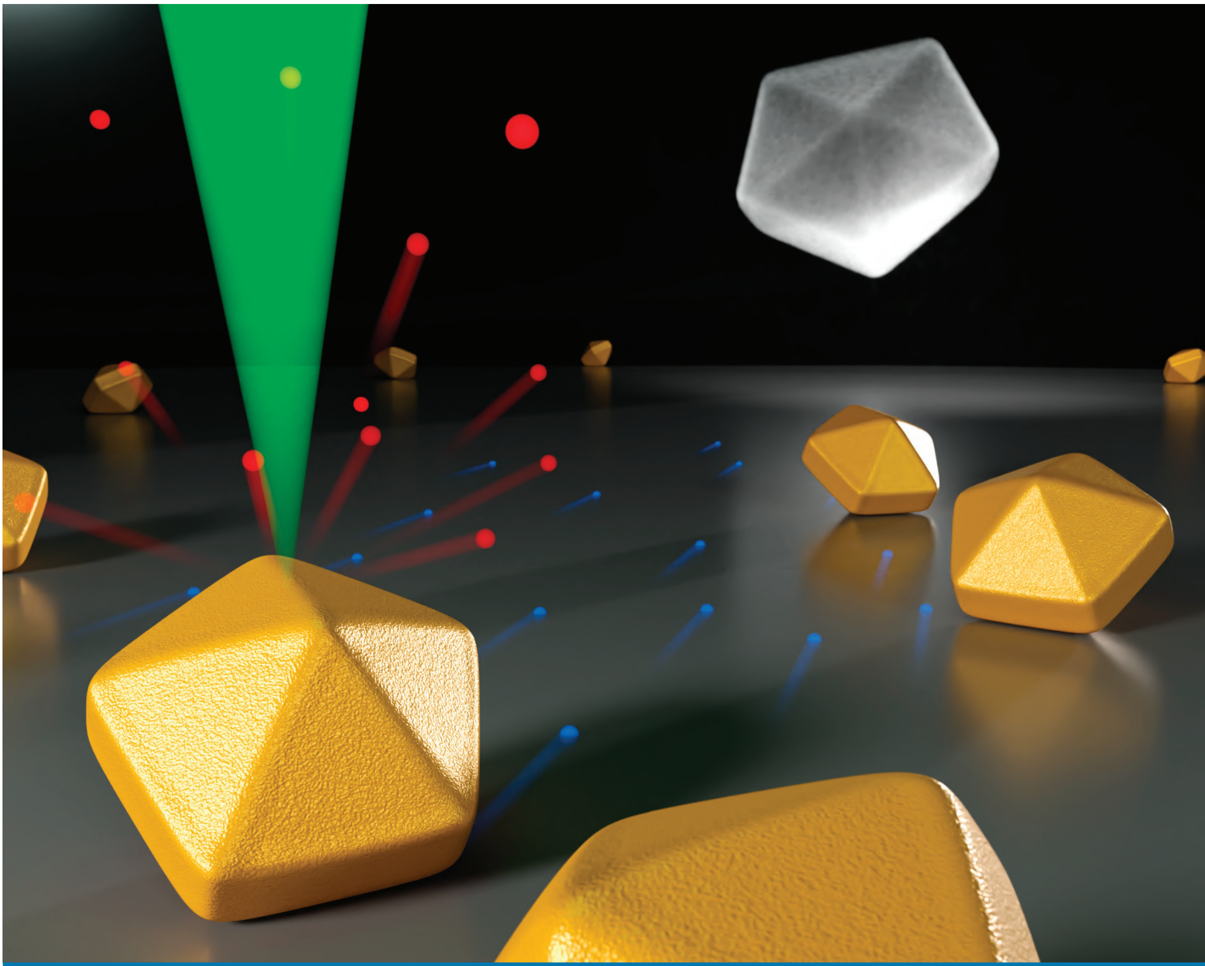

Supervisor **Prof. Dr. Sara Bals & Prof. Dr. Johan Verbeeck**

Thesis submitted for the degree of Doctor of Science: Physics
Faculty of Science | Antwerp, 2024

University
of Antwerp

University
of Antwerp

Faculty of Science

Exploiting Secondary Electrons in Transmission Electron Microscopy for 3D Characterization of Nanoparticle Morphologies

Thesis submitted in fulfilment of the requirements for the degree of
doctor in Physics
at the University of Antwerp

Evgenii Vlasov

Supervisors
Prof. Dr. S. Bals
Prof. Dr. J. Verbeeck

Antwerpen, 2024

Jury

Chair
Prof. Dr. S. Cambré, University of Antwerp, Belgium

Supervisors
Prof. Dr. S. Bals, University of Antwerp, Belgium
Prof. Dr. J. Verbeeck, University of Antwerp, Belgium

Members
Prof. Dr. J. Batenburg, Centrum Wiskunde & Informatica, The Netherlands; Leiden Institute of Advanced Computer Science, The Netherlands
Prof. Dr. Leopoldo Molina-Luna, Technische Universität Darmstadt, Germany
Prof. Dr. Nick van Remortel, University of Antwerp, Belgium

Contact
Evgenii Vlasov

University of Antwerp
Faculty of Science
EMAT
Groenenborgerlaan 171, 2020 Antwerpen, België
evgenii.vlasov@uantwerpen.be

Dutch title:

Gebruik van secundaire elektronen in transmissie-elektronenmicroscopie voor 3D-karakterisering van de morfologie van nanodeeltjes

Summary

In past decades, electron tomography (ET) has become a powerful tool for determining the three-dimensional (3D) structure of nanomaterials in transmission electron microscopy (TEM). ET enables 3D characterization of a variety of nanomaterials in different fields, such as life sciences, chemistry, solid-state physics, and materials science down to atomic resolution. However, the acquisition of a conventional tilt series for ET is a time-consuming process and thus cannot capture fast transformations of materials in realistic conditions. Moreover, only a limited number of nanoparticles (NPs) can be investigated, hampering a general understanding of the average properties of the material. Even though current state-of-the-art approaches allow for significant acceleration of the acquisition process, ET *in situ* heating experiments remain challenging, since the specimen needs to be quenched to room temperature to avoid changes of the NPs during the acquisition. Therefore, alternative characterization techniques that allow for high-resolution characterization of the surface structure without the need to acquire a full tilt series in ET are required which would enable a more time-efficient investigation with better statistical value and more representative *in situ* experiments. The aim of this PhD work is to find alternative techniques for the characterization of the morphology of NPs to improve the throughput and temporal resolution of ET. This challenge is approached in the following chapters:

Chapter 1 gives a brief introduction to nanotechnology and nanomaterials focusing on properties and applications of plasmonic NPs. Next, the chapter provides the conceptual background for TEM and covers practical aspects and state-of-the-art ET. Finally, the main limitations of ET for the 3D characterization of the nanomaterials are considered, giving rise to the motivation for the research presented in this thesis.

Chapter 2 shift the focus to the application of secondary electron (SE) imaging in scanning TEM (STEM), showing its potential to retrieve the surface morphology of the nanostructures. Given the poor availability of SE imaging in modern STEM instruments, the secondary electron electron beam-induced current (SEEBIC) is introduced and proposed as an alternative technique to detect SEs. Finally, recent advancements in SEEBIC and its practical aspects are discussed.

For the implementation of SEEBIC imaging of the surface morphology of the nanostructures, in **Chapter 3** I formulate the main requirements for SEEBIC experimental setup and focus on the design and characterization of an optimized transimpedance amplifier. Here detailed discussion on stability consideration and noise performance as well as design choices are presented. The proposed design was used throughout this PhD thesis and made possible experiments described in the following chapters.

Chapter 4 is concerned with the development of SEEBIC as an alternative way for the visualization of the 3D structure of NPs. The time- and dose efficiency of SEEBIC

are tested in comparison with ET and superior spatial resolution is shown compared to SEM. Finally, contrast artifacts arising in SEEBIC images are described, and their origin is discussed. The origin of contrast artifacts is further explored in **Chapter 5**, where a physical model that includes the angle-dependent escape rate of SEs and their contribution to the SEEBIC signal is proposed.

Obtained in the previous chapters findings allowed us to further push the throughput of the SEEBIC imaging. **Chapter 6** introduces a high-throughput methodology that combines images acquired by SEEBIC with quantitative image analysis to retrieve information about the helicity of hundreds of NPs in a time-efficient manner. Here we demonstrate that SEEBIC imaging overcomes the limitation of ET providing a general understanding of the connection between structure and chiroptical properties. Based on experimental observations and previous discussions, we propose a model of how morphologies of single nanorods translate to an average morphology of the ensemble.

In **Chapter 7** I present the overall outcome of this PhD work, and in **Chapter 8** I provide a perspective on the future application of SEEBIC for characterization of the 3D structure of nanomaterials.

Samenvatting

In de afgelopen decennia is elektronentomografie (ET) een krachtig hulpmiddel geworden voor het bepalen van de driedimensionale (3D) structuur van nanomaterialen in transmissie elektronenmicroscopie (TEM). ET maakt 3D-karakterisering van een verscheidenheid aan nanomaterialen op verschillende gebieden mogelijk, zoals biowetenschappen, chemie, vastestoffysica en materiaalkunde tot op atomaire resolutie. De acquisitie van een conventionele kantelreeks voor ET is echter een tijdrovend proces en kan dus geen snelle transformaties van materialen in realistische omstandigheden vastleggen. Bovendien kan slechts een beperkt aantal nanodeeltjes onderzocht worden, wat een algemeen begrip van de gemiddelde eigenschappen van het materiaal in de weg staat. Hoewel de huidige state-of-the-art benaderingen een aanzienlijke versnelling van het acquisitieproces mogelijk maken, blijven ET textit verhittingsexperimenten een uitdaging, omdat het monster moet worden afgekoeld tot kamertemperatuur om veranderingen van de nanodeeltjes tijdens de acquisitie te voorkomen. Daarom zijn er alternatieve karakteriseringstechnieken nodig die een karakterisering met hoge resolutie van de oppervlaktestructuur mogelijk maken zonder de noodzaak om een volledige kantelreeks in ET te verwerven. Dit zou een tijdsefficiënter onderzoek met een betere statistische waarde en meer representatieve experimenten met ET in situ mogelijk maken. Het doel van dit PhD-werk is om alternatieve technieken te vinden voor de karakterisering van de morfologie van NP's om de verwerkingscapaciteit en temporele resolutie van ET te verbeteren. Dit probleem wordt benaderd in de volgende hoofdstukken:

Hoofdstuk 1 geeft een korte inleiding in nanotechnologie en nanomaterialen met de nadruk op de eigenschappen en toepassingen van plasmonische nanodeeltjes (NP's). Vervolgens bevat het hoofdstuk de conceptuele achtergrond voor TEM en worden praktische aspecten en state-of-the-art ET besproken. Tot slot worden de belangrijkste beperkingen van ET voor de 3D karakterisering van nanomaterialen bekeken, wat aanleiding geeft tot de motivatie voor het onderzoek dat in dit proefschrift wordt gepresenteerd.

Hoofdstuk 2 verschuift de aandacht naar de toepassing van secundaire elektronen (SE) beeldvorming in scanning TEM (STEM). In dit hoofdstuk wordt het potentieel van deze techniek aangetoond om de oppervlaktemorfologie van de nanostructuren te achterhalen. Gezien de slechte beschikbaarheid van SE-beeldvorming in moderne STEM-instrumenten wordt de secundaire elektronenbundel-geïnduceerde stroom (SEEBIC) geïntroduceerd en voorgesteld als een alternatieve techniek om SE's te detecteren. Tot slot worden recente ontwikkelingen in SEEBIC en de praktische aspecten ervan besproken.

Voor de implementatie van SEEBIC beeldvorming om de oppervlaktemorfologie van de nanostructuren te bestuderen, formuleer ik in **Hoofdstuk 3** de belangrijkste eisen voor de SEEBIC experimentele opstelling en richt ik me op het ontwerp en de karakterisering van een geoptimaliseerde transimpedantie versterker. In dit hoofdstuk worden de stabiliteit, ruis en de ontwerpkeuzes in detail gepresenteerd. Het voorgestelde ontwerp is in deze thesis gebruikt en heeft de experimenten mogelijk gemaakt die in de volgende hoofdstukken worden beschreven.

Hoofdstuk 4 beschrijft de ontwikkeling van SEEBIC als een alternatieve manier om de 3D structuur van NP's te visualiseren. De tijd- en dosis efficiëntie van SEEBIC worden getest en vergeleken met ET. Superieure ruimtelijke resolutie wordt aangetoond in vergelijking met SEM. Tot slot worden contrastartefacten in SEEBIC-beelden beschreven en wordt hun oorsprong besproken. De oorsprong van deze contrastartefacten wordt verder onderzocht in **Hoofdstuk 5**. Hier wordt een fysisch model voorgesteld dat de hoekafhankelijke ontsnappingsnelheid van SE's en hun bijdrage aan het SEEBIC-signaal omvat.

De bevindingen uit de voorgaande hoofdstukken maakten het mogelijk om de verwerkingscapaciteit van de SEEBIC-beeldvorming te vergroten. **Hoofdstuk 6** introduceert een high-throughput methodologie die beelden opgenomen met SEEBIC combineert met kwantitatieve beeldanalyse om informatie over de heliciteit van honderden NP's op een tijd efficiënte manier te verkrijgen. Hierdoor overkomt SEEBIC de limieten van ET waardoor een algemeen begrip over de relatie tussen de morfologie en chiroptische eigenschappen kan worden bekomen. Op basis van experimentele waarnemingen en eerdere discussies wordt een model voorgesteld dat beschrijft hoe de morfologie van afzonderlijke nanorods zich vertalen naar een gemiddelde morfologie van het ensemble.

In **Hoofdstuk 7** presenteer ik het algemene resultaat van dit PhD werk en tot slot geef ik in **Hoofdstuk 8** een perspectief op de toekomstige toepassing van SEEBIC voor de karakterisering van de 3D structuur van nanomaterialen.

List of Abbreviations

2D	Two-dimensional
1D	One-dimensional
0D	Zero-dimensional
NP	Nanoparticle
LSPR	Localized surface plasmon resonance
CD	Circular dichroism
EM	Electron microscopy
TEM	Transmission electron microscopy
SEM	Scanning electron microscopy
BF	Bright field
DF	Dark field
HR-TEM	High-resolution transmission electron microscopy
STEM	Scanning transmission electron microscope
HAADF	High-angle annular dark field
ADF	Annular dark field
SE	Secondary electron
AEM	Analytical electron microscopy
EDXS	Energy-dispersive X-ray spectroscopy
EELS	Electron energy loss spectroscopy
3D	Three-dimensional
ET	Electron tomography
CT	Computed tomography
FBP	Filtered backprojection
SIRT	Simultaneous iterative reconstruction technique
EM	Expectation maximization
DART	Discrete algebraic reconstruction technique
TVM	Total variation minimization
GPA	Geometrical phase analysis
ETD	Everhart-Thornley detector
BSE	Backscattered electrons
EBIC	Electron beam induced current
EBAC	Electron beam absorbed current
SEEBIC	Secondary electron electron beam induced current
TIA	Transimpedance amplifier
PEET	Plasmon energy expansion thermometry
MEMS	Micro-electromechanical system

ROC	Rate of closure
PCB	Printed circuit board
ESF	Edge spread function
PSF	Point spread function
FWHM	Full width at half maximum
CTAC	N,N,N-Trimethylhexadecan-1-aminium chloride
BINOL	1,1′-Bi-2-naphthol
BINAMINE	1,1′-Binaphthyl-2,2′-diamine
NR	Nanorod
SfS	Shape-from-shading
SfM	Structure-from-motion
NeRF	Neural Radiance Fields

Contents

Summary **i**

Samenvatting **iii**

List of Abbreviations **v**

1 Introduction **1**

1.1 Nanotechnology and Nanomaterials 1

1.2 Electron Microscopy 5

1.2.1 Transmission Electron Microscopy 6

1.2.2 Scanning Electron Microscopy 10

1.3 Electron Tomography 12

1.4 State-of-the-art of Electron Tomography 18

1.4.1 Atomic-resolution Electron Tomography 18

1.4.2 Fast Electron Tomography 19

1.4.3 *In situ* Electron Tomography 21

2 Secondary Electron Imaging in Transmission Electron Microscopy **23**

2.1 Secondary Electron Imaging in STEM 23

2.2 Secondary Electron Induced Current 27

2.3 Practical Aspects of SEEBIC 31

2.4 Conclusions 33

3 Design of a SE Detection Setup for Use in TEM **35**

3.1 Introduction 35

3.2 TIA Design Considerations 36
3.2.1 Stability Considerations 37
3.2.2 Noise Analysis 39
3.2.3 Board Layout 42
3.3 Carrier Board Design 43
3.4 Experimental Validation of the Design 44
3.5 Outlook 45

4 Secondary Electron Electron Induced Current as a Method to Visualize the Morphology of Nanoparticles 47

4.1 Introduction 47
4.2 Materials and Methods 48
4.3 Results and Discussion 49
4.3.1 Accumulated Electron Dose Estimation 50
4.3.2 Comparison with SEM 52
4.3.3 Origin of Artifactual SEEBIC Contrast 55
4.3.4 Imaging of Dielectric and Semiconductor Materials 59
4.4 Conclusions 59

5 Physical Model of SEEBIC Topographical Contrast Formation 61

5.1 Introduction 61
5.2 Problem Statement 62
5.3 Materials and Methods 68
5.4 Results and Discussion 69
5.5 Conclusions 71
5.6 Appendix 72

6 High-throughput Morphological Helicity Quantification of Twisted and Wrinkled Gold Nanorods 75

6.1 Introduction to Chirality in Inorganic Nanoparticles 75
6.2 Growth and 3D Characterization of Chiral NP by ET 76

6.3 Motivation 79
6.4 Materials and Methods 79
6.5 Results and Discussion 81
6.5.1 Qualitative Comparison 81
6.5.2 Quantitative Comparison 84
6.6 Conclusions 95
6.7 Experimental Images Used for Analysis 95

7 General Conclusion 99

8 Outlook 101

List of Author's Contribution 115

Acknowledgements 117

Chapter 1

Introduction

This chapter introduces the background and theoretical basis for the research comprised in this thesis, including the motivation for studying nanomaterials and the relevance of electron microscopy during these investigations. The principles of electron tomography as a tool for understanding the three-dimensional structure of nanomaterials and its state-of-the-art will also be discussed. Next, the main drawbacks of electron tomography are considered, giving rise to the motivation for the research presented in this thesis.

1.1 Nanotechnology and Nanomaterials

In recent decades, significant advancements in the field of nanotechnology have been made. Nanotechnology refers to the science and technology concerned with manipulating matter at dimensions typically between 1 to 100 nanometers. At this scale, materials exhibit distinct properties that are fundamentally different from their bulk counterparts, leading to unprecedented opportunities for innovation and discovery. This has opened new avenues for designing and fabricating materials and devices with extraordinary properties and functionalities, including, e.g., enhanced mechanical strength, exceptional electrical, magnetic, and optical characteristics [1].

Central to the success and widespread application of nanotechnology is the development of nanomaterials – materials with tailored structures and properties at the nanometer level. These materials can be categorized into several types depending on the number of dimensions that are restricted to the nanometer range (**Figure 1.1**). Two-dimensional (2D) materials, such as thin films, have one dimension that is confined to the nanometer scale, whereas two other dimensions can be larger than 100 nm. For one-dimensional (1D) materials, such as nanowires, nanotubes or nanorods, two dimensions should be restricted. Finally, when three dimensions are confined, the materials are referred to as zero-dimensional (0D), in other words, nanoparticles (NPs). Specific examples of different dimensionality include carbon-based nanomaterials as shown in **Figure 1.2**.

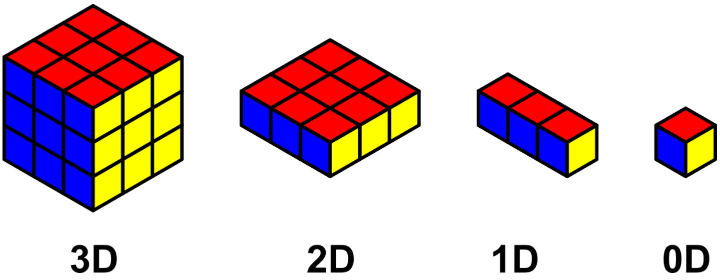

Figure 1.1: Schematic representation of the different classes of nanomaterials. Depending on the number of dimensions restricted to the nanometer scale, they are classified as 2D, 1D and 0D materials. The colours in the figure are used for visibility purposes and have no additional meaning.

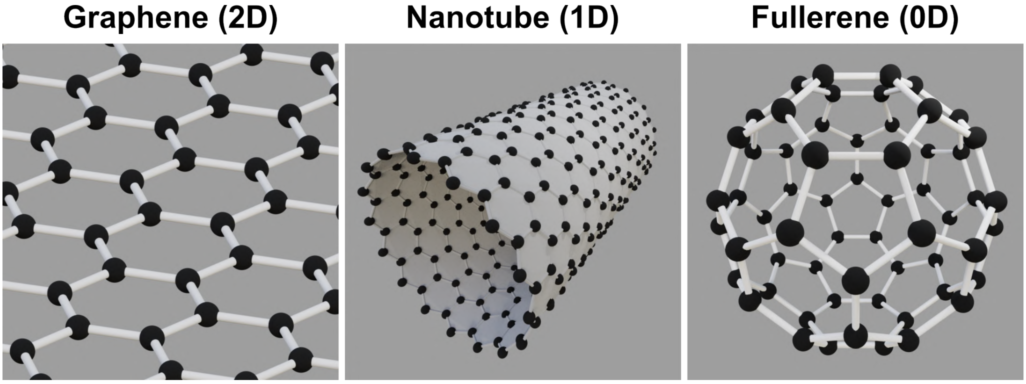

Figure 1.2: Carbon-based nanomaterials of different dimensionalities.

The synthesis and fabrication of nanomaterials can be employed in different manners that can be split into two categories: the top-down and bottom-up approaches (**Figure 1.3**) [2]. The top-down approach involves reducing the size of macroscopic structures to create smaller nanostructures by the removal of the excess material. Techniques such as photo- [3] and electron lithography [4], etching [5], and focused ion beam milling [6] are used to carve or remove material from a larger piece, hereby gradually reducing its size to the nanoscale. These techniques enable precise control over the final structure and are suitable for producing uniform and ordered nanostructures. However, photolithography is hampered by a diffraction limit, and electron beam lithography is extremely time-consuming and expensive. The second approach is based on assembling desired nanostructures step by step from individual atoms or molecules. It is commonly used for the fabrication of NPs. For example, wet chemical synthesis [7] allows precise control of the size, shape, and structure of nanomaterials, thereby tailoring their specific properties for a broad range of applications. Additionally, surface functionalization of nanomaterials with various ligands, polymers, or biomolecules further enhances their functionality and biocompatibility, widening their applications in the fields of drug delivery, biosensing, and tissue engineering [8].

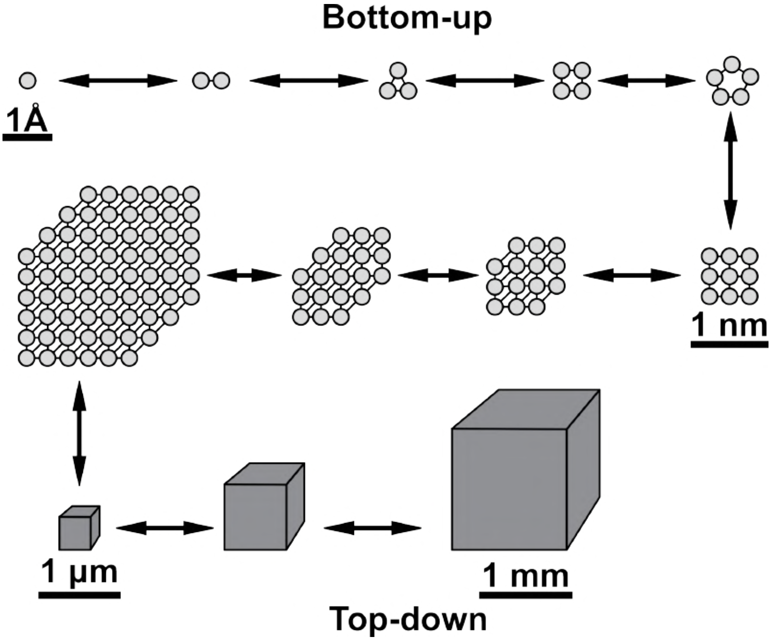

Figure 1.3: The principal protocols for synthesizing nanomaterials: the bottom-up and the top-down approaches. A sphere represents one atom. Scale bars represent the characteristic sizes of the objects. Based on [2].

Among the large variety of nanomaterials, plasmonic NPs deserve a more detailed description in the framework of this chapter due to their remarkable optical properties arising from their interactions with incident light [9]. The applications of plasmonic NPs span a wide range of fields, making them invaluable in various technological and biomedical applications. In photonics, these NPs are employed for enhancing light-matter interactions, leading to improved sensors, imaging devices, and energy harvesting systems [10]. In medicine, plasmonic NPs are utilized for targeted drug delivery, imaging, and photothermal therapy, capitalizing on their ability to absorb and convert light into heat [11, 12]. Furthermore, these nanoparticles find applications in catalysis, where their unique optical properties can be harnessed to drive chemical reactions with enhanced efficiency [13].

The unique properties of plasmonic NPs are caused by localized surface plasmon resonance (LSPR) phenomenon arising from the collective oscillation of electrons at the nanoparticle's surface when excited by incident light [2]. To achieve a tunable and application-oriented LSPR peak, physical features, including size, morphology, and composition of noble metal NPs, play a crucial role and need to be precisely designed (**Figure 1.4**). This can be achieved using dedicated synthesis techniques. Among them, the wet chemical (colloidal) approach, also known as seed-mediated crystal growth, has attracted significant attention and has undergone substantial progress in recent decades. This method allows for the fabrication of nanoparticles with well-defined shapes, such as spheres, rods, and triangles with specific plasmonic properties [14].

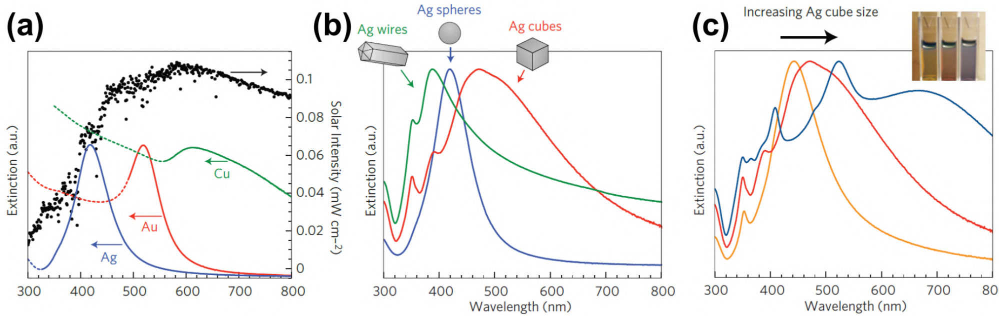

Figure 1.4: Normalized extinction spectra (absorption + scattering) displaying composition, (b) shape, and (c) size-dependent LSPR shifts. The scatter plot in panel (a) shows the intensity of solar radiation (solar spectrum). It can be seen, that the position, shape, and number of LSPR peaks can be routinely adjusted by modifying the composition, shape and size of metallic nanoparticles. Reproduced with permission from [15]. Copyright 2011 Springer Nature.

Another class of plasmonic nanomaterials that is rapidly emerging nowadays is chiral NPs [16]. Chirality is a fundamental property of asymmetry characterized by the absence of improper rotations, making the chiral objects not superimposable to their mirror images. Chirality plays a central role in nature and arises universally across many different fields. The majority of biomolecules and their assemblies exhibit chirality, which is essential for the interactions and reactions that occur within living organisms. Many biomolecules, such as amino acids, sugars (like glucose), and nucleic acids (DNA and RNA), are chiral. The chirality of these molecules has a profound impact on their biological functions. It should be noted that chirality can strongly affect molecular properties. Two molecules that are non-superimposable onto their own mirror image are called enantiomers. Two enantiomeric forms exhibit distinct properties. For example, the right-handed molecule of carvone is responsible for the scent of spearmint, whereas the left-handed enantiomer is responsible for the scent of caraway, even though these molecules are mirror images of each other (**Figure 1.5**).

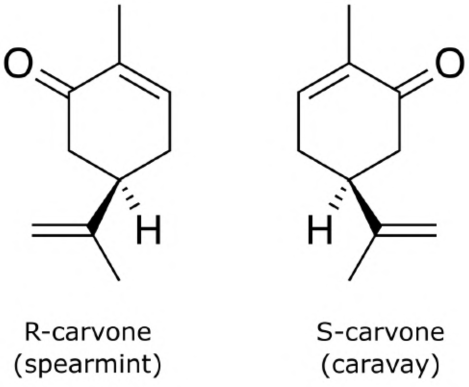

Figure 1.5: Enantiomers of carvone: R-carvone and S-carvone.

Incorporating chiral features into plasmonic nanoparticles provides them with extraordinary optical characteristics. These NPs are capable of interacting distinctively with left- and right-handed circularly polarized light. This unique interaction is a base for employing spectroscopic techniques that rely on the differential absorption known as circular dichroism (CD). CD spectroscopy is extensively used for the identification and study of a wide range of chemical compounds. The pronounced chiroptical effects of asymmetric plasmonic NPs prove to be especially advantageous. They not only enhance CD signal from small concentrations of chiral molecules but also shift it to the visible range, thereby enabling the detection and examination of chiral materials. More detailed information on the properties and synthesis of chiral NPs can be found in **Chapter 6**.

As can be seen from plasmonic NPs, the properties of nanomaterials, such as their reactivity, stability, and ability to interact with the environment, are strongly connected to their size, shape, composition, and crystal structure. These are key parameters for modulating and optimizing the properties of metal/oxide NPs in various applications. Therefore, investigation of the local structure and composition of nanomaterials is of crucial importance to enable the optimization of a controlled synthesis as well as to tune the structure-property connection, leading to materials with specific, pre-defined properties. However, nanomaterials cannot be observed with the naked eye or optical microscopes due to their lack of spatial resolution that is governed by a diffraction limit (Rayleigh criterion). Precisely speaking, two features cannot be resolved as individual objects in the image if they are separated by a distance lower than

$$R = \frac{\lambda}{2n\sin\alpha} \approx 0.61\frac{\lambda}{NA}, \tag{1.1}$$

where λ is the wavelength of light, n is the index of refraction of the medium in which the lens is working and α is the maximum half-angle of the cone of light that can enter the lens, and NA is the numerical aperture, which cannot exceed 1.45. Due to these limitations, the resolution limit of an optical microscope ($\lambda \approx 400nm$) is about 200 nm, which corresponds to the length scale of thousands of atoms and is clearly not sufficient for studying the local structure of nanomaterials. Therefore, more accurate methods to measure the structure and composition of nanomaterials are peremptory.

1.2 Electron Microscopy

Electron microscopy (EM) overcomes the resolution limit of the optical microscope due to the wave-particle duality of electrons established by Louis de Broglie in 1924. The wavelength of electrons is dependent on their momentum, which can be changed by accelerating them through a range of voltages as shown (ignoring relativistic effects) in **Equation 1.2**.

$$\lambda = \frac{h}{mv} = \frac{h}{\sqrt{2meE}} \tag{1.2}$$

where h is Plank's constant, m is the mass of a particle, v is its velocity, e is elementary charge and E is accelerating voltage. Higher accelerating voltage produces high-energy electrons with smaller wavelengths. Therefore, using accelerating voltages of 1–300 kV, electrons with wavelengths of 40 pm down to 2 pm can be produced [17].

The first transmission EM (TEM) was built in 1932 by Max Knoll and Ernst Ruska [18] and later, in 1938, became commercially available. Ruska's TEM had only three lenses and a resolution of about 50 nm, which is significantly better than the best possible optical microscope. Although the basic principles of TEM have not changed since its invention, modern TEM instruments have significantly changed due to rapid improvements in electronics, leading to more stable lens currents and high voltage supplies, which, in turn, have made possible the practical implementation of theoretical electron optics ideas, such as energy filters and aberration correctors.

EM has been a useful tool to perform a detailed characterization of structure and composition at the nanoscale. Although a plethora of electron microscopy imaging modes are available, a rough distinction can be made between TEM and scanning EM (SEM). There are many similarities between TEM and SEM. For example, the components of both are very similar. Each has an electron source/gun that emits an electron beam toward a sample, lenses and electron apertures to focus, shape and control the electron beam to form images and various detectors (**Figure 1.6**). However, it should be noted that the difference between TEM and SEM is significant. The techniques have different working principles, require different sample preparation, and yield different spatial resolutions, as will be discussed in the next sections.

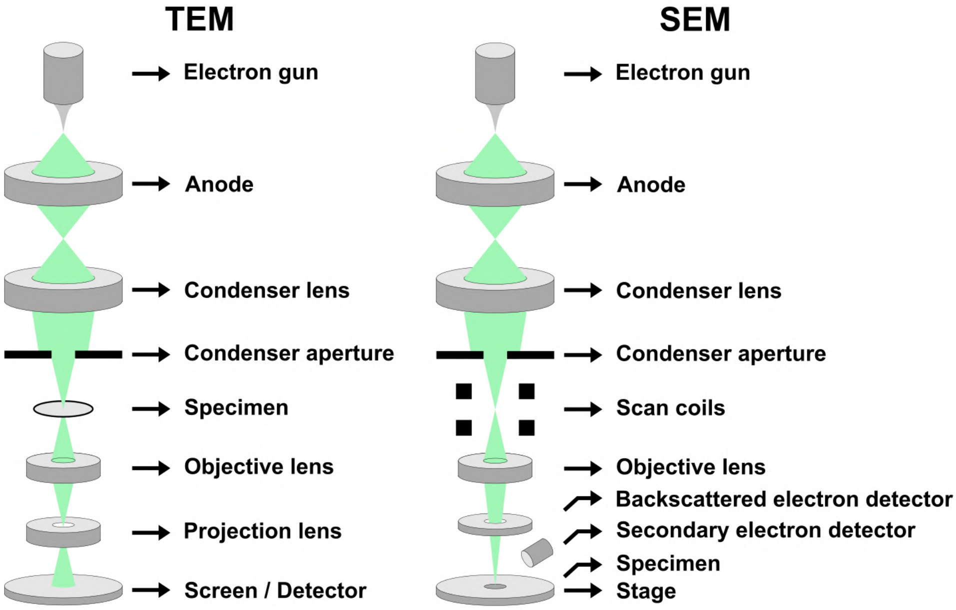

Figure 1.6: Simplified schematic representation of conventional TEM and SEM.

1.2.1 Transmission Electron Microscopy

EM heavily relies on signals generated during the electron-matter interaction, therefore, electron scattering plays a fundamental role in EM (**Figure 1.7**). Scattered electrons can be divided into elastic and inelastic, where elastic scattering results in no electron energy loss and inelastic scattering in some measurable loss of energy.

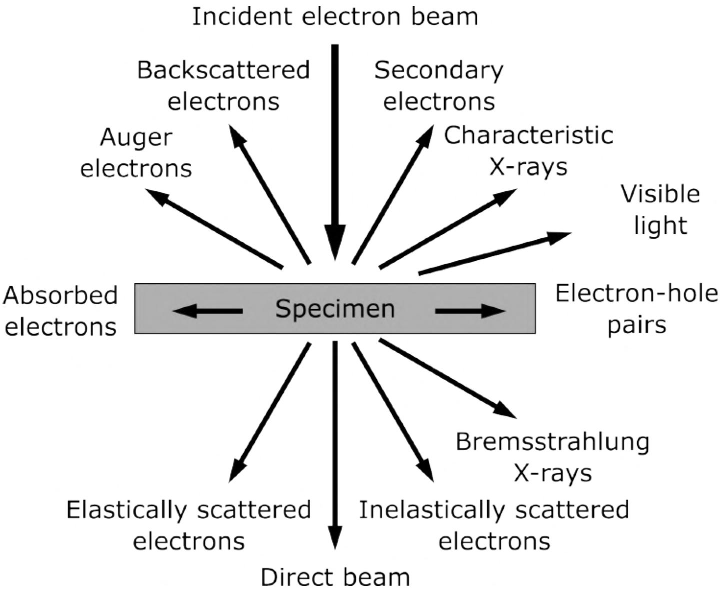

Figure 1.7: Signals generated during the interaction of the electron beam with the specimen.

In conventional TEM, an ultra-thin electron-transparent sample is illuminated by a high-energetic (60-300 keV) broad electron beam (plane electron wave). Electrons that undergo elastic scattering during interaction with matter change their direction upon the Coulomb potential of the atomic nuclei (high-angle scattering) and electron clouds (low-angle scattering). These electrons are the major source of contrast in conventional TEM: amplitude and phase contrast.

Variations in the sample's mass or thickness (or both) alter the amplitude of electrons transmitting the sample through Rutherford scattering. This type of scattering occurs to high angles. By positioning the objective aperture around the direct beam (central optical path), electrons scattered to these high angles are blocked from reaching the image plane. As a result, a bright field (BF) image is created. In a BF image, areas with greater mass or thickness appear darker, demonstrating what is known as mass-thickness contrast. However, TEM samples are often crystalline materials, and atoms are arranged in a repeatable 3D arrangement. When electrons enter these crystals, they scatter elastically to specific angles (Bragg angles), reflecting the material's unique lattice spacings (denoted as d spacings). In BF imaging Bragg scattering is responsible for diffraction contrast: the area where diffraction takes place appears darker on the image.

Bragg scattering results in diffraction patterns that provide an image of Bragg angles, revealing details about the crystalline structure, including its symmetry, lattice spacings, strain, and defects. In materials that are polycrystalline or amorphous, the diffraction pattern appears as diffuse rings, with the ring radius corresponding to lattice spacings and the diffuseness indicating the size of the crystallites. By positioning the objective aperture around a selected Bragg beam, corresponding to a specific lattice spacing, a dark field (DF) image can be formed. Amplitude contrast in these images arises from variations in diffracting conditions for a certain Bragg angle within the field of view, allowing the detection of subtle changes in crystalline orientation.

Phase contrast arises when multiple beams, such as the direct and Bragg beams, constructively and destructively interfere because of relative phase shifts. This interference leads to the formation of lattice fringes in high-resolution TEM (HR-TEM) images, Fresnel fringes around the edges of the specimen, or Moiré patterns. These images yield the highest spatial resolution because they incorporate multiple beams, including those scattered at higher angles, which correspond to smaller lattice spacings (denoted as smaller d-spacings). This inclusion of a broader range of scattering angles allows for a more detailed and precise visualization of the specimen's structure at the atomic level.

A conventional TEM can be modified into a scanning transmission electron microscope (STEM) by the addition of a system that rasters a convergent beam across the sample to form the image when combined with dedicated detectors. The image is produced by correlating the electron count to the position of the scanning beam (known as the "probe"). Different imaging modes are possible depending on the scattering angle. Electrons scattered to low angles (< 10 mrad) are used for BF-STEM and electron diffraction, providing information about the specimen crystalline structure, whereas electrons scattered to higher angles (> 50 mrad) are used in high-angle annular dark field scanning TEM (HAADF-STEM) providing the mass-thickness contrast. Annular dark field (ADF) detector can be set to be sensitive to both diffraction and mass-thickness contrast (**Figure 1.8**).

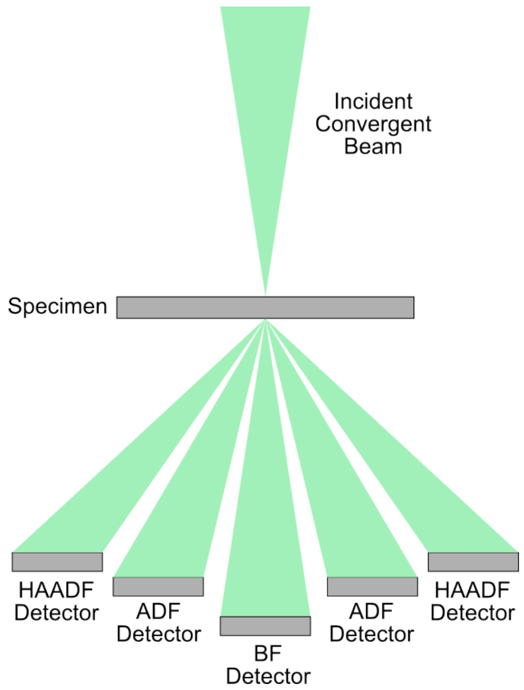

Figure 1.8: Various types of electron detectors used in STEM.

During inelastic scattering, energy is transferred from the electron beam to the atoms of the specimen, causing the ionization of atoms and transitions of electrons from one energy level to another within the atom. This results in different types of signals, such as secondary electrons (SEs), Auger electrons and photons, as shown in **Figure 1.7**. Energy-loss electrons themselves, characteristic X-rays and visible light are used in analytical electron microscopy (AEM), providing information about the chemical identity of the specimens. The most used AEM modes are energy-dispersive X-ray spectroscopy (EDXS) and electron energy loss spectroscopy (EELS) (**Figure 1.9**).

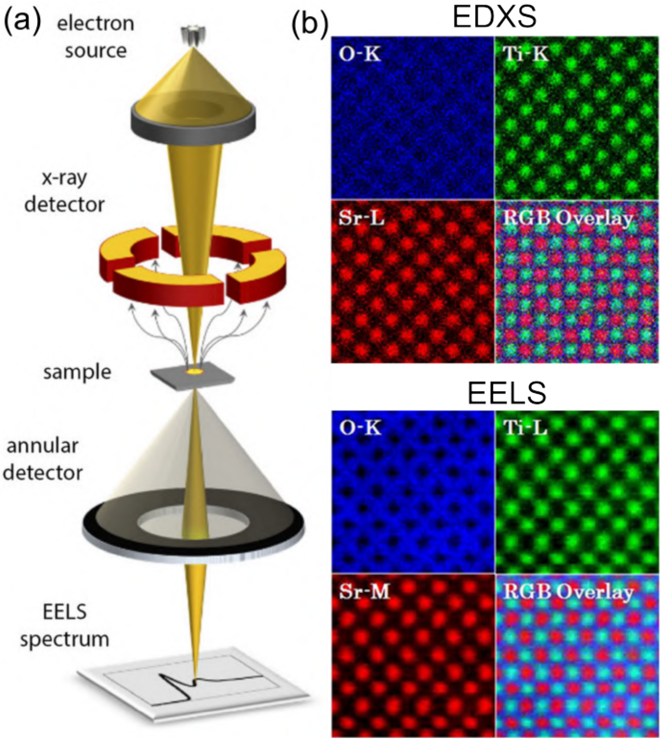

Figure 1.9: (a) Schematic ray diagram describing the geometry of EDXS and EELS systems in STEM. Reprinted from [19] (b) EDXS and EELS spectrum images (maps) of $SrTiO_3$. Image adapted from Glossary of TEM Terms, JEOL Ltd.

In EDXS, when the electron beam interacts with the specimen, electrons from the inner shells of the atom can be excited and ejected from these shells. This causes a transition of an electron from a higher energy shell to fill a formed vacancy, with an X-ray photon emitted with energy equal to the difference between these two energy levels. This energy is characteristic for each element. Using an energy dispersive spectrometer, the number of emitted X-rays and their energy can be measured [20]. On the other hand, EELS detects electrons after the interaction with the specimen. Energy loss electrons pass through a magnetic prism where they are dispersed according to their kinetic energies. This energy distribution provides information about the local elemental composition, chemical bonds, optical properties, and vibrational modes [21]. The recorded EEL spectrum can be split into three energy regions: the zero-loss (elastically scattered electrons), low-loss (2-50 eV), and core-loss region (> 50 eV). The low-loss region yields information on the plasmon oscillation of the valence electrons in the sample whereas the core-loss region of the spectrum contains information on the electron-electron interaction from the inner shells (**Figure 1.10**). Both EDX and EEL spectra can be transformed into quantitative images of the distributions of all the elements present in the specimen (**Figure 1.9 b**).

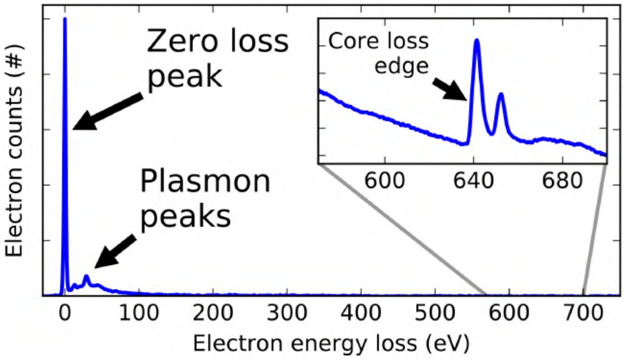

Figure 1.10: Energy loss spectrum showing typical features such as the zero-loss peak corresponding to transmitted electrons through the specimen, the plasmon frequency, and the chemical fingerprint of the material in the core loss edge. Reproduced from [22] under the term of CC BY-SA 4.0 license.

1.2.2 Scanning Electron Microscopy

SEM uses a focused beam of electrons with energies below 30 keV. The beam is scanned across the surface of the nanomaterial. Usually, samples studied in SEM are sufficiently thick to absorb incoming electrons meaning that they are not electron transparent. Primary electrons absorbed by a sample encounter multiple electron scattering events within a material, causing the formation of signal generation volume (**Figure 1.11**). Because of the strong interaction between the electrons and the material, various signals, illustrated in **Figure 1.11**, are generated that contain local information about the surface topography (secondary and backscattered electrons) and chemical composition (backscattered electrons, X-rays and cathodoluminescence). However, this information only relates to the near-surface region of the material (ranging from a few nm to a few μm depending on the type of signal) and, therefore, does not provide any insight into its internal structure. It should be noted that, due to strong electron scattering, leading to delocalization of the signal [23] determined by a generation volume (**Figure 1.11**), the resolution of SEM is limited to about 1 nm. In other words, SEM is probing the near-surface structure of a sample under investigation, whereas in TEM a projection of the entire sample is measured. Due to finite generation volume and interaction of generated signals (primarily secondary and backscattered electrons) with structural features of the surface, SEM images provide pseudo-3D perception and resemble reflected-light images. SEM is quite user-friendly and often accessible in a scientific environment, but the resolution of a typical SEM instrument is of the order of 1-20 nm. On the other hand, (S)TEM can yield atomic resolution information on both the structure and composition of a broad variety of nanomaterials, eventually along with signatures of their electronic and optical properties.

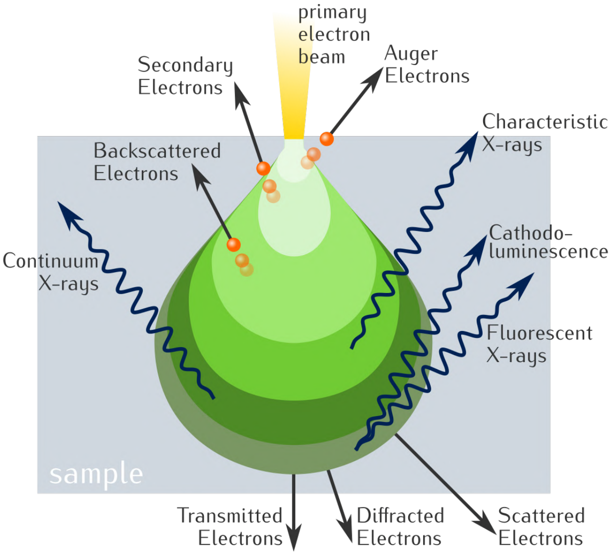

Figure 1.11: Signal generation volume formed as a result of multiple electron scattering within the sample during electron-matter interaction in SEM. Reproduced from [24] under the term of CC BY-SA 4.0 license.

Because of its superior resolution and advanced capabilities for chemical and structural analysis over SEM, (S)TEM is a preferable tool in nanoscience nowadays. However, as already mentioned, (S)TEM images conventionally only correspond to a 2D projection of a three-dimensional (3D) object, which often can be misleading as illustrated in **Figure 1.12**. Therefore, in order to reliably understand the structure-properties relationship of nanomaterials in (S)TEM, it is necessary to retrieve the hidden 3D information from a series of 2D micrographs using electron tomography (ET).

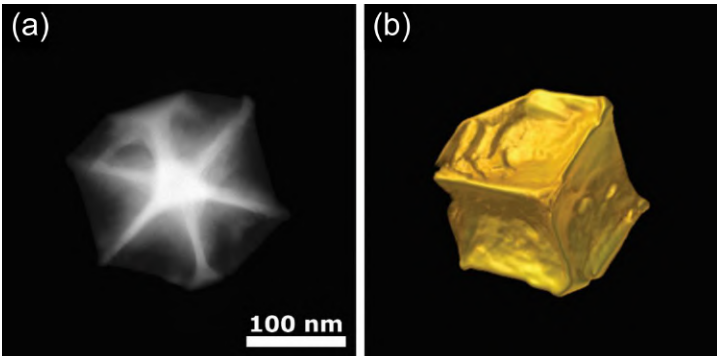

Figure 1.12: (a) HAADF-STEM image of a gold nanoparticle. This 2D projection image suggests that the morphology corresponds to a nanostar. (b) Real morphology of the same nanoparticle shown in (a), obtained by electron tomography. It is clear that the morphology corresponds to a truncated nanocube. Image courtesy Dr. Thomas Altantzis.

1.3 Electron Tomography

ET has been developed as a technique to determine the 3D structure of nanomaterials from 2D images. Similarly to X-ray computed tomography (CT), which finds extensive application in healthcare, ET enables an understanding of the geometry of complex NPs and their internal structure. Therefore, ET emerges as a key approach to investigate NPs, their assemblies, and devices characterized by complex 3D shapes. In the ET experiment, a tilt series of 2D projection images is acquired over a wide angular range with tilt increments of typically 1-3° by tilting the sample holder at controlled angles using a calibrated microscope stage. Next, these projection images are aligned to a common tilt axis to eliminate relative shifts between them. Based on this aligned series, a 3D reconstruction is performed using a dedicated mathematical algorithm [25] (**Figure 1.13**).

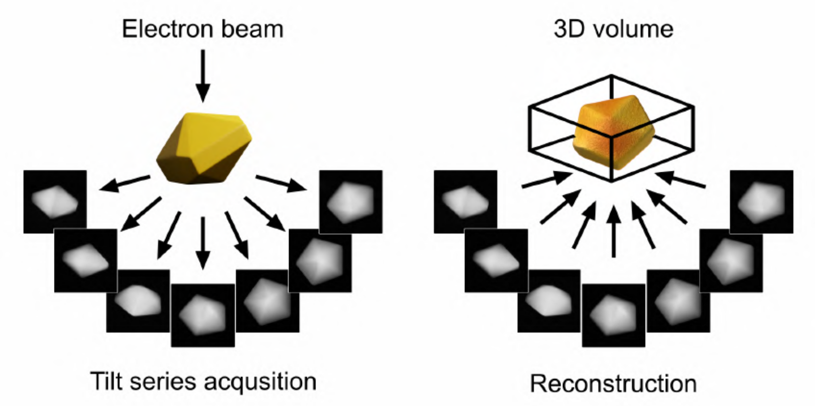

Figure 1.13: Acquisition of the tilt series in (S)TEM and visualization of the 3D reconstruction from an object, the reconstruction is obtained by re-projecting the tilt series using a mathematical algorithm.

The acquisition of a tilt series is the first step of any tomography experiment. The imaging mode producing input data for ET should obey the projection requirement, meaning that the intensity in the projected images should be a monotonic function of a certain property of the sample under investigation [26]. It should be noted that effects such as electron diffraction and electron channelling can violate this requirement and lead to artifacts in ET reconstructions and need to be minimized during the data acquisition step. For biological materials and non-crystalline inorganic systems, the use of BF-TEM is appropriate because mass-thickness contrast is dominant and satisfies the projection requirement. However, materials in physical science are often crystalline and consequently produce diffraction contrast. Therefore, there is no longer a monotonic relation between the intensity in the projected images and the thickness of the sample, which implies that the projection requirement is no longer fulfilled when using BF-TEM. Therefore, 3D studies of crystalline samples are often performed using HAADF-STEM images to overcome this problem.

In ET, the specimen ideally would be tilted over a full tilt range of ±90°, however, since the specimen holder is located inside a pole-piece gap of the objective lens that is limited in space by approximately 5 mm (see **Figure 1.14 a**, g-dimension), full tilt series cannot be acquired to avoid a collision with the polepieces of the objective lens. Additionally, the TEM holder, on which the grid containing the specimen is mounted, can also induce a shadowing effect as illustrated in **Figure 1.14 b**, reducing the number of projections that can be recorded even further. The tilt range is restricted to approximately ±40° for a regular sample holder, leading to a "missing wedge" of information (**Figure 1.15**) that results in artifacts in the final reconstruction (**Figure 1.16**). For example, blurring and elongation along the direction of the optical axis can be observed. A dedicated tomography holder with reduced dimensions (**Figure 1.17**) enables to improve a tilt range to ±80° significantly reducing the "missing wedge" effect.

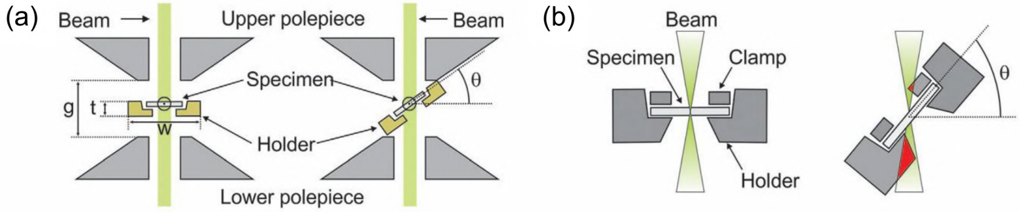

Figure 1.14: (a) Geometry of the polepiece gap and specimen holder at zero tilt and at the maximum tilt angle θ. θ is defined by the dimensions of the specimen holder tip (t, w) and the polepiece gap (g). (b) Geometry of the shadowing effect of the electron beam by the holder. Adapted from [26].

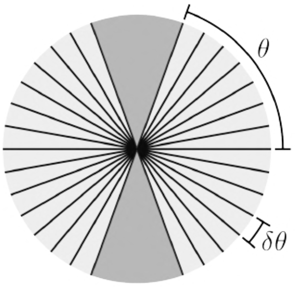

Figure 1.15: Representation of sampled frequencies in Fourier space for a linear single-axis tilt scheme. Projections are acquired over a range θ with increment $\delta\theta$. The gap of missing information indicated in dark grey is called the “missing wedge”.

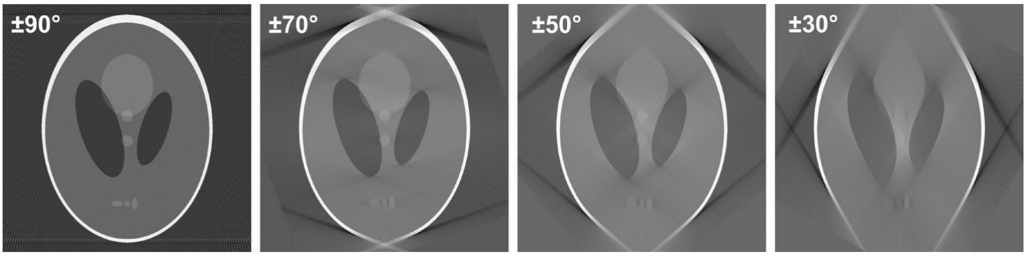

Figure 1.16: Effect of the missing wedge for the Shepp-Logan phantom. The tilt range is indicated in the figures. The final reconstruction is blurred and elongated.

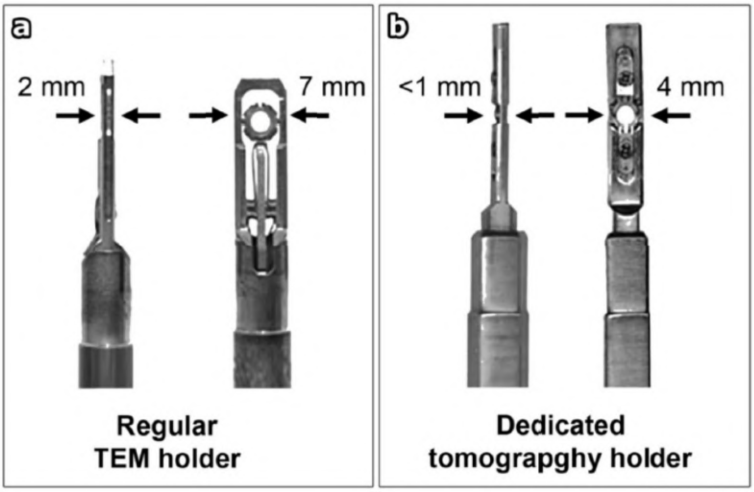

Figure 1.17: (a) Regular double tilt TEM holder and (b) dedicated electron tomography holder with indicated dimensions. Adapted from [26].

The next step is the alignment of the acquired tilt series. The particle is assumed to not shift throughout the tilt series acquisition in ET reconstructions. Therefore, all the image shifts that occurred during the acquisition step when tilting the sample from one angle to another must be compensated prior to the reconstruction. This can be done by image registration using correlation techniques [27]. The cross-correlation between two images is computed as the normalized product between the Fourier transform of one image and the complex conjugate of the Fourier transform of the second image. By locating the maximum in the cross-correlation, the relative shift between the images can be found and compensated (**Figure 1.18**). Another important step is the alignment of the computational tilt axis to the experimental one by iterative rotation and translation to minimize the arc-shaped artifacts in the reconstruction.

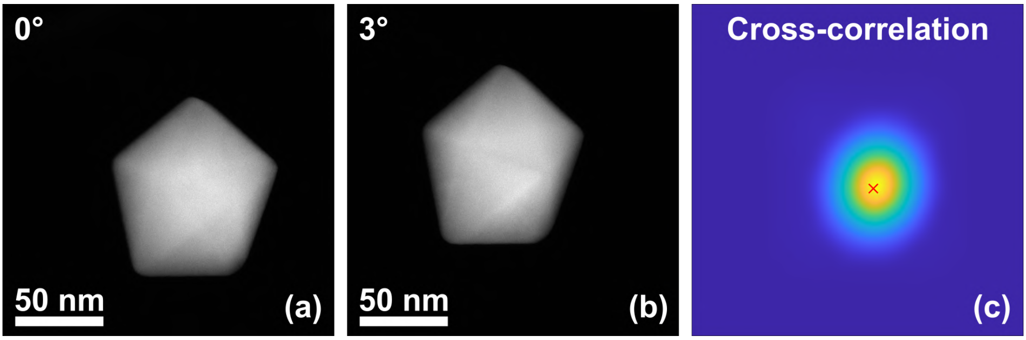

Figure 1.18: (a)-(b) Two consecutive projections acquired during the ET experiment and (c) cross-correlation image of them. The position of the maximum in the cross-correlation with respect to the middle reveals the relative shift between both images. When two projections are optimally aligned, the position of maximum intensity (depicted with a red cross) will coincide with the centre of the image.

Once the tilt series is aligned, it can be used as an input for a mathematical algorithm to obtain a 3D reconstruction. The mathematical basis of tomography relies on the Radon transform that was introduced in 1917. In a simple case, the Radon transform (**Figure 1.19**) is an integral transformation that describes the projection of an object $f(x, y)$ defined on the plane as a function Rf defined on the 2D space of lines in the plane, whose value at a particular line is equal to the line integral of the function over that line (**Equation 1.3**).

$$Rf = F(t, \theta) = \int_L f(x, y)\, dS, \tag{1.3}$$

where dS is the unit vector along the projection direction L. In other words, the Radon transform converts an object in Cartesian coordinates (x, y) into an object in Radon coordinates (t, θ). The (t, θ) coordinates represent the projection angle θ and the distance t of the projection line from the origin, as shown in **Figure 1.19**. The Radon transform converts a point into a sine curve. Therefore, the image in Radon space (set of projections) is typically called a sinogram.

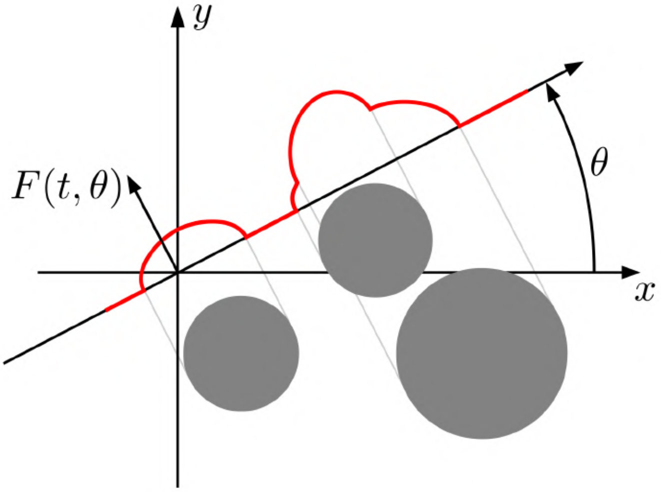

Figure 1.19: Illustration of the Radon transform. The object $f(x, y)$ and its projection $F(t, \theta)$ for a given projection angle.

The object $f(x, y)$ can be analytically reconstructed from the projections using the inverse Radon transform known as back projection. However, back projection as an integral transform requires ideally an infinite amount of projections, which is impossible to acquire during real experiments. Therefore, back projection only provides an approximation of the original object, as can be seen in **Figure 1.20**. The effects of undersampling can also be shown using the projection slice theorem that states that a projection of an object at an angle is mathematically identical to a section through the Fourier transform of that object at the same angle **Figure 1.21**. Each projection provides information about the object in Fourier space in a particular direction. By acquiring projections at many angles, the entire object can be reconstructed in real space by calculating the inverse Fourier transform. Hereby, the Fourier slice theorem suggests a potential method for tomographic reconstruction: by simply summing the projections in Fourier space at the corresponding angles and applying an inverse Fourier transform, the object can be retrieved. It should be noted that the mathematical principles are explained here by considering a 2D object and its 1D projection. The extension towards a 3D object and its 2D projections can be done without any loss of generality.

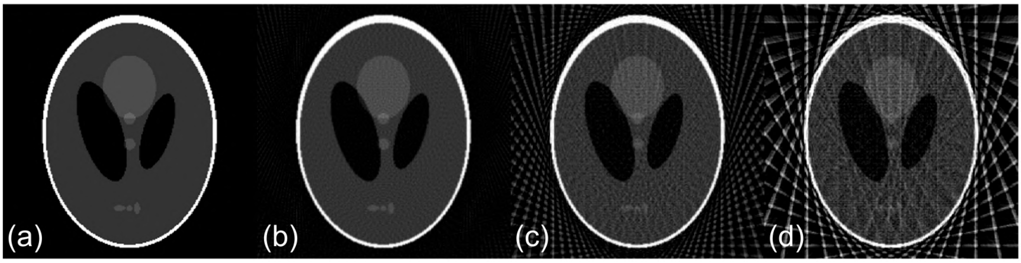

Figure 1.20: Effect of the angular sampling on the reconstructions. (a) Shepp-Logan phantom, (b)-(d): reconstructions based on (b) 90, (c) 24, (d) 18 projection angles.

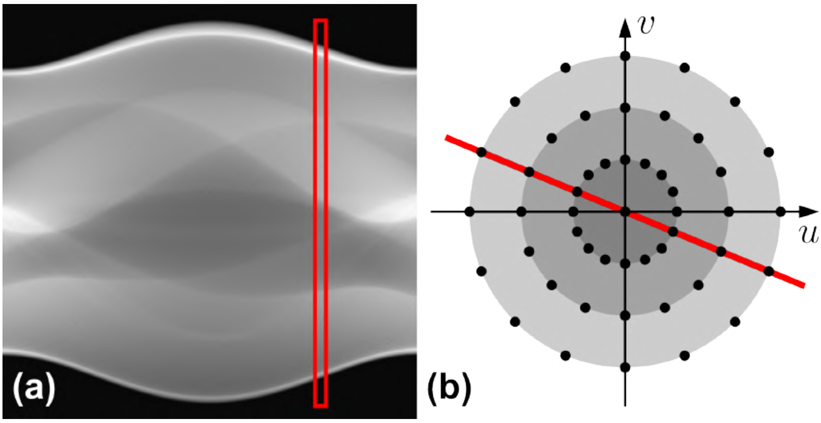

Figure 1.21: Illustration of the Fourier slice theorem. The polar sampling causes highly inhomogeneous sampling, which is evident from the more closely packed dots near the centre of the Fourier domain.

Uneven sampling results in a blurring of the final reconstruction. This restriction can be eliminated by applying a filter suppressing low frequencies (filtered backprojection, FBP). However, the main limitation of FBP is its high sensitivity to the amount of input data, therefore, the FBP algorithm is not commonly used in ET. This reconstruction technique is mostly employed for medical computed axial tomography reconstructions, where a set of projection images over all projection angles is available. Therefore, ET requires advanced reconstruction algorithms. The Simultaneous Iterative Reconstruction Technique (SIRT) involves refining the reconstruction at each iteration by solving the minimization problem

$$\hat{x} = argmax_x \|Ax - b\|_2^2, \tag{1.4}$$

where x is the vector that represents the reconstructed object, A is the projector operator, and b is the vector that represents the projection images. The initial iteration is obtained by applying the back projection method. Subsequently, images based on the first reconstructed volume are generated at the same projection angles and compared with the input images for reconstruction. The relative error between the input and the generated projection is computed simultaneously for each tilt angle and used to generate a new reconstructed volume. The procedure is repeated until convergence for the minimization of the relative error between input data and generated data is reached [28]. This is the most commonly used reconstruction method, although more advanced algorithms exist. For example, the Expectation Maximization (EM) iterative algorithm alternates between performing an expectation and maximization steps in order to maximize the probability of explaining the input data known as a "likelihood" [29]. It should be noted that the SIRT algorithm can also be demonstrated to converge towards a maximum likelihood solution, but it is only suitable when the noise in the input data is Gaussian distributed. An advantage of EM is the adaptability to handle input data characterized by a Poisson distribution, experimentally arising from the discrete number of events at each measured point – such as the number of scattered electrons in HAADF-STEM, that makes EM algorithm a very popular practical method for obtaining electron tomography reconstructions.

Advanced algorithms for ET reconstruction also include methods that employ the use of prior knowledge such as Discrete Algebraic Reconstruction Technique (DART) [30] and Total Variation Minimization (TVM) [31]. The DART algorithm can be used when the sample consists of only a few different compositions, each corresponding to a constant grey level in the reconstruction. It uses an iterative algorithm that combines a continuous iterative reconstruction combined with segmentation. The TVM reconstruction algorithm is based on the principles of compressed sensing. In this method, the prior knowledge that the boundary of the specimen is sparse is used. By incorporating such prior knowledge, these advanced algorithms contribute to the improvement of tomographic reconstruction, but they are highly computationally demanding and require careful choice of reconstruction parameters, e.g., threshold intensity values for DART reconstruction.

The final step of any tomography experiment is the visualization and interpretation of the obtained 3D reconstruction. This can be done using different techniques such as orthoslices, isosurfaces, and volume rendering using voxels (so-called voltex rendering) (**Figure 1.22**). Orthoslices are cross-sectional slices through the reconstruction that allows examination of the internal structure of the object in three perpendicular directions (if the slice is taken in an arbitrary direction, it is usually called an oblique slice). This visualization protocol does not require thresholding of the data and, thus, is considered the most reliable visualization technique among others. On the contrary, both isosurfaces and voltex rendering employ thresholding of the data. For isosurfaces, voxels with identical intensities are connected to form a connected surface, effectively reducing the 3D volume to a 2D surface, whereas voltex rendering traces the entire 3D volume based on the emission and absorption of light that pertains to every voxel of the volume. The algorithm simulates the light rays through the volume from a given intensity, colour, and transparency.

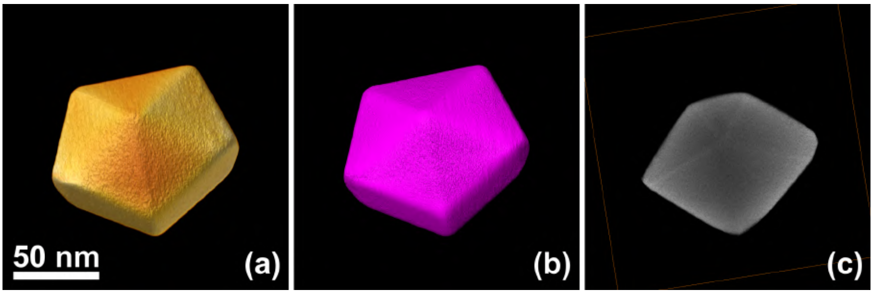

Figure 1.22: (a) Voltex and (b) isosurface rendering of Au Ino decahedron. (c) XY-orthoslice through the centre of the reconstruction that enables the investigation of the interior of the NP.

1.4 State-of-the-art of Electron Tomography

During the past decades, ET in HAADF-STEM mode has become a popular technique to investigate the overall morphology of nanomaterials, to determine the nature of surface facets, and even to characterize the atomic structure in 3D. Contributions to the state-of-the-art in the field were done by the EMAT group, where the PhD research described in this thesis was done, and the other groups [32–39]. In the following section the progress in atomic resolution tomography, fast acquisition approaches and *in situ* tomography will be reviewed.

1.4.1 Atomic-resolution Electron Tomography

In [37], a methodology to measure the 3D atomic structure of free-standing nanoparticles was proposed based on a limited number of high-resolution HAADF-STEM images along the main crystallographic zone axes. The in-zone axis projections of a NP were used as an input for compressed sensing reconstruction. This approach allowed to obtain more reliable atomic-scale reconstruction by exploiting the sparsity of the object (and its 3D reconstruction) as prior knowledge, assuming that only a limited number of voxels contain an atom and most voxels correspond to a vacuum (**Figure 1.23 a**). Furthermore, without assuming the positions of the atoms during tomographic reconstruction, this technique enabled the investigation of strain in the atomic lattice in Au nanorod through the extension of Geometrical Phase Analysis (GPA) to 3D (**Figure 1.23 b**). Another methodology based on a continuous tilt series of high-resolution images uses an assumption that the atomic potentials can be modelled with 3D Gaussian spheres. It was used to retrieve the 3D atomic structure of Au nanodecahedron [40]. The coordinates of each atom in the NP were directly retrieved, enabling the determination of 3D displacement maps for strain analysis.

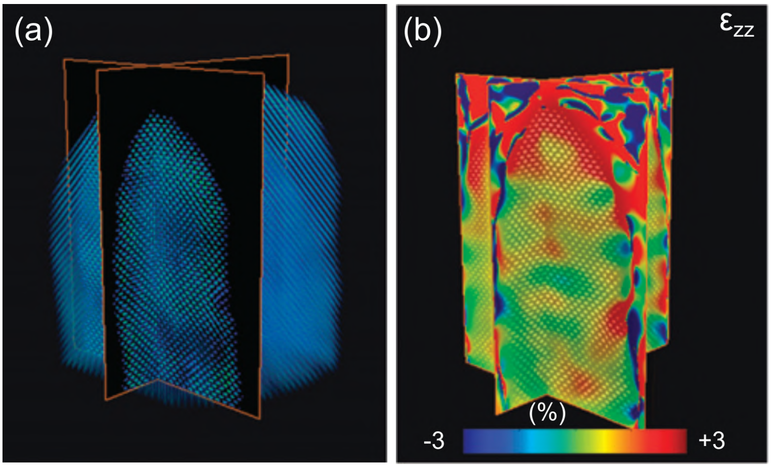

Figure 1.23: (a) Volume rendering of the reconstructed Au nanorod with two selected slices through the reconstruction. (b) Slices through the 3D ε_{zz} strain measurement. Reproduced with permission from [37]. Copyright 2012 Springer Nature.

1.4.2 Fast Electron Tomography

Unfortunately, the acquisition of a conventional tilt series for ET is a time-consuming process that requires at least 1 hour for a standard experiment. In addition, after the acquisition, a post-process reconstruction step is required to evaluate the final 3D shape of the nanomaterial. Consequently, only a limited number of NPs can be investigated, hampering a general understanding of the average structure of a given sample. This restriction further limits a thorough understanding of the structure-property relations, especially because the properties of nanomaterials are mostly measured by ensemble techniques. It is, therefore, clear that ET is a very valuable technique but still limited in providing 3D structural information in a time-efficient manner. Furthermore, the long acquisition times lead to the accumulation of high electron doses ($> 10^4\ e/\AA^2$), which hampers the application of ET to dose-sensitive specimens, among which are highly promising classes of materials, such as lead halide perovskites, metal-organic frameworks, and many types of zeolites. Another limitation arises from ET combined with *in situ* stimuli that allows to perform a dynamic characterization of changes in the 3D structure of nanoparticles under realistic conditions and predict the evolution of their properties. Such an experiment is challenging due to the narrow tilt range of dedicated *in situ* specimen holders. Moreover, the lengthy acquisition of a tilt series can be too slow to capture the fast changes of the materials when exposed to relevant conditions. Overcoming all of these mentioned aspects is the aim of the REALNANO project, funded by the European Research Council Consolidator grant [41].

The problems described above can be partially solved by recently developed methods that significantly accelerate the acquisition and reconstruction process for ET [42–44]. Unlike conventional ET acquisitions where the stage is manually tilted and re-centred before capturing a new projection image, fast tomography involves simultaneous image acquisition and stage tilting, enabling the acquisition of hundreds of frames during the tilting process. The tilt speed is carefully adjusted to find an optimal balance between speed and image quality. The total acquisition time for ET series, then, can be significantly reduced from around 1 hour (for conventional ET) to just 6 minutes when employing fast acquisition schemes. The decreased acquisition time enables the recording of more tomographic series within a one-hour timeframe, resulting in higher throughput for nanomaterial characterization.

However, fast ET faces challenges related to tracking and refocusing the nanoparticle during the acquisition process. During the sample tilt, the particle experiences displacements. Consequently, motion-blurring artifacts may be present in some projection images. These artifacts can be corrected for by applying a low-pass filter within Fourier space, resulting in improved image quality (**Figure 1.24**) [42]. Projection images that were heavily affected by blurring need to be excluded before the reconstruction. However, the number of such projections is a fraction of the total number of projection images and their removal does not compromise the quality of the final result. Further improvement of the approach, is incremental tomography that continuously captures projection images, while the sample tilt is incrementally tilted (with 2-3° step and 5-10s pause after each tilting step) across the entire range of tilt angles. The incremental approach requires slightly longer acquisition times (around 6-8 minutes), but the pause between tilting steps allows the stage to stabilize and the microscopist can track the particle and adjust its position and focus to the optimal settings. This results in higher-quality data and reconstructions compared to the continuous approach.

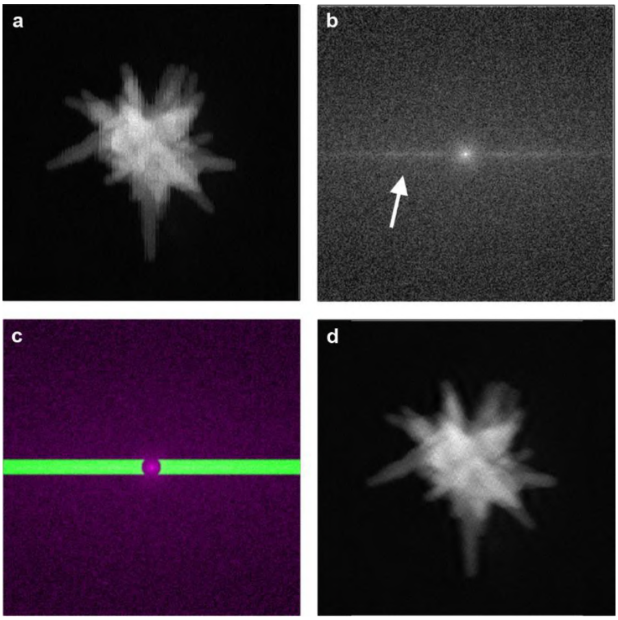

Figure 1.24: (a) HAADF-STEM image obtained during the fast ET acquisition of a single nanostar, revealing noise in the direction of scanning. (b) The amplitude of the Fourier transform of (a). The white arrow indicates the presence of directional noise at higher frequencies. In order to correct the projection images a dedicated low pass filter was used (c) to remove these higher frequencies and restore the projection image (d). Reproduced from [42] under the term of the CC BY 4.0 license.

1.4.3 *In situ* Electron Tomography

The advancements in fast acquisition strategies for ET have enabled a series of *in situ* heating experiments at EMAT. It allowed to perform the 3D characterization of heat-induced morphological changes of highly asymmetric Au nanostars and study the influence of the reshaping on their plasmonic properties (**Figure 1.25**) [42]. Further studies combined *in situ* heating and ET to understand the heat-induced reshaping of AuPd octopods. The enhanced thermal stability of AuPd octopods up to 450°C in a vacuum was shown, whereas pure Au octopods already reshaped at 200°C [45]. Later, alloying in single Au@Ag@SiO_2 NPs of varying shapes was investigated. The composition in the reconstructions was quantified based on the changing voxel intensity histograms in the NPs upon alloying. This quantification allowed to determine the degree of alloying as a function of time for the different NPs. By fitting the experimental results to diffusion simulations, diffusion coefficients could then be extracted [46].

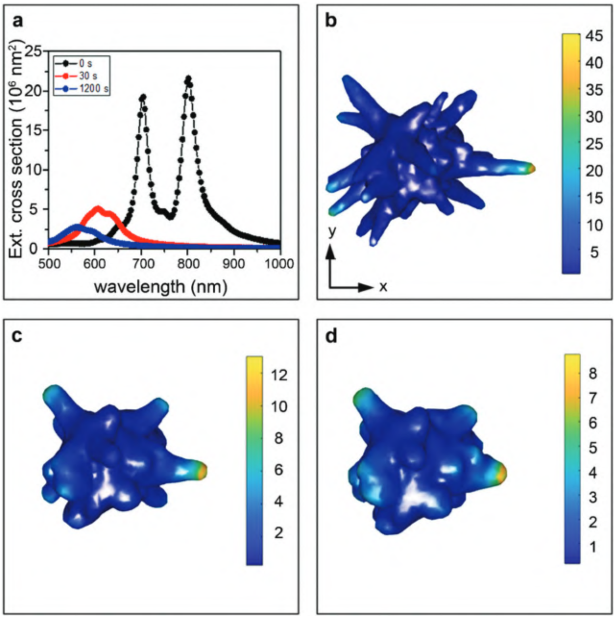

Figure 1.25: (a) Simulated extinction spectra of unheated and heated asymmetric Au nanostars and corresponding 3D ET reconstructions: (b) unheated NP, (c) after 30s of heating at 300°C, (d) after 1200s of heating at 300°C. Reproduced from [42] under the term of the CC BY 4.0 license.

ET *in situ* experiments remain challenging because of several reasons. Firstly, during the acquisition of a fast ET series, the specimen needs to be quenched to room temperature to avoid changes of the NPs during the acquisition leading to a significant increase in the acquisition times. Secondly, the acquisition of a fast tomography series is still a lengthy procedure and a limited number of NPs can be investigated within one experimental day hampering an understanding of the average structure of NP ensemble. Therefore, alternative characterization techniques that allow for high-resolution characterization of the surface structure without the need to acquire a full tilt series in ET are required which would enable a more time-efficient investigation with better statistical value and reliable *in situ* experiments. It is interesting to note that, rather than obtaining a 3D reconstruction of the entire nanoparticle structure, the most important goal of many ET studies is often to only extract the surface morphology of the NPs. Indeed, the surface structure of a NP determines its reactivity, stability, and ability to interact with the environment. Especially the surface faceting of NPs [47] is a key parameter toward modulating and optimizing the properties of metal/oxide NPs in catalytic [48], plasmonic [49, 50], and medical [51] applications.

This PhD work is devoted to finding alternative techniques for the characterization of the morphology of NPs to improve the throughput and temporal resolution of ET. Here, we propose to investigate the surface structure of nanomaterials through the detection of secondary electrons in STEM mode, while using the sample itself as the detector. The results of this work will contribute towards improved throughput of 3D morphological analysis in STEM, enabling new dynamic experiments where the object of interest changes during the investigation.

Chapter 2

Secondary Electron Imaging in Transmission Electron Microscopy

In this chapter, the application of secondary electron imaging in TEM is discussed and proposed as an alternative way of retrieving 3D information in nanomaterials. Secondary electron electron beam induced current is introduced and its practical aspects are discussed.

2.1 Secondary Electron Imaging in STEM

SEs are low-energy electrons (< 50 eV) ejected from the sample by inelastic interactions between the primary electron beam and weakly bonded conduction-band electrons in metals or the valence electrons of insulators and semiconductors. SEs originate from the near-surface region of the sample and, therefore, carry topographical information. The SE signal is, therefore, exploited in SEM as one of the main imaging modes. As mentioned earlier, typical field emission gun SEMs have SE imaging resolutions of just a few nm restricted by the size of the beam, the presence of aberrations, and signal delocalization due to electron-matter interactions. These aspects limit the applicability of SEM for the investigation of NPs with complex or irregular surface structures at the scale from a few nm to sub-nm.

SE imaging has been incorporated into STEM for several decades [52–55]. The higher acceleration voltages, compared to SEM, and the use of ultra-thin samples enabled SE images with resolutions down to the sub-nm regime. High-resolution SE imaging was studied in Cavendish Laboratory at the University of Cambridge and by Liu and Cowley at Arizona State University [56, 57]. In the Cavendish laboratory, off-axis and on-axis methods of SE detection were implemented. On-axis method used an Everhart-Thornley detector (ETD) that comprised of a scintillator and photomultiplier located above the upper objective pole piece. The on-axis detector consisted of an annular channel plate incorporated in a similar way to the HAADF-STEM detector and allowed energy analysis of detected SEs by inserting a copper grid at a negative potential in front of the detector and measuring the current collected after the channel plate as a function of the retarding potential [53]. In Liu and Cowley's works SE detection was combined with Auger spectroscopy. The ETD and Auger spectrometer were placed above the upper pole piece. High-resolution SE images of metal particles supported on various oxides were demonstrated revealing information about the relative locations of nanoparticles with respect to the surface topography of the support (**Figure 2.1**) [57]. It was shown that sub-nanometer surface details can be observed implying that the generation processes of SEs are localized within 1 nm or less. Later, it was shown that the generation of SEs is directly related to large-angle inelastic scattering of the high-energy incident electrons. These localized inelastic scattering events involve large momentum transfer mechanisms such as Umklapp (high-momentum, low-energy transfer processes) or phonon-assisted electron excitation processes [57].

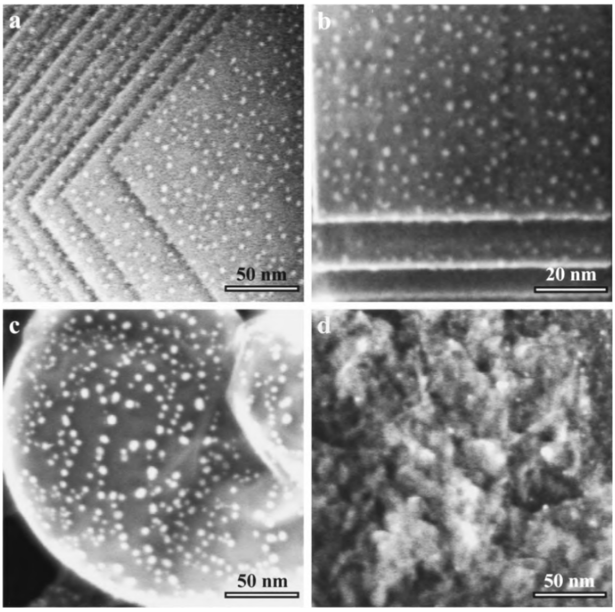

Figure 2.1: High-resolution SE images of (a) Ag and (b) Fe nanoparticles on MgO crystals, (c) Ag nanoparticles on α-alumina powder and (d) Pd nanoparticles on γ-alumina crystals. Reproduced with permission from [57]. Copyright 2005 Oxford University Press.

Later, it was demonstrated that SE imaging can complement conventional STEM modes, offering access to the depth and topography information that is inaccessible by either phase contrast or (HA)ADF imaging [58]. It was shown that SE imaging aids in the explanation of the complex HAADF-STEM contrast that arises due to irregular shapes and compositionally diverse components. The particle shape and orientation can be directly observed from SE images (**Figure 2.2 a, b**). Additionally, SE imaging was used to study porous oxides that are ideal supports for catalysts. The SE image reveals that only a limited number of pores extend to the surface, and this may act as a bottleneck to gas exchange (**Figure 2.2 c, d**). With the development of aberration correctors, SE imaging with atomic resolution has been achieved [59, 60] followed by the theory explaining the image formation [61, 62]. SE imaging was furthermore combined with *in situ* heating to understand the behaviour of supported catalysts during thermal treatments (**Figure 2.3**) [63].

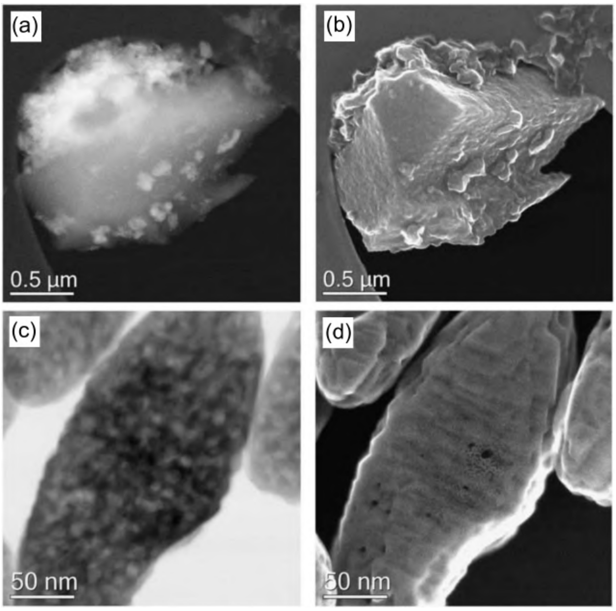

Figure 2.2: (a) HAADF-STEM and (b) SE images of the Fe-rich mineral particles supported on a slab-shaped biochar particle. (c) BF-STEM and (d) SE images of highly porous TiO_2 catalyst support. Despite the high degree of internal porosity, very few pores penetrate the surface. Reproduced with permission from [58]. Copyright 2016 Oxford University Press.

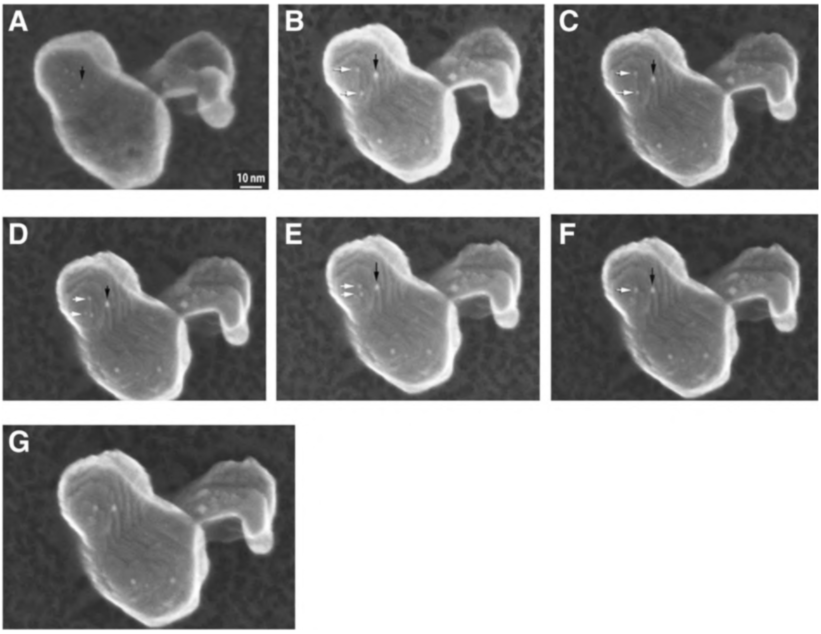

Figure 2.3: Sequence of SE images showing the development of facets on the support surface and movement and coalescence of nanoparticles at 700°C. Reproduced from [63] under the terms of the CC BY 4.0 license.

Besides superior spatial resolution, another advantage of SE imaging in STEM over SEM is the better useful signal to background ratio. The improvement can be explained by the lack of remote SE signals. SEs generated inside an electron microscope can be categorized into four types of signal, namely, SE-I, II, III, and IV (**Figure 2.4**) [23]. The SE-I signal originates from the incident point of the primary electrons in the specimen. Consequently, this SE image provides the highest resolution. The SE-II electrons are generated by backscattered electrons (BSEs) at the specimen's surface. SE-III electrons are electrons generated from the high-energetic BSEs reaching the pole-piece of the objective lens. SE-IV signal arises from BSEs created when other primary electrons have an impact on components inside the microscope. Both SE-III and SE-IV are unwanted (remote) signals for SE imaging, compromising image resolution and increasing the background signal. In STEM conditions, the BSE yield is very small (an order of magnitude lower than SE yield), and, therefore, the contribution of remote signals is negligible compared to SEM (SE-II) or even missing (SE-III and IV).

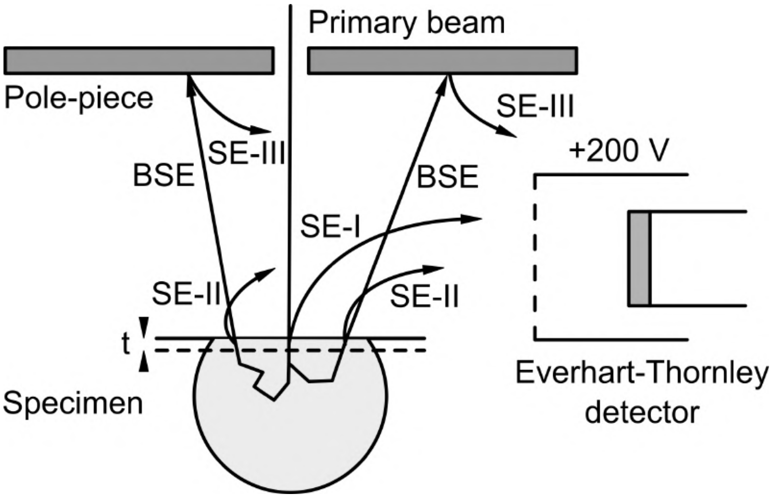

Figure 2.4: Origin of the different components of the SE signal generated in SEM. Based on [23].

Despite its demonstrated capabilities, SE imaging is not widely available in modern STEM instruments [58, 64]. One of the reasons for the poor availability of SE imaging in STEM is the complexity of its technical implementation. The low energy of SEs makes them difficult to detect in STEM since they are heavily affected by a strong magnetic field of the objective lens. Moreover, the pole-piece gap of the objective lens is very limited in size ($\approx$ 5 mm), making it impossible to place the detector inside it. To address this problem, modern STEM instruments equipped with SE detectors use the in-lens configuration mentioned previously (**Figure 2.5**). In this configuration, the ETD is located above the upper objective pole piece, and SE electrons reach it due to the spiralling effect as illustrated in **Figure 2.5**

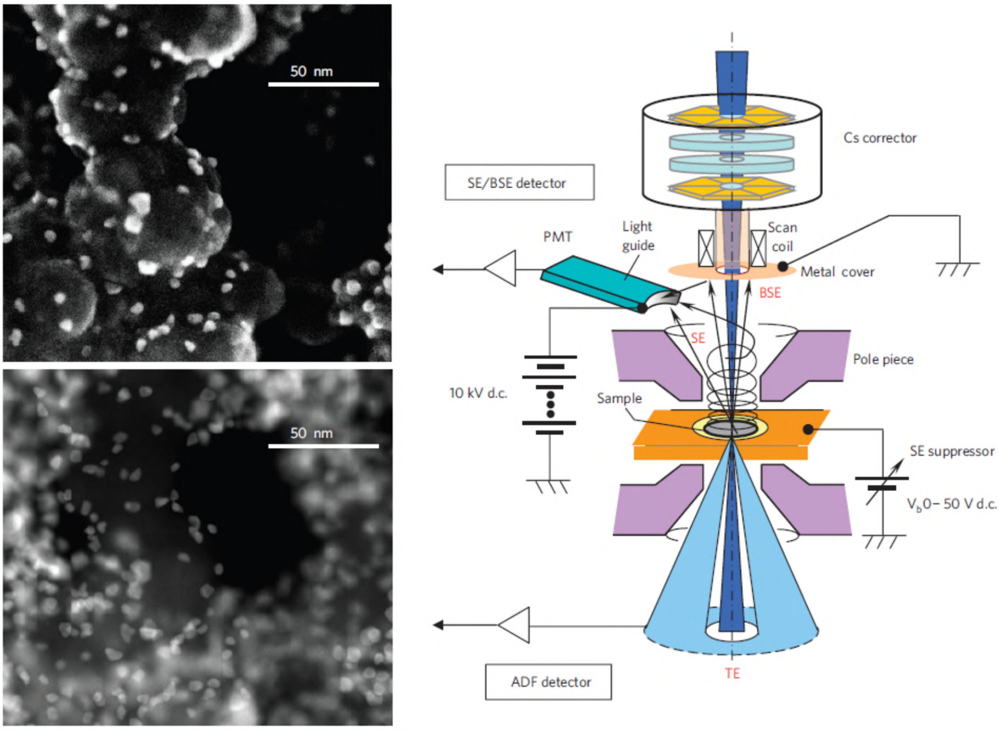

Figure 2.5: Overview of the experimental setup for the simultaneous acquisition of SE and STEM images installed in Brookhaven National Laboratory. Reproduced with permission from [59]. Copyright 2009 Springer Nature.

2.2 Secondary Electron Induced Current

Recently, an alternative approach to detect SEs has been proposed [65], based on a modification of the electron beam-induced current (EBIC) technique that has been widely used to analyze specific electrical properties of semiconductors [66]. EBIC conventionally measures the electrical current that originates when the primary electron beam interacts with the sample due to e.g. generation of electron-hole pairs, absorption of the electrons from the electron beam, or SE emission. Depending on that, EBIC can be split into three sub-techniques (**Figure 2.6**). The most well-known EBIC technique uses an electron beam to measure electron-hole pair recombination lengths and can map the current depletion region in a semiconductor p–n junction (**Figure 2.6 a**). In this mode, the current measured is greater than that of the primary electron beam. The other technique, which is called electron beam absorbed current (EBAC), uses EBIC to probe electrical shorts in embedded traces, where the absorbed electron current from the electron beam can be used as a diagnostic tool for probing disconnects (**Figure 2.6 b**). In this case, the measured current is approximately equal to the primary electron beam current. In SE-related EBIC (SEEBIC), the detected current arises from holes generated by the emission of SEs from the sample (**Figure 2.6 c**) [65]. The measured current here is generally much lower than the primary electron current since it relies on the SE yield of the specimen.

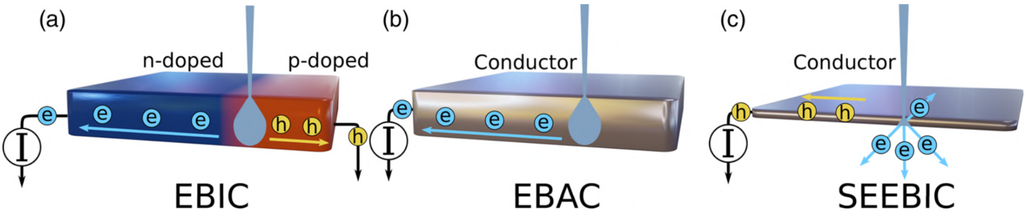

Figure 2.6: Schematics of the EBIC sub-techniques. (a) EBIC (b) EBAC and (c) SEEBIC. Reproduced from [64] under the terms of the CC BY 4.0 license.

All of these mechanisms are dependent on the interaction between the electron beam and specimen, electrical connections within the sample, and electrical connections to the sample. For example, EBAC is only possible when some measurable fraction of the primary electrons can be stopped within the conductive region of the specimen. This is typically not possible in STEM imaging conditions where almost all the electrons transmit through the sample. Likewise, SEEBIC requires the ejection of electrons from the surface, which only occurs within several nanometers of the surface. SEEBIC can attain higher imaging resolution because of the limited interaction volume, but this is at the expense of less signal current. It should be noted that for SEEBIC, the thickness of the specimen becomes essential to maintain the fraction of absorbed current to a minimum (negligible compared to SE emission current).

Figure 2.7 shows the schematic setup of a typical SEEBIC experiment. As mentioned previously, the SEEBIC current arises from holes generated by the emission of SEs from the ultra-thin sample on a conductive support. Next, this current flows to a current sensing transimpedance amplifier (TIA) and the detected signal is mapped as the primary beam is scanned over the sample area.

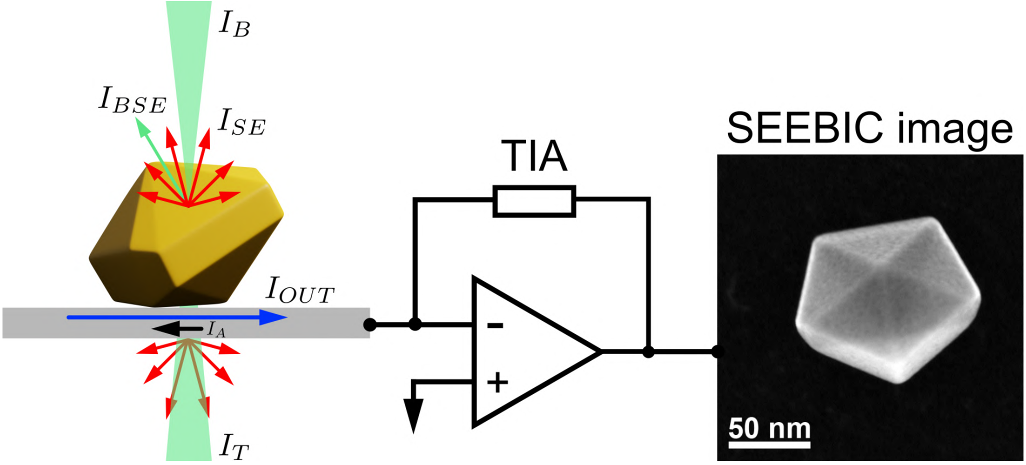

Figure 2.7: Schematic setup of the SEEBIC imaging concept with electrical current arising in the system.

In TEM conditions, when the electron beam is incident on the sample placed on ultra-thin conductive support, we approximate the steady-state current balance with **Equation 2.1** [65]

$$I_B = I_T + I_A + I_{BSE} + I_{SE} + \frac{V_S}{R_S} + I_{OUT} \tag{2.1}$$

where I_B is the primary electron beam current, I_T is the current of the transmitted electron beam, I_A is the absorbed current, I_{BSE} is the BSE emission current, I_{SE} is the SE emission current, V_S and R_S represent the local sample potential under the beam irradiation (e.g., charging due to SE emission) and the effective resistance to ground, and I_{OUT} is the current that can be measured.

In STEM conditions (accelerating voltage ≈ 100 kV and ultra-thin specimen is used), $I_T \approx I_B$, whereas I_A and I_{BSE} are negligible. In an electrically isolated area, SE emission leads to charging and $I_{SE} = -\frac{V_S}{R_S}$. If, instead, there is a low-impedance path to ground or a virtual ground consisting of the input to a TIA, little charging occurs, and a current $I_{OUT} = -I_{SE}$ is generated. Thus, the detected signal will be equal but opposite to the SE current flowing out of the sample. The detected signal can be mapped to produce an image that directly depends on the SE yield for each scan position.

The original paper by Hubbard *et al.* [65], which introduced the technique, has shown that SEEBIC reveals electronic properties of the sample through the position-dependent sample resistance (conductivity) and the SE yield which is dependent on the local work function. Later, it was demonstrated that lattice-resolution imaging is feasible [67]. The resistive contrast imaging capabilities of SEEBIC were shown as well allowing to visualize resistive grain boundaries in multilayer ceramic $BaTiO_3$ capacitors [68]. In SEEBIC, an emitted SE leaves a hole behind, which produces a positive current that also travels preferentially to one electrode or the other, depending on the resistance. Therefore, SEEBIC can also be used to compute a resistive contrast image (**Figure 2.8**) that can also be considered as a potential map of the sample.

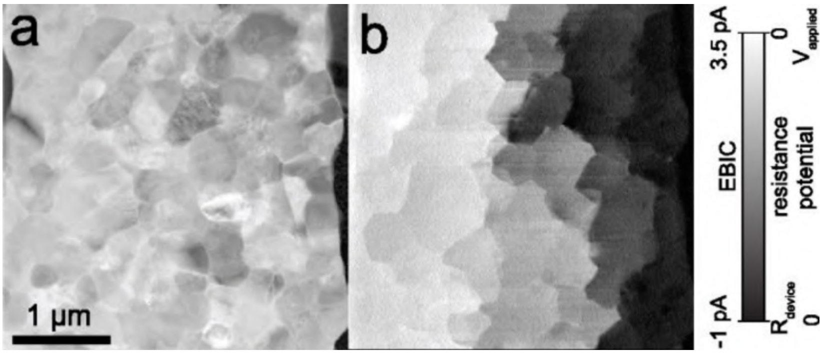

Figure 2.8: (a) ADF-STEM and (b) SEEBIC images of $BaTiO_3$ multilayer ceramic capacitor. SEEBIC image shown in (b) represents a resistive contrast image. Reproduced from [68] under the terms of the CC BY 4.0 license.

Recently *in situ* imaging of dielectric breakdown in $Pt/HfO_2/Ti$ valence change memory devices was reported [69]. STEM EBIC enabled direct visualization of the electronic signatures of dielectric breakdown, namely local changes in the conductivity and the electric field, with high spatial resolution and contrast. Dielectric breakdown was observed to proceed through two distinct regimes: a volatile, "soft" filament created by electron injection; and a non-volatile, "hard" filament created by oxygen-vacancy aggregation. Depending on the filament regime, different EBIC contrasts are possible. In low electric fields, SEEBIC dominates the contrast, whereas at high potentials standard EBIC contrast dominates the SEEBIC [69]. Two-channel SEEBIC imaging was used to characterize connectivity in two-terminal $SrTiO_3$-based memristor in STEM. SEEBIC images showed no leakage paths across the device confirming functionality of the fabricated thin-film oxide-based stack devices inside a TEM [70].

A series of papers by O.Dyck *et al.* have been issued, focusing on charge carrier transport in graphene-based nanodevices and the use of SEEBIC for device failure analysis [71, 72]. SEEBIC allowed a clear distinction between single and multilayer graphene and visualization of cracks in graphene sheets. Recently, spatially resolved imaging of electron density of an encapsulated WSe_2 layer was demonstrated [73].

A thermal response in the EBIC signal (both traditional EBIC and SEEBIC) was found that can be calibrated using EELS plasmon energy expansion thermometry (PEET) (**Figure 2.9**) [74]. EBIC thermometry is appealing for measuring temperature in operating electronic devices. Any TEM-compatible device that is electrically connected for *in situ* operation already satisfies many of the challenging requirements for compatibility with STEM EBIC. Unlike PEET, EBIC does not require the complicated fitting of 3D datasets, and it is relatively agnostic to the specific materials used for thermometry as long as the device architecture provides a measurable EBIC signal.

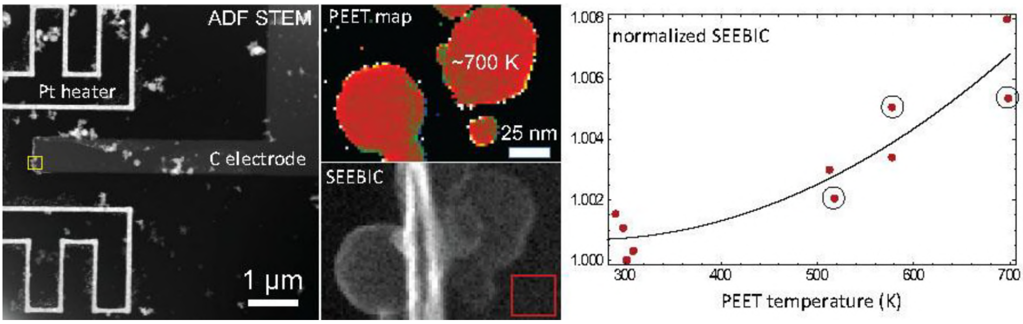

Figure 2.9: Illustration of the SEEBIC thermometry calibration with plasmon energy expansion thermometry. Reproduced with permission from [74]. Copyright 2020 Oxford University Press.

It was shown that adjusting the voltage between the pole piece of the microscope and the sample holder can modify the SEEBIC contrast (**Figure 2.10**) [75]. Positive potential relative to the pole piece attracts low-energy SEs back to the holder, decreasing the SEEBIC signal, whereas negative holder potential leads to an increase in signal, as the local electric field encourages SEs to escape. This property of SEEBIC can be used to enhance the signal, for example, in conditions where the use of high electron doses is impossible due to beam damage of the sample. Moreover, the ability to control the potential between the holder and the pole piece enables the measurement of work functions [65].

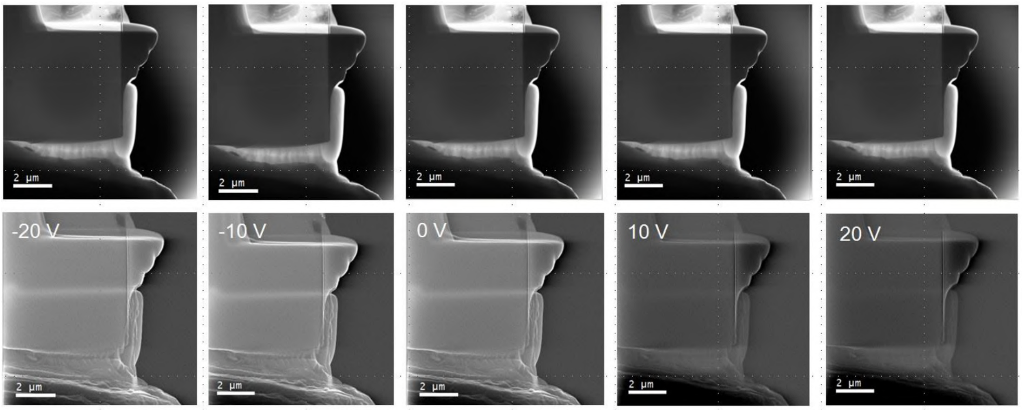

Figure 2.10: ADF-STEM (top row) and SEEBIC (bottom row) images at different holder bias values relative to the pole piece. Reproduced with permission from [75]. Copyright 2019 Oxford University Press.

2.3 Practical Aspects of SEEBIC

The typical SEEBIC-STEM experimental setup consists of the following key elements: (1) electrical interface with a sample; (2) current amplifier; and (3) analog-to-digital converter. The first stage is usually employed by a micro-electromechanical system (MEMS) device in combination with biasing TEM holder to create an electrical connection between the sample in vacuum and the measuring device. STEM-compatible chips that enable the electrical biasing of samples are commonly available through several vendors (e.g., DENSsolutions, Protochips, Hummingbird Scientific). Moreover, the fabrication of custom-made substrates for the design and operation of experimental devices is also common [71, 76, 77]. Such devices are usually fabricated using optical and/or electron beam lithography and feature lithographically patterned electrodes that interface with the electrical contacts on the TEM holder via contact pads. A biasing MEMS device consists of a few hundred μm-thick Si with electron transparent SiNx window with electrodes (depicted as sample area in **Figure 2.11**). Optionally, the device may contain a heating spiral to perform *in situ* heating during the biasing experiment. An example of a device architecture that can be used for the SEEBIC experiment is shown in **Figure 2.11**.

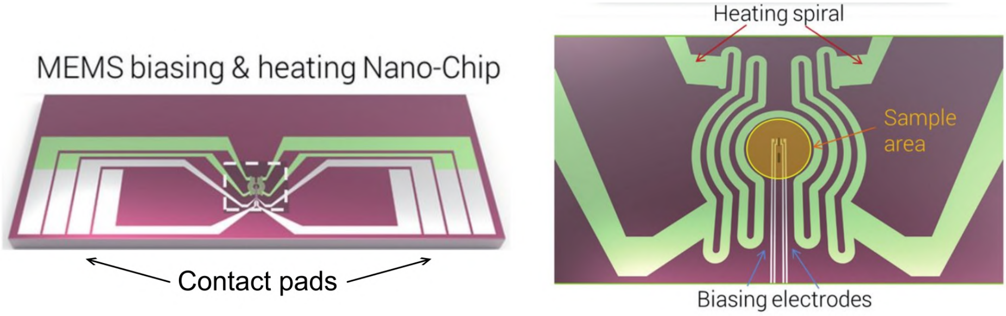

Figure 2.11: Example of device architecture that can be used for the SEEBIC experiment: DENSsolutions MEMS heating & biasing Nano-Chip with indicated features [78].

The next component of the SEEBIC experimental setup is a current-to-voltage amplifier or transimpedance amplifier. This is a critical part of the setup since the measured SEEBIC signal is very low (sub-pA range), and therefore, it requires a dedicated approach to design and needs to be discussed in detail. A TIA can be implemented conveniently with an integrated operational amplifier (op-amp) as shown in **Figure 2.12**. The op-amp's non-inverting (+) input is grounded, and a feedback resistor (R_F) is connected between inverting (-) input and output. The input current (I_{IN}) flows entirely through the feedback resistor, and the op-amp adjusts its voltage output to keep its inputs at equal voltages. The DC and low-frequency gain of a TIA is measured in V/A set by R_F value and determined by **Equation 2.2**.

$$V_{OUT} = -I_{IN} R_F. \tag{2.2}$$

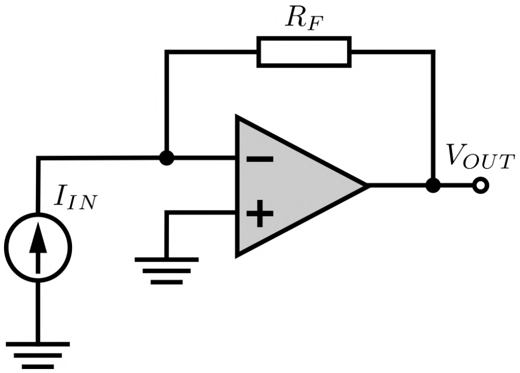

Figure 2.12: Simplified transimpedance amplifier circuit.

TIAs are often encountered in photodetector circuits where a photocurrent generated in a photodiode or photomultiplier tube is converted into a measurable voltage signal. Designing such amplifiers is challenging as a compromise between competing requirements has to be met such as (1) stability of the circuit; (2) bandwidth (or speed); and (3) noise.

Transimpedance amplifiers are frequently susceptible to oscillation at high frequencies caused by the stray capacitance of the current source as shown in **Figure 2.13**. To ensure stability, a compensation capacitor C_F connected in parallel with the feedback resistor is used. It should be noted that during the SEEBIC experiment, the geometry of the setup (MEMS device, TEM holder and cabling) is responsible for this input capacitance and care needs to be taken to keep this capacitance as low as possible to maintain the stability of the amplifier. This will allow to reach improved performance. The bandwidth of a TIA is inversely proportional to R_F and C_F, therefore, high-speed applications require optimization of these values to maintain TIA stability and keep noise at a reasonable level. The stability and noise performance of the amplifier requires careful consideration according to specific design needs and will be discussed in detail in the next chapter.

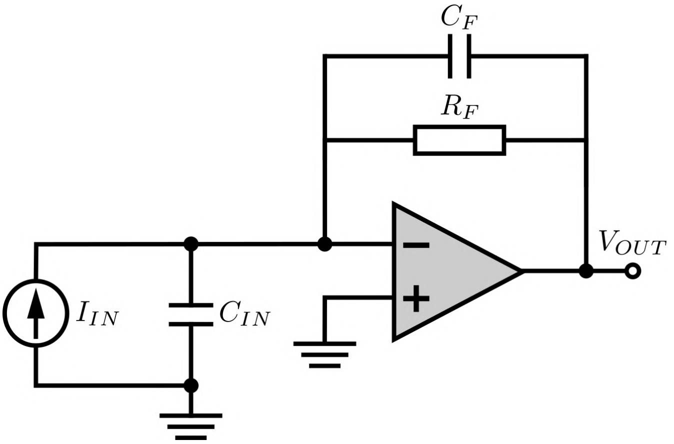

Figure 2.13: Realistic transimpedance amplifier circuit.

At the final stage of the SEEBIC experimental setup, the voltage output of the TIA is connected to the analogue-to-digital converter included in the scan engine of the microscope and controlled by software via a PC. The scan engine controls the scan coils of the microscope and synchronizes the measured signal with a beam position. Experimental parameters such as dwell time, sampling, gain and offset can be controlled at this stage.

2.4 Conclusions

So far, SEEBIC studies have been primarily used to investigate the electronic properties of materials, with a main emphasis on the importance of the technique for failure analysis and characterization of nanoelectronic devices. However, the capability of SEEBIC to produce topography-sensitive SE images was not fully explored, even though SE imaging in STEM is known to be a powerful complementary technique. SEEBIC can overcome the disadvantages of SE-STEM imaging (mainly the unavailability of SE detectors in existing STEM instruments) limiting its application in the EM community. In this PhD thesis, this aspect of SEEBIC will be exploited. The use of SEEBIC as an alternative technique to provide 3D information about surface morphology with high spatial resolution will be discussed. SEEBIC will be used to overcome the lengthy acquisition and reconstruction procedures needed in ET.

Chapter 3

Design of a SE Detection Setup for Use in TEM

This chapter discusses the main requirements for the design of a transimpedance amplifier for use as a part of the SEEBIC setup. The design of the SEEBIC-optimized solution is proposed. Next, the performance of the proposed design is characterized and further improvements are suggested.

3.1 Introduction

In STEM, the number of SEs per incoming electron, or the SE yield (δ), does not exceed 0.005 in the primary electron energy range of 100-200 keV [79]. Therefore, the measured SEEBIC signal is typically in the sub-picoampere range. To amplify the signal to a level that can be handled by the scan engine of the microscope, a TIA with a gain of $\approx 10^9$ V/A is required. Previous studies show successful use of the commercially available DLPCA-200 (FEMTO Messtechnik GmbH) TIA for SEEBIC experiments [65, 71]. Even though this product has an appropriate gain for most SEEBIC measurements, its bandwidth at a maximum gain is 1.1 kHz, which limits scan speed and adversely affects high-resolution imaging due to spatial drift. Additionally, it could result in a higher accumulated electron dose and consequential beam damage. Moreover, the electrical connection of this amplifier to the biasing TEM holder creates unwanted input capacitance that negatively affects the noise performance of the experimental setup. To overcome these challenges I have designed and characterized a custom TIA that can directly be plugged into DENSsolution biasing holder. This solution effectively reduces the effect of input

---

This chapter is based on the following paper:

Vlasov E., Bals S., Verbeeck J. Design and characterization of a transimpedance amplifier for electron beam-induced current measurements in scanning transmission electron microscope (in preparation).

The contribution of the author of the thesis consisted of designing and implementing the transimpedance amplifier. Analysis of the stability and noise performance of the proposed design, as well as experimental characterization of the design were done in collaboration with Prof. Dr. J. Verbeeck.

capacitance on SEEBIC measurements while providing a higher bandwidth than the commercial analogue.

3.2 TIA Design Considerations

SEEBIC visualisation of morphological features implies a set of requirements for a TIA design which are discussed below. First of all, the amplifier gain should be above 10^9 V/A to be able to amplify the expected low current SEEBIC signal to an output signal in the range of a few volts. Moreover, the bandwidth of the TIA design needs to be above 5 kHz to allow for a dwell time lower than 200 μs (that corresponds to an acquisition time of 1 minute for 512×512 image). To satisfy the selected design requirements we have chosen the design shown in **Figure 3.1**

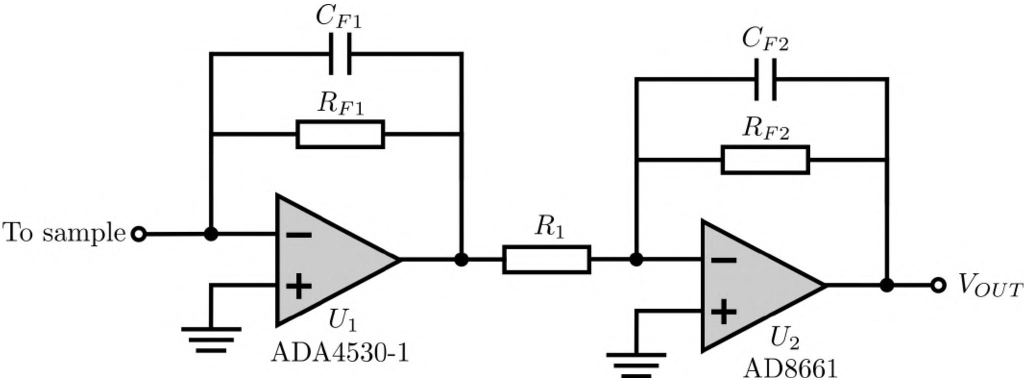

Figure 3.1: Proposed TIA design consisting of two stages with a total gain of 2×10^9 V/A. The gain of the first stage is 200 MV/A (defined by R_{F1}), and the gain of the second stage is 10 V/V (defined by R_{F2}/R_1 ratio).

This design uses a cascade topology (TIA built on U_1 with a gain of 200 MV/A followed by a voltage amplifier built on U_2 with a gain of 10 V/V) to maintain sufficient bandwidth and total gain above 10^9 V/A (2×10^9 V/A in this case) at an acceptable noise level. In this section, we consider only the first stage of the circuit (its stability and noise performance) since it is the most critical part of the design as noise created in this stage can not be undone in later stages without compromising bandwidth. The TIA design uses feedback resistor R_{F1} = 200 MΩ and feedback capacitor C_{F1} = 0.1 pF. The bandwidth of the TIA is defined then by cut-off frequency f_c (**Equation 3.1**).

$$f_c = \frac{1}{2\pi R_{F1} C_{F1}} \approx 8\ kHz, \tag{3.1}$$

The low current requirement implies the use of dedicated op-amps that are optimised for this task. For this design, we have chosen the ADA4530-1 (Analog Devices) op-amp that is optimised for electrometer circuits. This op-amp has ultralow input bias current (< 1 fA) which is crucial for the precision and ultimate noise performance of the TIA, relatively low input capacitance (8 pF) and a gain bandwidth product of 2 MHz (GBWP) which is sufficient to obtain the required bandwidth.

3.2.1 Stability Considerations

As was mentioned in the previous chapter, in a practical setting, the input capacitance of the current source (**Figure 2.13**) destabilizes the TIA. Prior to the analysis of the stability, an adequate estimation of the input capacitance of the setup is required. We assume that the major capacitance present in the setup originates from the TEM holder. This capacitance can be estimated as the capacitance of a coaxial cylindrical capacitor

$$C = \frac{2\pi\varepsilon_0 k}{ln(^b/_a)}, \tag{3.2}$$

where a and b are the inner and outer radii of the holder, L is the length of the holder, ε_0 is the permittivity of vacuum, and k is dielectric constant. For $\frac{b}{a} = 5$, $L = 25$ cm, we get an estimate of the input capacitance of 9 pF. This value closely correlates with the one we measured for a DENSsolution Wildfire holder (9 ± 2 pF). Here, we assume a total input capacitance $C_{IN} \approx 20$ pF to have a margin for the amplifier stability and take into account the input capacitance of the op-amp and an unaccounted capacitance that might be related to e.g., the sample.

Given input capacitance, the destabilizing effect of C_{IN} can be investigated based on the phase margin. Phase margin is defined as the difference between the phase at gain crossover frequency f_z and -180°. In the context of a TIA, a higher phase margin (above 45°) typically indicates greater stability, meaning the system is less likely to exhibit oscillatory or unstable behaviour. For simplicity, the phase margin of the circuit can be expressed in terms of the rate of closure (ROC) [80]. ROC is defined as the difference between the slopes of the open-loop gain (A_{OL}) and inverse feedback network transfer function ($1/\beta$, known as the noise gain) at the crossover frequency (f_x). Generally, a ROC less than 30 dB/dec (in the ideal case, ROC of 20 dB/dec is considered to be optimal for stability) ensures a stable circuit with some safety margin. A rate of closure greater than 30 dB/dec is moving towards an unstable circuit condition.

$$\phi_m \approx 180° - 4.5 \times ROC(dB/dec) \tag{3.3}$$

Physically, C_{IN} and R_F establish a complex pole within the feedback loop ($f_z = {}^1/_{2\pi R_F C_{IN}}$). Consequently, a signal travelling around the feedback loop will have to contend with two poles, one due to the op-amp and the other due to C_{IN}, with the risk of a phase shift approaching 180° (ROC of 40 dB) and thus jeopardizing circuit stability leading to the peaking of TIA gain of the circuit at high frequencies (as shown in **Figure 3.2 b**). However, adding capacitor C_F to the feedback loop can stabilize the circuit by shifting the feedback pole to lower frequencies ($f_z' = {}^1/_{2\pi R_F (C_{IN}+C_F)}$) and creating a second pole of $1/\beta$ ($f_p = {}^1/_{2\pi R_F C_F}$) (**Figure 3.2 c**). Minimal C_F value to comply with feedback loop stability can be estimated using the simplified **Equation 3.4**

$$C_F = \frac{C_{IN}}{2\pi R_F f_t}, \tag{3.4}$$

where f_t is the GBWP determined by the op-amp selection [80].

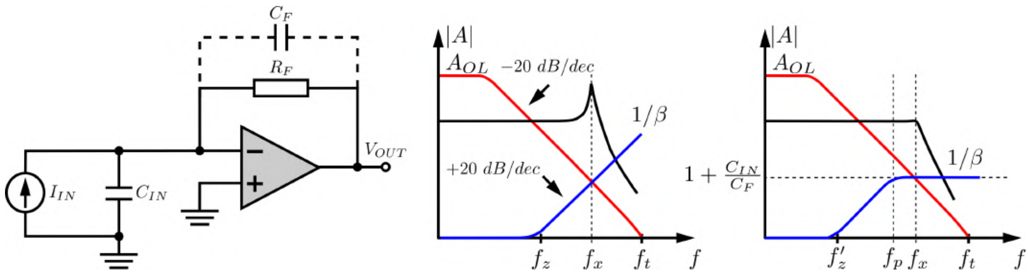

Figure 3.2: Schematic of TIA and corresponding Bode plots showing an unstable and stable circuit.

Based on **Equation 3.4**, a minimum feedback capacitance of 0.09 pF is required, which justifies our choice of C_{F1} = 0.1 pF. The analysis of our TIA design was done in the LTSpice software which solves the series of coupled differential equations representing the potentials and currents in the circuit based on the SPICE simulator [81]. Obtained Bode-plots of A_{OL} and $1/\beta$ are shown in **Figure 3.3**. From the Bode plots, it can be seen that indeed the uncompensated circuit shows TIA gain peaking at high frequency (**Figure 3.3 a**). On the other hand, the compensated TIA (with C_{F1} in place) demonstrates an almost flat response at high frequencies (**Figure 3.3 b**). It should be noted that in our simulations we used a C_{F1} value of 0.1 pF, however, even though this value corresponds to the one we chose for our design implementation, in reality, this value will be slightly higher due to parasitic capacitance associated with R_{F1} and printed circuit board (PCB) layout providing some extra margin in the stability of the circuit.

Figure 3.4 shows Bode-plot of the proposed design shown in **Figure 3.1**. It can be seen that the TIA demonstrates flat frequency response in the desired range up to 8 kHz.

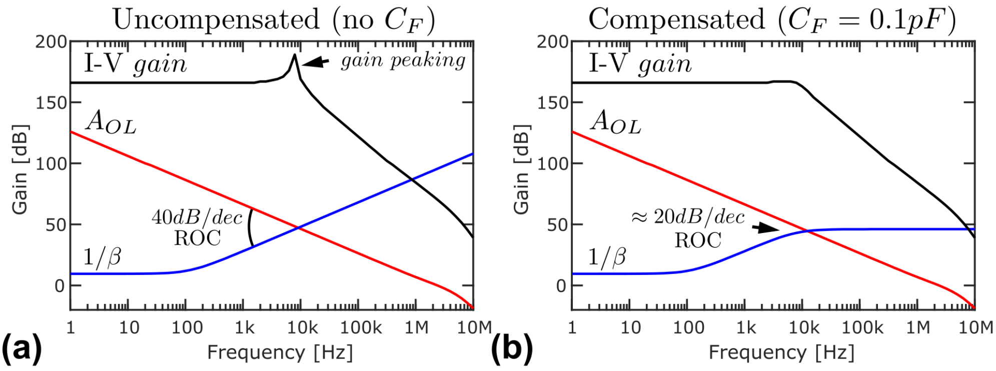

Figure 3.3: Bode plots of the open-loop gain (A_{OL}), noise gain ($1/\beta$) and I-V gain for (a) uncompensated and (b) compensated TIA.

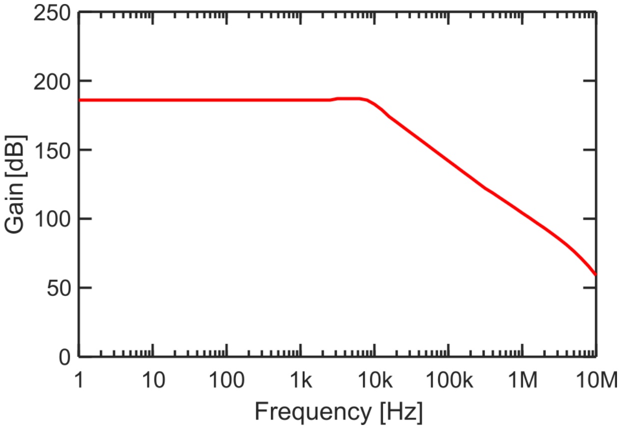

Figure 3.4: Bode plot of the proposed TIA design.

3.2.2 Noise Analysis

Photodiode TIA circuits have four noise sources (input-referred) that must be considered (**Table 3.1**) [82].

Type of noise	Formula	Value
Shot (Poisson) noise	$i_{Nshot} = \sqrt{I_{IN} e}$	0.4 fA/$\sqrt{Hz}$ @ I_{IN}=1 pA
Johnson noise	$i_{Nth} = \sqrt{\frac{4k_B T \Delta f}{R_F}}$	9 fA/$\sqrt{Hz}$
Input current noise	i_N as specified	0.07 fA/$\sqrt{Hz}$
Input voltage noise	v_N as specified	14 nV/$\sqrt{Hz}$

Table 3.1: Major sources of noise in TIA design.

Shot noise originates from the discrete nature of the electric charge, whereas Johnson noise is the thermal noise of the feedback resistor R_F. The input current noise is the intrinsic characteristic noise of the op-amp input and in most cases (and in ours) does not significantly affect the noise performance of the circuit. The last noise source is input voltage noise (v_N) that produces a noise between non-inverting and inverting terminals of the op-amp which gets converted into a current (I_{vN}) by any parallel impedance between the sense input and the reference voltage. This parallel input impedance we call Z_{IN} can consist of leakage resistance (or shunt resistance of a current source, R_S) and capacitance C_{IN} that includes the capacitance of the current source and input capacitance of the op-amp (**Figure 3.5**). This may well be an important source of noise, especially when the input capacitance is high. It should be noted, that in general, Johnson noise of a shunt resistor R_S also needs to be considered as a noise source. However, the measured R_S value is in the TΩ range making this contribution one order of magnitude lower than the current noise of the op-amp. Therefore, the thermal noise of the shunt resistor can be excluded from the consideration.

In the ideal case, the total noise of the TIA should be as close as possible to the shot-noise limit as this is the only fundamental noise source that can not be avoided. Simple estimations show that the input-referred shot noise is one order of magnitude lower than Johnson noise (**Table 3.1**) of R_F, and to achieve a Johnson noise level comparable to the shot-noise, R_F needs to be increased by a factor of 400, which is impractical for SEEBIC applications as bandwidth (speed) of the amplifier will be reduced proportionally forcing us to use unrealistically long dwell times.

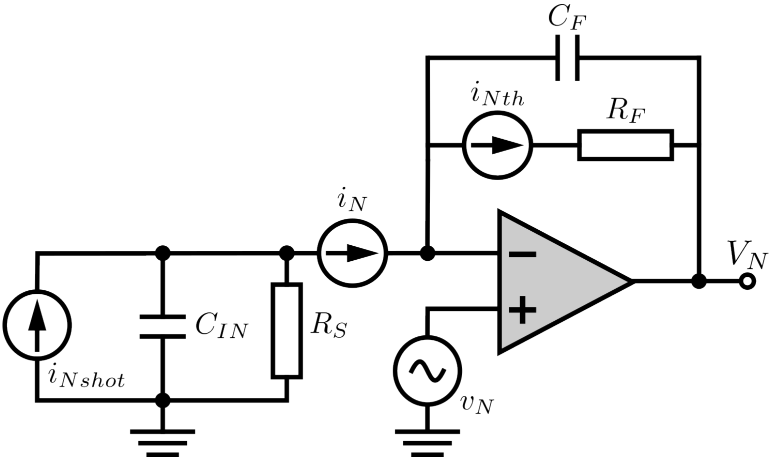

Figure 3.5: Noise model of TIA.

The noise contributions of all sources are typically referred to the output for analysis. To obtain noise plots of V_{Nshot}, V_{Nth} and V_{iN}, corresponding input-referred currents (i_{Nshot}, i_{Nth} and i_{iN}) need to be multiplied by the transimpedance transfer function $T_z(f)$ (**Equation 3.5**).

$$T_z(f) = \frac{Z_F(f)}{1 + \frac{1}{A_{OL}(f)\beta(f)}}, \tag{3.5}$$

where $A_{OL}(f)$ is frequency-dependent open-loop gain of the op-amp, $\beta(f)$ is the feedback network transfer function (**Equation 3.6**), $Z_F(f)$ is impedance of parallel circuit formed by R_F and C_F (**Equation 3.7**), and $Z_{IN}(f)$ is input impedance (**Equation 3.8**).

$$\beta(f) = \frac{Z_{IN}(f)}{Z_{IN}(f) + Z_F(f)} \tag{3.6}$$

$$Z_F(f) = \frac{1}{\sqrt{\frac{1}{R_F} + 2\pi f C_F}} \tag{3.7}$$

$$Z_{IN}(f) = \frac{1}{\sqrt{\frac{1}{R_S} + 2\pi f C_{IN}}} \tag{3.8}$$

The calculation of V_{vN} noise spectrum is a less trivial task. The op-amp input voltage noise (v_N) is converted into a current by a parallel input impedance. V_{vN} spectrum then can be obtained from:

$$V_{vN}(f) = v_N \frac{A_{OL}(f)}{1 + A_{OL}(f)\beta(f)} \tag{3.9}$$

Figure 3.6 shows noise density plots for all noise sources. It can be seen that the dominant sources in our design are the thermal noise of the R_F resistor and the input voltage noise of the op-amp. It should be noted that both of them can be reduced by adjusting the proposed design. For example, thermal noise can be reduced by increasing the R_F value, but this will lead to a reduction of bandwidth ($V_{Nth} \propto 1/\sqrt{R_F}$ and BW $\propto 1/R_F$). An alternative approach would be cooling the system to lower temperatures. However, the reduction of the R_F noise by a factor of two requires the temperatures down to 75 K which also might be impractical. On the other hand, V_{vN} contribution can be reduced by reduction of the input capacitance of the setup (e.g. placing the amplifier closer to the sample and choosing an op-amp with lower input capacitance and/or lower input voltage noise).

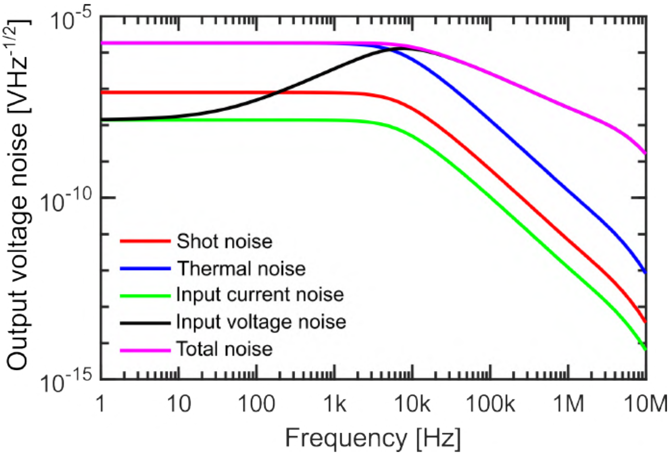

Figure 3.6: Noise spectra for all noise sources.

To convert each noise spectrum into its contribution to the rms noise voltage at the output, their noise power spectra need to be integrated over the entire frequency range (see **Equation 3.10** for the shot noise as an example).

$$V_{Nshot\ rms} = \sqrt{\int_0^{f_t} V_{Nshot}^2 df} \tag{3.10}$$

The sum in quadrature of all the noise sources (since they are uncorrelated) results in the total output-referred rms voltage noise of the first stage:

$$V_{N1\ rms} = \sqrt{V_{Nshot\ rms}^2 + V_{Nth\ rms}^2 + V_{iN\ rms}^2 + V_{vN\ rms}^2} \tag{3.11}$$

The contribution of each component to the total rms noise of the first TIA stage can be found in **Table 3.2**.

Type of noise	**Value** [μV_{rms}]
Shot (Poisson) noise	6.12 @ I_{IN}=1 pA
Thermal noise of R_F	139.08
Input current noise	1.07
Input voltage noise	227.76
Total output voltage noise	266.94

Table 3.2: Contributions of all noise sources to total output-referred rms voltage noise.

It should be noted that the contribution from the input voltage noise becomes dominant at high frequencies above the bandwidth of the TIA (**Figure 3.6**). This noise has an important weight in the total rms voltage as the frequency range where this noise is important is high, which can appear misleading on a log-log scale plot. Further low pass filtering with a cutoff around 8 kHz will strongly suppress this noise without significantly altering the signal.

The total output noise of TIA can be estimated from the noise of the first stage multiplied by the gain of the second stage (10 V/V) and the noise of the second stage. However, the amplified noise of the first stage is dominant compared to the noise of the second stage, therefore, the noise of the second stage can be neglected (LTSpice simulations show that this assumption introduces an error of 1% to the total rms noise). The factor of 10 assumes that the second stage has no bandwidth limit, however, it would be wise to choose its bandwidth limit equal to the bandwidth of the first stage to filter out high-frequency noise contribution from the voltage noise.

$$V_{N\ rms} = \sqrt{V_{N1\ rms}^2 + V_{N2\ rms}^2} \approx V_{N1\ rms} = 2.667\ mV. \tag{3.12}$$

3.2.3 Board Layout

In this section, we will discuss a PCB layout of our TIA design. The TIA was designed on a four-layer FR4 PCB to provide shielding, low inductance, and controlled capacitance. RF shielding using a RF can (Faraday cage) of the first amplification stage was implemented to avoid electromagnetic interference in the circuit.

Low current measurements such as SEEBIC can create insulation resistance requirements that are unrealistically high. Fortunately, a technique called "guarding" can reduce these requirements to a reasonable level. A "guard" is a driven trace (or shield) that physically surrounds the input trace and feedback circuitry and is held at a potential equal to the reference potential. Since the input circuitry and the guard are kept at the same potential, the leakage current between the two nodes (I_{leak}) is zero. The guard is a low-impedance node, so any external leakages will "leak" into the guard and not into the protected input (**Figure 3.7 a**). The guard potential may be taken from the non-inverting input or reference voltage as shown in **Figure 3.7 b**. The ADA4530-1 uses guarding techniques internally, and it has a high-performance guard buffer integrated. The output of this buffer is made available externally to simplify the implementation of guarding at the circuit level. We used a guard ring technique to implement the guarding on the surface of the PCB. The solder mask was removed from the high-impedance trace (input) and the guard trace to ensure that the guard makes electrical contact with any surface leakage paths. The guard ring was extended around the input pin, R_{F1} and C_{F1} to ensure that the entire high-impedance node was surrounded by the guard (**Figure 3.7 c**). The guard ring is directly driven from the ADA4530-1 guard buffer. Additionally, a guard plane was used to implement the guarding through the bulk of the PCB material. The guard plane is a filled copper shape that is placed directly below the high-impedance trace. This plane is connected to the guard ring on the surface layer with vias.

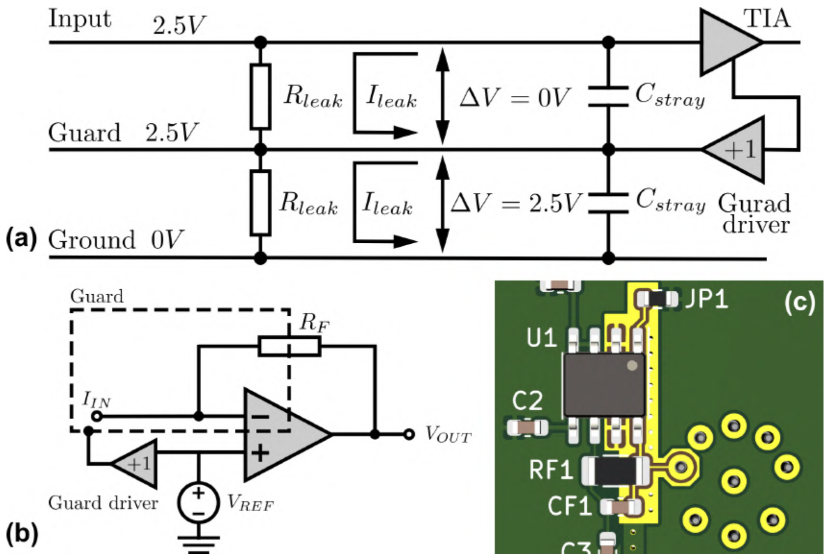

Figure 3.7: (a) Guarding theory schematic, (b) schematic of guarding principle for TIA circuit, (c) implementation of guarding in current design.

It should be noted that the effective insulation (shunt) resistance of the TIA circuit can also be substantially degraded if the PCB surface is contaminated. Solder flux, body oils, dust, and dirt are all possible sources of contamination. Some of these contaminants form a parallel leakage path across the surface of the existing insulator, effectively lowering the insulation resistance and creating a new noise source (Johnson noise of shunt resistor). Thorough cleaning and guarding techniques help to suppress these effects.

3.3 Carrier Board Design

Previous studies show the use of MEMS devices for performing SEEBIC experiments. The design and fabrication of such MEMS chips are time-consuming and require complicated and expensive equipment that does not lend itself well to rapid prototyping but holds benefits in terms of volume production and vacuum behaviour. In our study, we created a sample carrier based on a 0.6 mm thick FR4 printed circuit board, designed to fit in a DENSsolutions Wildfire heating holder which allows the use of a conventional copper TEM grid as a support for a sample (**Figure 3.8**).

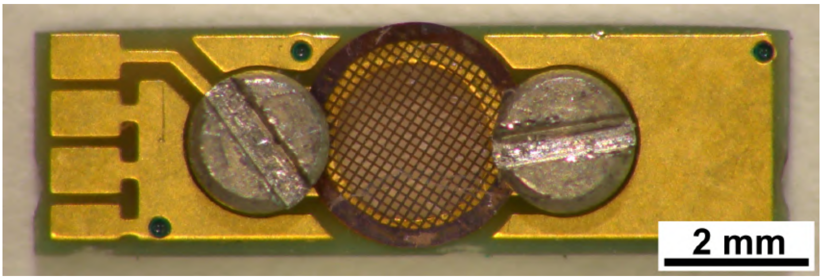

Figure 3.8: Sample carrier printed circuit board with attached TEM grid.

3.4 Experimental Validation of the Design

First, we measured the output rms noise of the designed TIA. The measured value of 4.09 mV is in close agreement with our estimations. Next, we estimated the noise of the SEEBIC setup including the TIA and analog-to-digital conversion in the scan engine. For that, we collected a series of images using our SEEBIC setup with a blanked electron beam with different dwell times (125, 250, 500 and 1000 μs). The noise from the images was estimated as the square root of the variance of the intensity multiplied by the step size of the digital-to-analog converter (input range divided by digital-to-analog converter resolution). The measured values are shown in **Figure 3.9** as red crosses. These values were compared with the calculated noise taking into account the integration time of the digital-to-analog converter (dwell time). In the time domain, the integration of the signal with a digital-to-analog converter can be approximated as a convolution of the signal with a box function that has a width equal to the chosen dwell time. In the frequency domain that corresponds to a product of the signal (noise spectrum in our case) with a $sinc$ function:

$$V_{n,T} = \sqrt{\int_0^{f_t} V_n^2(f) sinc^2(fT) df} \tag{3.13}$$

The comparison shows a discrepancy between the noise estimated from the images and the calculated noise. The difference between measured and calculated noise can be attributed to the residual pickup noise from other sources. To explore this we analysed the noise measured from images in the frequency domains, which is essentially a time series of AC conversion of the analog signal, converted to the frequency domain using a fast Fourier transform.

Figure 3.10 shows such Fourier transform of the measured data (image obtained with 125 μs dwell time). Two distinct peaks can be seen at ≈ 600 and 1100 Hz. The peak at 1100 Hz can likely be attributed to the interference from the turbopump of the microscope. Turbopumps can run up to 1400 Hz (84000 rpm) and are precisely frequency controlled. In normal operation, the turbopump runs at 80% of its speed which corresponds to ≈ 1100 Hz. A lower frequency 600 Hz noise can perhaps be related to internal signal from the brushless DC motor driver of the pump.

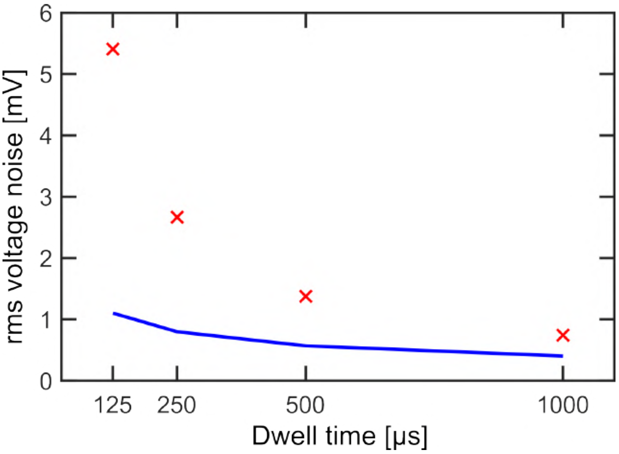

Figure 3.9: Dependence of rms voltage noise on dwell time. The blue curve represents calculated noise and red crosses represent values estimated from the noise images.

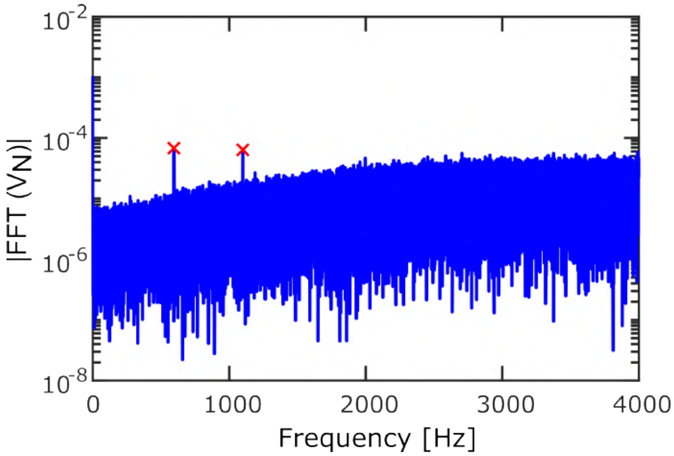

Figure 3.10: Noise spectrum obtained from the images. Red crosses indicate peaks at ≈ 600 and 1100 Hz.

3.5 Outlook

To further improve the noise performance of the system, the amplifier needs to be as close as possible to the sample to avoid unwanted extra input capacitance. This can be done by the fabrication of a dedicated TEM holder for SEEBIC measurements where the first amplifier stage is built as close as possible to the sample. It should be noted, that a system with integrated TIA was recently released by Hummingbird Scientific in collaboration with NanoElectronic Imaging [83]. However, the author of the thesis is not aware of the detailed specifications of this product and cannot make conclusions about the performance and design choices of this system. Another solution to reduce the effect of input capacitance is to use the common-base transistor amplifier that transmits its emitter current to its collector while keeping its emitter at a roughly constant voltage.

Therefore, the input of TIA is isolated from C_{IN}, reducing the input voltage noise contribution [82].

The bandwidth of the TIA can also be improved by using a combination of ultra-fast op-amps and advanced PCB layout techniques. For example, the op-amp with a high gain bandwidth product (e.g. LTC6268, GBWP = 500 MHz) can provide enough margin for decreasing the C_F value and keeping the TIA stable. In this case, C_F can be omitted from the design since the parasitic capacitance of R_F and PCB traces becomes sufficient to compensate for the destabilizing effect of C_{IN}. This parasitic capacitance can be reduced even more (down to 7 fF) with the use of advanced layout techniques and dedicated PCB materials allowing to significantly increase the bandwidth of TIA [84]. Whether the proposed improvements will bring us much closer to a shot noise-limited experiment remains to be seen, but we estimate that significant progress in noise behaviour and/or bandwidth is possible.

Chapter 4

Secondary Electron Electron Induced Current as a Method to Visualize the Morphology of Nanoparticles

This chapter focuses on the development of SEEBIC as an alternative way for the visualization of the morphology of nanoparticles. The time- and dose-efficiency of SEEBIC are tested in comparison with conventional ET. High spatial resolution is shown compared to SEM. Finally, contrast artifacts arising in SEEBIC images are described, and their origin is discussed.

4.1 Introduction

As mentioned in **Chapter 1**, the properties of nanomaterials can be tuned by changing their size, shape, composition, and crystal structure. For example, shape control is a very important field for the design of plasmonic structures since the shape has a strong influence on optical properties than particle size [47]. Especially in the field of the formation of anisotropic Au nanostructures, where considerable research is ongoing [14, 47, 85]. The variety of synthesised shapes includes rods, wires, prisms, cubes, stars, tetrapods, and others. Although the typical seeded-growth synthesis of such nanoparticles is well controlled, essential feedback about desirable NP shapes and features is often required. ET is an indispensable tool for such studies. However, ET suffers from high

---

This chapter is based on the following paper:

Vlasov E., Skorikov A., Sánchez-Iglesias A., Liz-Marzán L.M., Verbeeck J., Bals S. Secondary electron induced current in scanning transmission electron microscopy: an alternative way to visualize the morphology of nanoparticles. *ACS Mater. Lett.*, 1916 (2023).

The contribution of the author of the thesis consisted of implementing the setup for measurement of the SEEBIC signal, setting up and conducting experiments; SEEBIC, HAADF-STEM, ET and SEM data acquisition, and processing. Synthesis of gold Ino decahedra and nanotriangles was carried out by the research team of Prof. Luis M. Liz-Marzán from the BioNanoPlasmonics Laboratory at CIC biomaGUNE, Spain.

recording times and complex aquisition procedures limiting the amount of particles that can be investigated with reasonable effort and time. Thus, new approaches to retrieve the morphology of nanomaterials in (S)TEM are needed since understanding of average structure of the sample requires statistics over hundreds of nanoparticles, which is impractical with ET. Here, we propose surface-sensitive SE imaging as an alternative to ET. The technique may provide us with topographical information from a single image allowing a time-efficient investigation of a broad range of the samples.

4.2 Materials and Methods

In this work, we have studied Au NPs with different shapes: triangular platelets and Ino decahedra (**Figure 4.1**). An Ino decahedron contains 5 small lateral facets between the 10 facets of a perfect decahedron [86]. Ino decahedra were synthesized through a modification of a recently reported method [87], but using pre-formed pentatwinned Au nanorods as intermediate seeds. Au nanotriangles were synthesized using the method reported in reference [88].

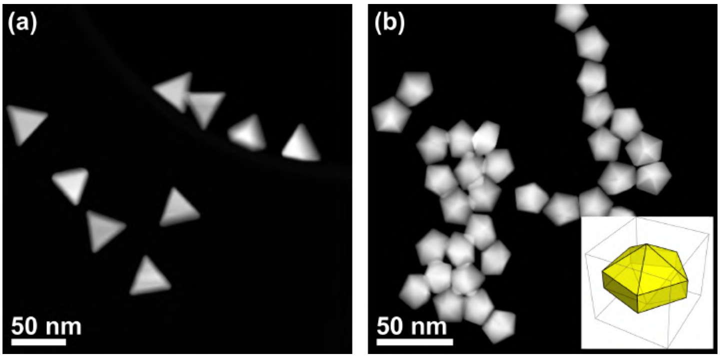

Figure 4.1: Overview HAADF-STEM images of (a) Au triangular platelets and (b) Au Ino decahedra. Inset in panel (b) shows a geometrical model of the Ino decahedron.

SEEBIC experiments were performed using an aberration-corrected "cubed" Thermo Fisher Themis Z TEM operated at an acceleration voltage in a range of 60-200 kV and a beam current of 200-500 pA. A custom-made transimpedance amplifier (see **Chapter 3** for details) with a total gain of 2 GV/A (0.2 GV/A at the first amplification stage) and bandwidth of 8 kHz, electrically connected to the sample via a DENSsolutions Wildfire holder, was used to convert the SEEBIC signal into a voltage signal digitized by the Attollight OUDS II scan engine along with the amplified HAADF-STEM detector signal. No image filtering was applied during post-processing. A FR4 printed circuit board, designed to fit in a DENSsolutions Wildfire heating holder (as shown in **Chapter 3**) was used as a carrier for a conventional copper TEM grid.

It is known that low-energy SEs can be absorbed by carbon layers of just a few nm in thickness [89]. Therefore, after drop-casting onto a copper TEM grid, the samples were Ar/O_2 plasma (3:1) cleaned to avoid a build-up of a layer of carbon contamination during the acquisition of SEEBIC data, as well as to remove surface ligands hindering topography imaging. Carbon contamination is a detrimental side effect in almost all electron microscopy studies. Contamination results from electron beam-induced polymerization of carbon-rich organic molecules on the sample surface that are present from sample preparation and storage or adsorption of molecules from the residual gas atmosphere in the microscope. The plasma consists of a mixture of energetic electrons and ions that bombard the surface and break the C–H bonds. With short-duration exposure, the surface of the specimen itself is essentially unaffected whereas the hydrocarbons are gradually decomposed into smaller organic molecules and pumped away in the vacuum of the plasma cleaner [90].

4.3 Results and Discussion

Conventional transmission electron micrographs, such as the HAADF-STEM images in **Figure 4.2 a, d**, often fail to uniquely describe the shape and faceting of the NPs. ET allows us to extract the necessary topographical information and clearly revealed the presence of side facets in triangular and decahedral NPs (**Figure 4.2 b, e**), which is less obvious from the HAADF-STEM projections. However, the acquisition of the tilt series for ET took approximately 1 hour, which would hamper a high-throughput analysis.

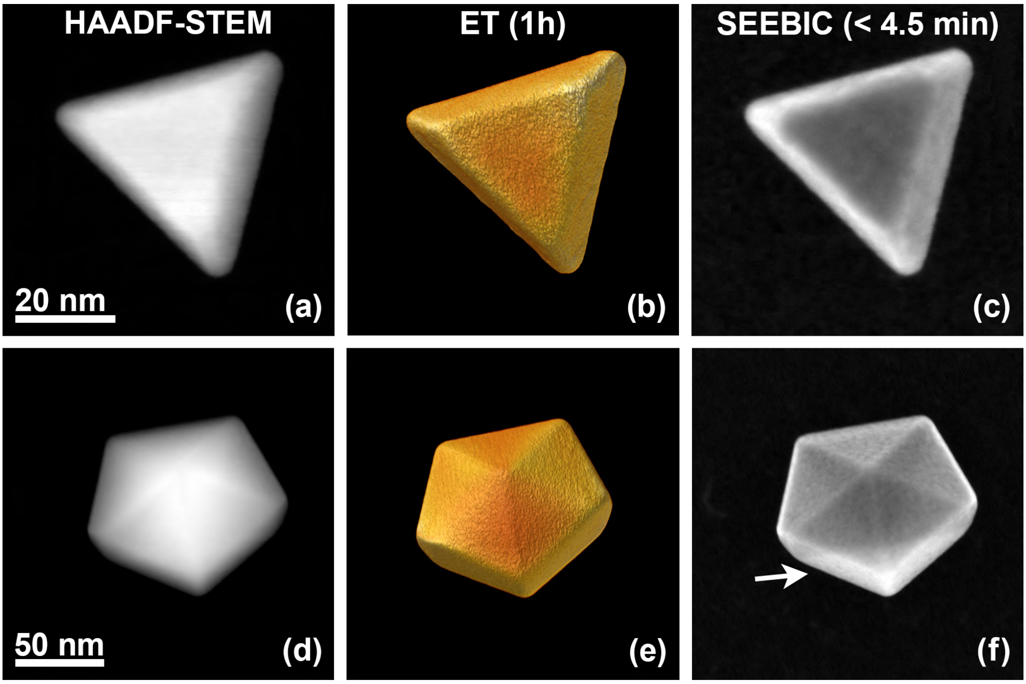

Figure 4.2: STEM images of an Au triangular platelet (a-c) and an Ino decahedron (d-e) obtained in different modes: (a, d) HAADF-STEM, (b, e) 3D surface visualization of an ET reconstruction, (c, f) SEEBIC imaging.

Next, SEEBIC was used to image the same particles (**Figure 4.2 c, f**). It is clear that both the morphology and the presence of side facets can be appreciated from the images. For the triangular platelet, a close-to-perfect agreement is found between the ET reconstruction and the SEEBIC image. However, for the Ino decahedron, subtle differences are present. For example, as indicated by a white arrow, a sharp line adjacent to an area with enhanced SEEBIC contrast is observed. To understand the origin of this contrast, we inspected the entire 3D structure as obtained by ET (see **Figure 4.3**). A thorough inspection does not reveal the presence of the artifactual line on the surface. The orthoslices taken from the reconstruction show the 5-fold symmetry diffraction contrast of twin boundaries that do not coincide with the expected line. Therefore, it is clear that the artifactual feature seen in **Figure 4.2 f** is not related to any specific structural or compositional features in the NP.

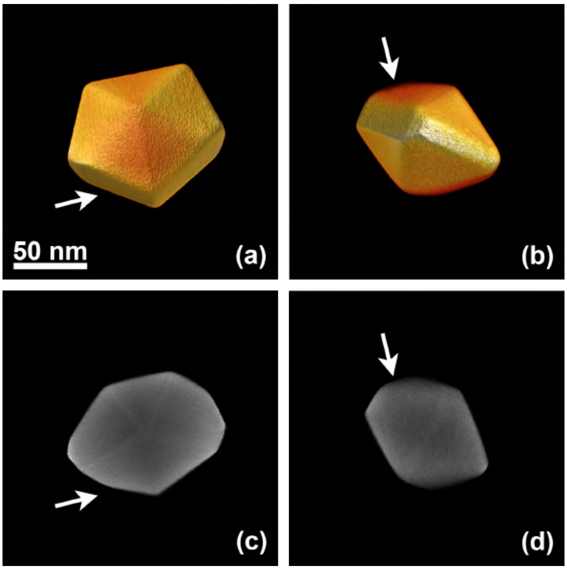

Figure 4.3: 3D surface renders of the Au Ino decahedron from **Figure 4.2** of the main text obtained from an ET reconstruction: (a) top view, (b) side view. (c) XZ- and (d) XY- orthoslices taken from the centre of NP. The white arrows indicate the area of the ET reconstruction for which the SEEBIC image showed an artificial line. The lines that are visible in the orthoslices are typical for this type of NPs with fivefold symmetry and correspond to grain boundaries [91].

It should be noted that similar to SEM images, SEEBIC provide only a pseudo-3D perception of the object under investigation, the information about real 3D structure (or morphology) remains hidden and cannot be extracted directly for further quantification and analysis. However, qualitative conclusions about the 3D structure of the NPs still can be made based on these images. To extract quantitative information about the surface morphology, state-of-the-art computer vision techniques can be employed similar to SEM [92].

4.3.1 Accumulated Electron Dose Estimation

To evaluate electron dose efficiency of SEEBIC we estimated accumulated electron dose during both ET and SEEBIC experiments presented in **Figure 4.2** using **Equation 4.1** with experimental parameters shown in **Table 4.1** similar to Vanrompay *et al.* [44]. Tracking and refocusing of a NP for the ET experiment was taken into account since these operations require additional illumination of the sample and therefore contribute to the total electron dose in conventional ET experiment. We used imaging at lower magnification to accurately track the NP of interest and lower dwell time to decrease the electron dose and accelerate the experimental runtime. For the electron dose calculations, we, therefore, assumed an 8 times larger pixel size for the tracking and half of the dwell time. The focusing step was done by acquiring a through-focus series of approximately 5 images at lower magnification and reduced dwell time.

$$Dose = \frac{beam\ current \times dwell\ time}{electron\ charge \times (pixel\ size)^2} \times number\ of\ images \tag{4.1}$$

	Electron tomography	**SEEBIC**
Acquisition	Beam current: 50 pA Dwell time: 3 μs Pixel size: 184 pm Tilt range: ±75° Tilt increment: 3° Number of images: 51	Beam current: 500 pA Dwell time: 1 ms Pixel size: 368 pm Tilt range: - Tilt increment: - Number of images: 1
Tracking	Beam current: 50 pA Dwell time: 1.5 μs Pixel size: 1472 pm Tilt range: ±75° Tilt increment: 3° Number of images: 255	Negligible compared to the acquisition
Focusing	Beam current: 50 pA Dwell time: 1.5 μs Pixel size: 368 pm Tilt range: ±75° Tilt increment: 3° Number of images: 255	Negligible compared to the acquisition
Total dose	$2.35 \times 10^4\ e/\AA^2$	$2.30 \times 10^5\ e/\AA^2$

Table 4.1: Acquisition parameters used for estimation of dose.

We have shown that using our current setup, SEEBIC is one order of magnitude less dose-efficient compared to conventional ET. On the other hand, the acquisition time for a single 512 × 512 SEEBIC image in **Figure 4.2 c and f** was 4.5 min (dwell time of 1 ms), which means a drastic reduction in the acquisition time (up to 13 times in this case). Further optimization of the experimental parameters (high voltage and dwell time) demonstrates that both dose and acquisition time can be significantly reduced while preserving the signal-to-noise ratio at a level that still enables a clear interpretation of the particle morphology. **Figure 4.4** shows that acquisition times of approximately half a minute per image are feasible. Overall, this results in a time reduction of two orders of magnitude in comparison to the acquisition for ET. The electron dose can also be further reduced, rendering SEEBIC equally or even more dose-efficient as ET. Consequently, SEEBIC will enable to improve the throughput of 3D characterization as well as to investigate nanoparticle transformations during the *in situ* application of specific triggers such as e.g. heat.

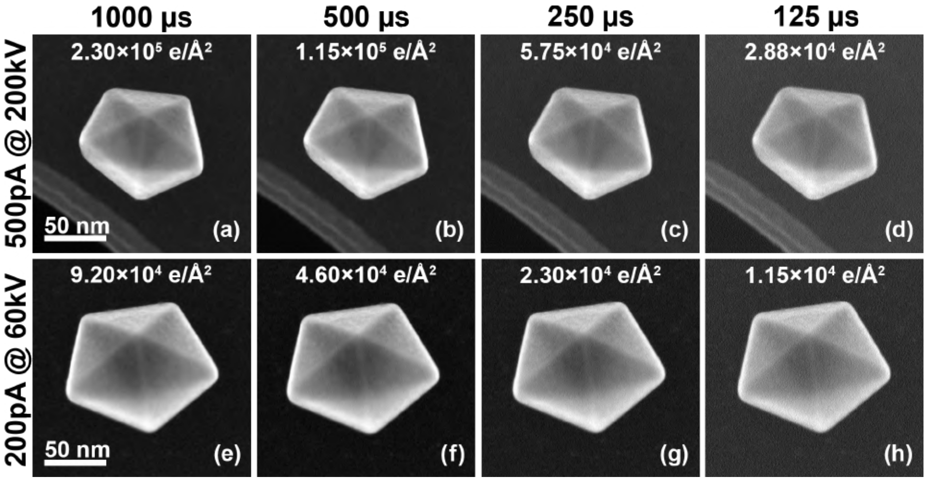

Figure 4.4: SEEBIC images of Au Ino decahedra obtained at various experimental conditions and dwell times. The accumulated dose is indicated in each panel.

4.3.2 Comparison with SEM

Next, we compare SEEBIC imaging with conventional SEM images **Figure 4.5**. Because of (unavoidable) different experimental conditions, a direct comparison is not straightforward. Nevertheless, it is clear that the SEEBIC yields superior image quality. To estimate the image resolution obtained by SEM and SEEBIC, we used the edge spread function (ESF), based on intensity profiles acquired across the edges of the nanoparticles, as indicated by white arrows in **Figure 4.6**. The ESF is a result of a convolution of a sharp edge of the NPs with a point spread function (PSF) that is directly connected to spatial resolution. If we assume a PSF that is described by the logistic distribution curve, we obtain a sigmoid function for the ESF [93].

$$ESF(x) = \frac{a}{1 + exp(\frac{r-x}{\sigma})} + b \tag{4.2}$$

In this expression, a and b correspond to scaling factors and r is the position of the edge. The parameter σ is related to the full width at half maximum $FWHM = 2ln(3 + \sqrt{8})\sigma = 3.53\sigma$ [94], which we here consider as an estimate for the spatial resolution. In this manner, we estimate the spatial resolution of the SEM images as approx. 4.2 nm, while the nominal resolution of the instrument was listed as 0.8 nm.

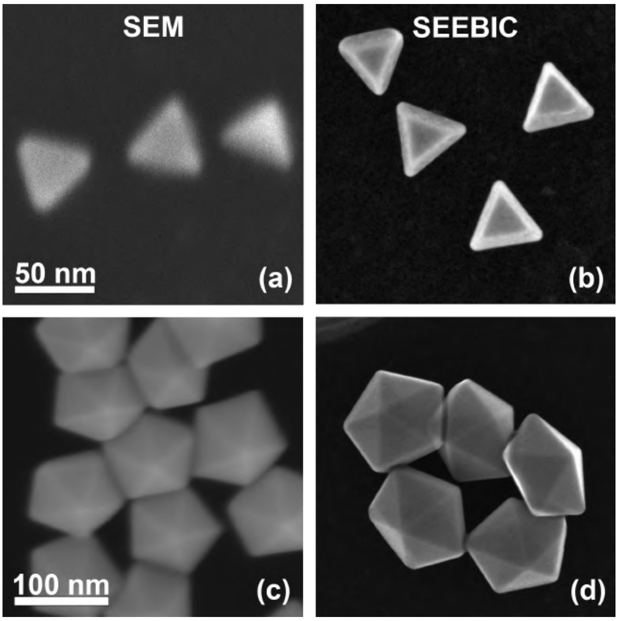

Figure 4.5: Conventional SEM (a, c) and SEEBIC images (b, d) of Au triangles (a, b) and Au Ino decahedra (c, d).

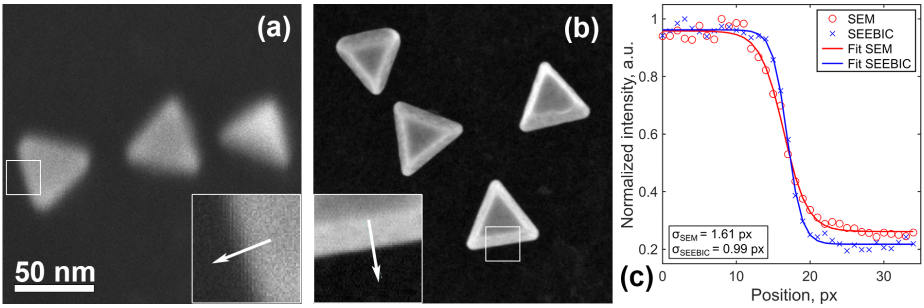

Figure 4.6: (a) conventional SEM and (b) SEEBIC images with an indication of line profiles taken for analysis, (c) ESFs obtained from the images (a) and (b) with sigmoid curve fit.

The discrepancy between nominal (0.8 nm) and actual (4.2 nm) SEM resolution can be explained by the fact that nominal resolution is usually defined as a probe size while in real experiments resolution is defined by the electron-matter interaction volume. A delocalization of the SE signal due to the scattering of the primary electron beam inside the sample and the process by which the SEs can leave the sample only up to a limited depth leading to an effective interaction volume that is significantly larger than the probe size, especially at low beam energies such as used here [23]. The SEEBIC images yield a clearly higher spatial resolution, estimated to be 1.3 nm. The SEEBIC resolution is limited by the selected sampling, which was balanced between a sufficient field of view and the total acquisition time. It should be noted, however, that the theoretical resolution is governed by the obtainable probe size and atomic resolution imaging using SEEBIC is also possible (**Figure 4.7**). The improvement of spatial resolution using SEEBIC in comparison to SEM is especially important when imaging NPs with sizes smaller than 50 nm (**Figure 4.5 a, b**).

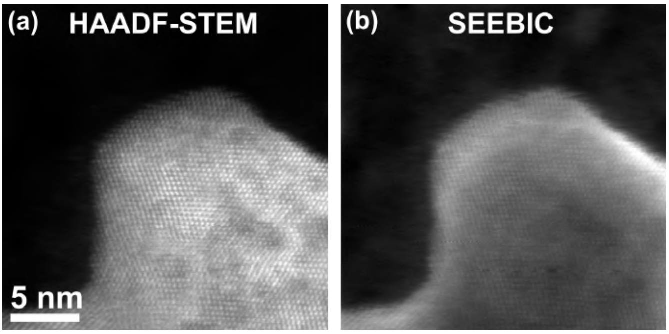

Figure 4.7: Atomic resolution images of $NaYF_4$ NPs doped with Yb and Er: (a) HAADF-STEM and (b) SEEBIC.

We used a similar approach to estimate the spatial resolution of obtained ET data [93]. Note that the resolution of ET data has an anisotropic nature due to the geometry of the experiment. The obtained resolution values are 0.77 nm for the x-axis, 0.76 nm for the y-axis, and 0.98 nm for the z-axis (**Figure 4.8**).

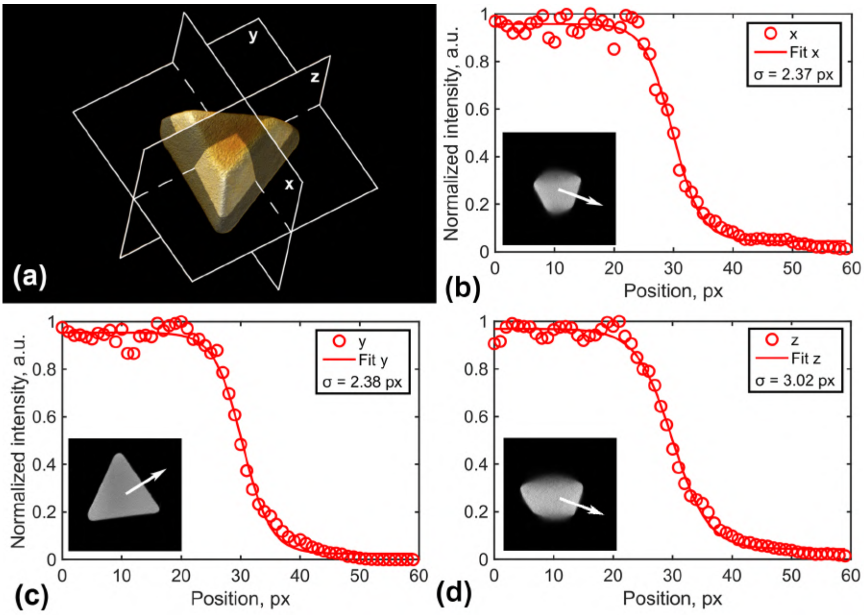

Figure 4.8: (a) Side view 3D render of ET obtained from Au triangular platelet with indicated orthoslices. ESFs obtained from the ET data of a nanotriangle along: (b) x-axis (c) y-axis, (d) z-axis with sigmoid curve fit. Insets show orthoslices with the indication of line profiles taken for analysis.

4.3.3 Origin of Artifactual SEEBIC Contrast

As demonstrated above, SEEBIC images show a close resemblance to SEM images, which is not surprising given that they are both formed through the creation of SEs. However, the white arrow in **Figure 4.2 f** illustrates the presence of artifactual features that cannot be understood in terms of surface contrast. For SEEBIC to become a useful alternative for ET, it is important to understand the origin of these artifacts.

In a SEM experiment, the acceleration voltage is lower in comparison to typical (S)TEM, and consequently, SEs are predominantly generated at the top surface of the nanoparticles. In the case of (S)TEM, however, the incident electron beam traverses the sample, and SEs are emitted from both the top and bottom surfaces. Because of the strong magnetic field ($\propto 2T$) in the pole-piece gap of the TEM, the SEs that leave the nanoparticle during a SEEBIC experiment will either spiral up or down (as shown in **Figure 2.5**). For the electrons spiraling up, the generated SEs leave the nanoparticles in a charged state and to reestablish the charge balance, the holes corresponding to emitted SEs flow to the transimpedance amplifier, which will generate the topographical contrast observed in SEEBIC images. On the other hand, the electrons that spiral down might be re-absorbed by structural features along their trajectories. Due to their extremely short inelastic mean free path (approx. 1-3 nm for C) [89, 95], these low-energy SEs are readily absorbed by the TEM support, corresponding to, e.g., a few nm-thick amorphous carbon layer. In this manner, the EBIC current that would otherwise flow to the amplifier is compensated, resulting in a contrast that is dominated by the top surface of the nanoparticles.

Oppositely, when a nanoparticle is partially suspended over a hole in the support film, which is the case for the particle in **Figure 4.9 a-c**, a significant portion of SEs generated at the bottom surface can escape without being absorbed and consequently contribute to the SEEBIC image formation. As a result, an image is formed that contains contributions of both the front and back surfaces, as indicated by the white arrows in **Figure 4.9 c**. Even if the particle is lying on a closed membrane support (continuous conductive film), non-topographical contrast might be present, which is exemplified by the sharp line in **Figure 4.2 f** and **Figure 4.9 f**. In this case, the Au Ino decahedron lies on one of its facets, resulting in a gap between the other NP facets and the support film, as schematically illustrated in **Figure 4.2 d** and **Figure 4.10**. Consequently, a fraction of the SEs emitted from the bottom facets escapes without being re-captured by the support film (**Figure 4.9 d**, red arrows). This fraction is determined by the angle-dependent scattering cross-section for SEs and the orientation of the NP's surface normal relative to the magnetic field axis. The apparent line in SEEBIC consequently corresponds to the edges of the Ino decahedron that form the boundary between the "base" of a NP and its suspended part, leading to abrupt changes in contrast. It should be noted that this line is also present in HAADF-STEM because of local changes in sample thickness due to the presence of the edges of Ino decahedron **Figure 4.10**.

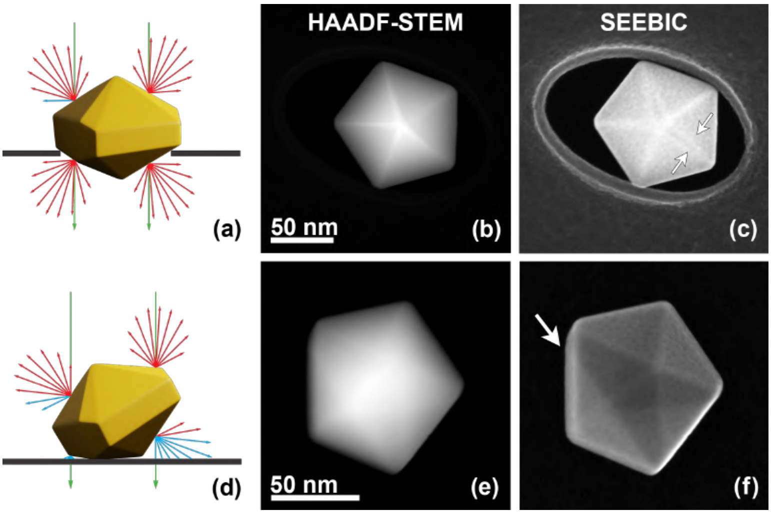

Figure 4.9: (a, d) 3D visualization of the NPs on the support film. (b, e) HAADF-STEM and (c, f) SEEBIC images of Au decahedra. Red arrows indicate SEs escaping the surface of NPs without being absorbed by the support, and blue arrows indicate re-captured SEs. The lengths of the arrows on panels (a) and (d) are indicative of the number of SEs emitted in each direction and proportional to the cosine of the angle between this direction and the surface normal. Green arrows indicate the primary electron beam.

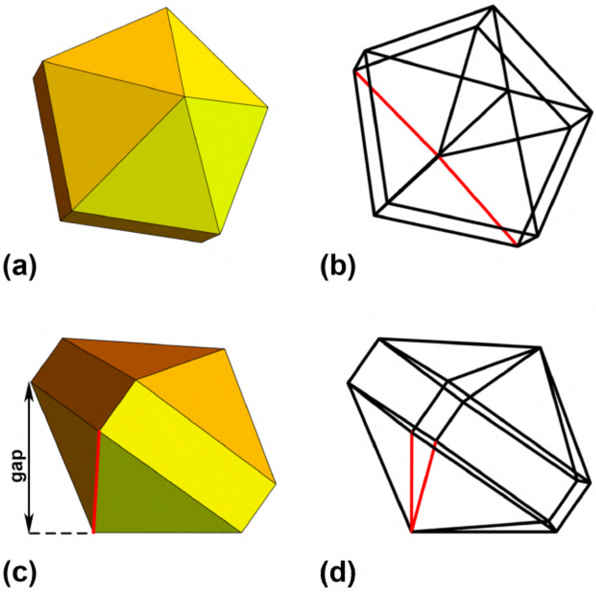

Figure 4.10: 3D surface renders of the simulated model of Au Ino decahedron from **Figure 4.9 d**: (a) - (b) top view, (c) - (d) side view, (b), (d) wireframe 3D representation of the model. Edges forming a straight line are indicated in red.

Figure 4.11 shows that both the intensity and the position of the artifactual line are dependent on a sample tilt angle, thereby confirming our model of contrast formation.

Intensity variations can be explained by the changes in the angle between the surface normal and the magnetic field axis leading to changes in the number of SEs that can escape without being re-absorbed by the support film (**Figure 4.11** bottom row). The shift of the artifactual line is apparent from **Figure 4.11** (see wireframe models) and can be explained by the shift of the boundary between the "base" of a NP and its suspended part relative to the “zero-tilt position”.

To demonstrate that SEEBIC image artifcat appearance is independent of acceleration voltage, a similar tilt series was acquired at 60 kV. The data obtained at 60 kV did not reveal any significant acceleration of the effect. Even though the lower accelerating energy leads to an overall increase in SE yield, the fraction of SEs that can escape from the gap formed by a NP and the support film is determined by the angle between the surface normal and the magnetic field axis only, but independent of the electron beam energy.

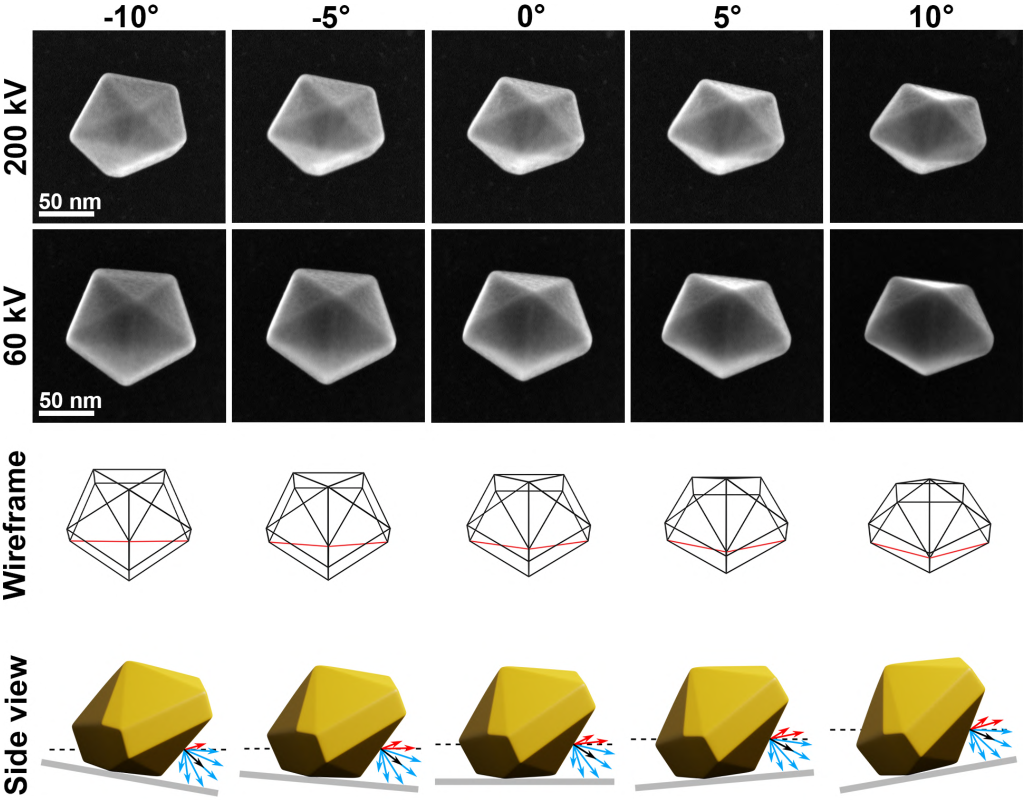

Figure 4.11: SEEBIC tilt series of Au Ino decahedra, obtained at acceleration voltages of 200 kV and 60 kV, and corresponding 3D wireframe representation of the model and side views. Red arrows indicate SEs escaping the surface of the NPs without being absorbed by the support, blue arrows indicate re-captured SEs. The lengths of the arrows on panels in the bottom row are indicative of the number of SEs emitted in each direction and proportional to the cosine of the angle between this direction and the surface normal.

The described model of contrast formation can be used for understanding artifactual features arising in **Figure 4.5 d**. **Figure 4.12** shows a 3D schematic illustration, based on the SEEBIC image. The "transparency" of crystal A over B can be clearly seen, whereas this effect is less prominent in the case of crystals B, C, and D. This can be explained by a different arrangement of the particles relative to each other. In the first case, both particles A and B lie on the support film with one of their facets forming a gap between the top facets of particle B and the bottom facets of particle A (**Figure 4.12 c**). Secondary electrons emitted by the bottom facets of NPs A and B can escape without being re-absorbed and thus contribute to the SEEBIC signal.

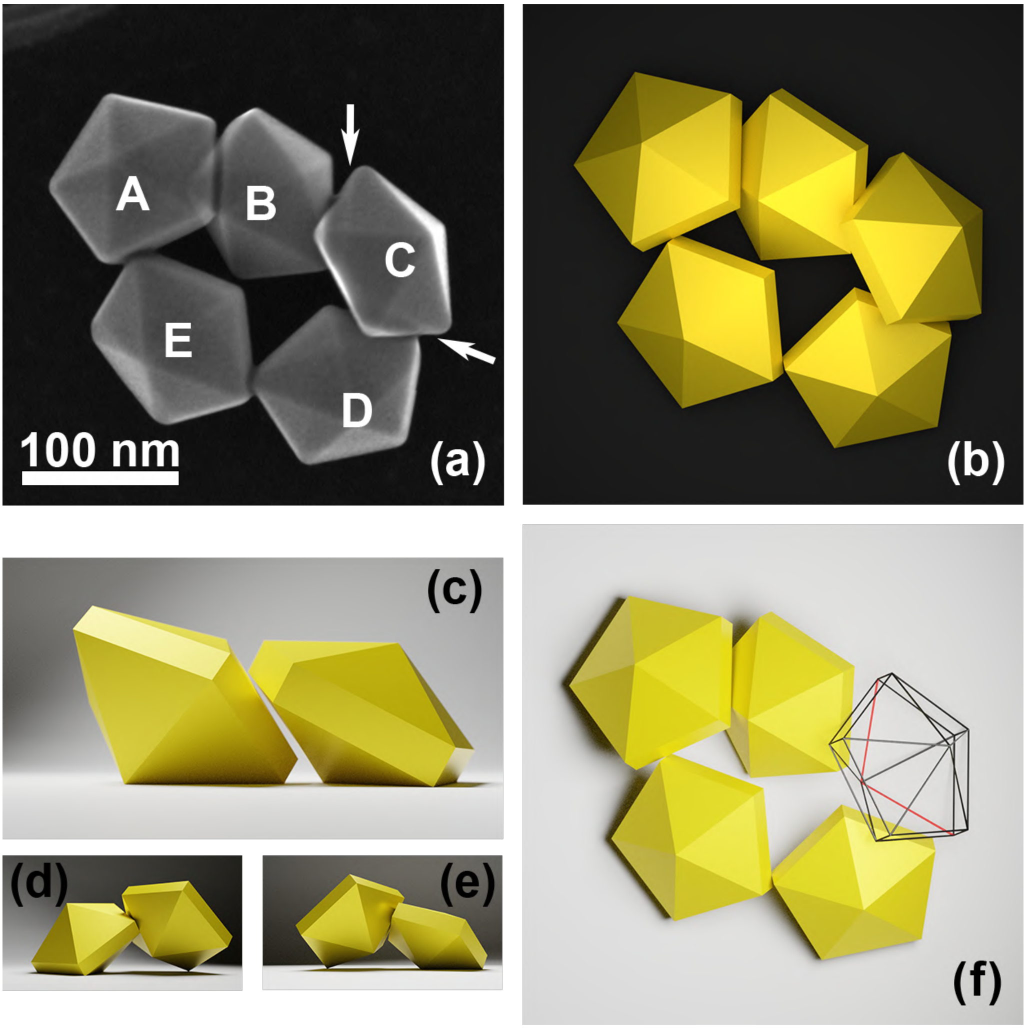

Figure 4.12: (a) SEEBIC images Au Ino decahedra with artifactual features. (b)-(f) 3D recreation of the arrangement of the NPs shown in panel (a): (b) top view, (c) side view on NPs A and B, (d) side view on NPs B and C, (e) side view on NPs D and C, (f) wireframe render of NP C.

In the other case, particle C is supported by three points formed by: (1) one of its vertices and the support film, (2) one of its bottom edges and the top surface of particle B, (3) its bottom facets and the top surface of particle D, as shown in **Figure 4.12 c-e**. Therefore, only the "tips" of particle C are sticking out, forming the gaps with particles B and D that lead to a bright contrast. Line contrast indicated by white arrows in **Figure 4.12 a** can be explained as the boundary between the "base" of a NP and its "suspended part", as can be seen from the wireframe model (**Figure 4.12 f**).

4.3.4 Imaging of Dielectric and Semiconductor Materials

In addition, it should be noted that 3D characterization by SEEBIC is not limited to metallic particles only, the main requirement for a SEEBIC experiment is the presence of a conductive underlying substrate from the sample to the amplifier. Here, the NPs were deposited on a conductive C film to fulfil this requirement. This requirement does not restrict the types of samples that can be studied. SEEBIC can also be performed on dielectric and semiconductor materials (**Figure 4.13**), as long as charge transport can occur, e.g., through leakage current or other transport mechanisms such as Poole-Frenkel conduction, hopping conduction, and tunneling [64]. Moreover, in cases where both standard EBIC and SEEBIC are present, a two-channel EBIC setup can be used to separate two signals [96].

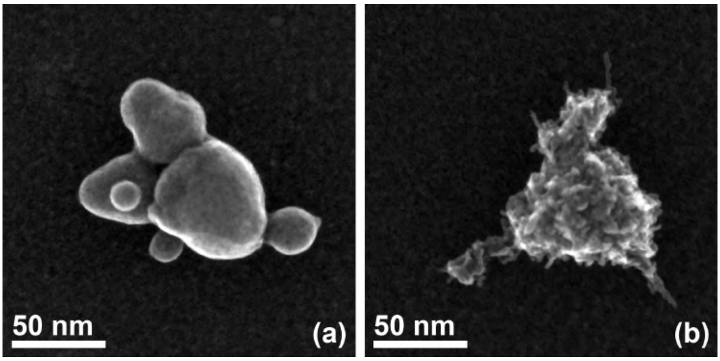

Figure 4.13: SEEBIC images of (a) SiO_2 and TiO_2 nanopowders demonstrating the capability of the technique to image dielectric and semiconductor materials.

4.4 Conclusions

We have demonstrated that SEEBIC can be considered as an attractive approach to image the morphology of nanomaterials with shorter acquisition and processing times of up to two orders of magnitude in comparison to ET and superior resolution in comparison to SEM. The contrast artifacts arising in SEEBIC were considered, and their origin was explained. We demonstrated the importance of using closed membrane support to minimize these imaging artifacts. Direct access to surface morphology obtainable in the order of minutes opens up the possibility of using SEEBIC for high-throughput analysis and combining 3D imaging with *in situ* stimuli.

Chapter 5

Physical Model of SEEBIC Topographical Contrast Formation

In the previous chapter, it can be seen that despite the apparent simplicity of the underlying physics behind SEEBIC, the interpretation of the images is not always straightforward. The interaction of emitted SEs with a strong magnetic field of the objective lens complicates the contrast of SEEBIC images, and for the technique to become a widely applicable tool for 3D imaging of the structure of nanoparticles, a thorough understanding of the mechanisms of SEEBIC contrast formation is required. In this chapter, I attempt to quantify the interaction of emitted SEs with the magnetic field of the objective lens by developing a physical model that includes the angle-dependent escape rate of SEs and their contribution to the SEEBIC signal.

5.1 Introduction

In this introductory section, I will discuss the peculiarities of the secondary electron image simulations. SE simulations are well-established for SEM for understanding the contrast formation mechanism in such systems. Especially in the field of the semiconductor industry, where an accurate image model is used to precisely measure dimensional parameters in e.g. photoresist or etched layout structures. The simulation of SEM images is usually employed by a Monte Carlo method to model the trajectory of electrons as they interact with a specimen [97].

In Monte Carlo simulations, electrons are treated as classical point particles. They travel through a material, encountering discrete scattering events along their path. Between

---

This chapter is based on the following paper:

Vlasov E., Heyvaert W., Stoops T., Kadu A., Van Aert S., Verbeeck J., Bals S. Physical model of SEEBIC topographical contrast formation (in preparation).

The contribution of the author of the thesis consisted of conceptualization and implementation of the physical model as well as experimental data acquisition, processing and analysis. Matlab code for SEEBIC image simulation was written in collaboration with W. Heyvaert and Dr. A. Kadu.

these events, electrons are regarded as free. There is a clear distinction between the events that may occur to the electrons: inelastic scattering, elastic scattering and material boundary crossing. The first two take place in the bulk of the material, whereas the latter represents interactions at the interface of the material. Monte Carlo simulations rely on pre-defined models for electron-matter interactions that are well-described in literature (e.g. mean-free path, scattering cross-section, etc.) [97]. At the start of every iteration, a single electron has a known position, direction and energy. If the electron is in a vacuum, it moves along a straight line (assuming there is no magnetic field) without undergoing scattering until it reaches the intersection with a material boundary. In the material, an electron randomly encounters elastic and inelastic scatterings probed for random free path lengths. The exact distance of travel to the next event is a random number, typically given by the exponential Lambert-Beer law, with the mean free path depending on the electron's energy and the type of excitation. The electron travels straight to the nearest event, which is then executed. The outcomes of the scattering events include potential reflection, refraction, or energy change at material boundaries, or deflection and energy loss within the material. Inelastic events may generate SEs, which are then treated like new primary electrons with a given energy. This process continues until an electron either reaches a detector (if included in the simulation) or loses enough energy to stop interacting with the material.

Monte Carlo simulation programs can include different stages of the SEM image formation process: the probe forming, the probe-sample interaction and the detection process. Additionally, Monte Carlo simulators can be coupled with an electromagnetic field solver to simulate specimen charging [98]. It should be noted that the Monte Carlo simulation of SE images is well-established for SEM, whereas, to our knowledge, there are no publications describing SE image simulation in STEM using the Monte Carlo method. Even though Demers and co-authors [99] attempted to expand their Monte Carlo model to STEM imaging conditions, their study is focused on ADF image simulation rather than topographical SE images. First attempts for atomic resolution SE imaging [59, 60] stimulated a series of publications on the mechanisms responsible for the atomic resolution of SE images [61, 62], but this topic is out of the scope of the current chapter and will not be discussed here.

As can be seen from the previous chapter, in the case of SEEBIC, the interaction of emitted SEs with a magnetic field of the objective lens may strongly affect the image contrast. Therefore, the Monte Carlo method, in its traditional form cannot be used to simulate SEEBIC images. It needs to be combined with a model describing the motion of SEs in a strong magnetic field. In this chapter, we propose a model that mainly considers the interaction of the emitted SEs with the magnetic field of the objective lens of the STEM omitting electron-matter interaction simulated by Monte Carlo. The main goal of this model is to aid the interpretation of artifacts in SEEBIC images in a relatively fast and simple manner. In future, our model can be coupled with Monte Carlo simulations to accurately simulate SEEBIC images.

5.2 Problem Statement

To better understand the contrast formation in SEEBIC, we consider the following problem: a convex-shaped NP is placed on an absorbing (meaning that the thickness of the support exceeds an inelastic mean free path of the SEs in the material) continuous and conductive support in a homogeneous strong magnetic field of the TEM pole piece gap. The overall SEEBIC intensity measured for each scanning position is determined then by several key factors: (1) the length of the primary beam path within the SE escape depth L, (2) recapture of the emitted SEs by the support, and (3) recapture the emitted SEs by protrusions and the sharp tips present at the surface of a nanoparticle. It should be noted that the evaluation of the influence of the third factor requires a solution of the ray tracing problem. Here, we only consider convex-shaped NPs meaning that all internal angles are less than 180° and there is no recapture of SEs by sharp tips and protrusions present in the NP itself. Therefore, the third factor can be neglected

The low kinetic energy of SEs (< 50 eV) determines the depth from which SEs can escape from the specimen. SEs suffer rapid energy loss with distance travelled, limiting the escape depth of SEs to a few nanometers [23]. Therefore, only SEs generated close to a surface have a significant probability to escape. As the primary beam traverses through the specimen, the SE generation rate is effectively constant along the path that lies within the shallow escape depth of SEs d. The length of the primary beam path within the escape depth L increases as the secant of α **Equation 5.1**, where α is the surface inclination angle relative to the incident electron beam. Assuming that the number of secondary electrons that eventually escape will be proportional to the number generated in this near-surface region, the secondary electron coefficient (number of emitted SEs per incoming primary electron, δ) is similarly expected to rise with the secant of the inclination angle (**Figure 5.1**).

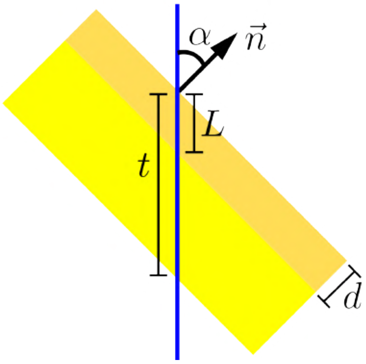

Figure 5.1: Schematic showing the length of the primary beam path within the SE escape depth that defines dependence of SE yield on inclination angle relative to the incident beam.

$$L = d\,|\sec(\alpha)| \tag{5.1}$$

Hereby, it should be noted that **Equation 5.1** equals infinity at $\alpha = \frac{\pi}{2}$ making this expression unphysical. However, the length of the primary beam path within the SE escape depth cannot be longer than the sample thickness when the beam is incident perpendicular to the surface normal. Therefore, the problem can be resolved by taking the local thickness of the specimen (thickness of the sample in incidence point of the primary beam) t into account. Namely, L can never be larger than t, such that we find that for each scanning position, the SE intensity is defined as:

$$I_{1,i} \propto \min\left(t/d, |\sec(\alpha)|\right), \tag{5.2}$$

SE emitted from the NP surface into the vacuum in an arbitrary direction (e.g. $\vec{n}_i$) determined by its velocity vector $\vec{v}_i$ will be affected by the presence of a magnetic field of the objective lens $\vec{B}$ (**Figure 5.2**). This magnetic field in the pole piece gap of the objective lens is assumed to be homogeneous (magnetic lines are parallel to each other) since the sample is small compared to the pole piece gap volume. The velocity of the SE, which is oblique to the magnetic field, can be decomposed into parallel and perpendicular components to the magnetic field $\vec{v}_{\|}$ and $\vec{v}_{\perp}$ respectively. $\vec{v}_{\|}$ defines the motion of SEs along the magnetic field axis in the direction defined by $\vec{v}_{\|}$. At the same time, the $\vec{v}_{\perp}$ vector results in a circular motion of the SEs induced by the Lorentz force. Therefore, electrons are spiralling up or down in the magnetic field of the pole-piece of a TEM. SEs with $\vec{v}_{\|}$ antiparallel to $\vec{B}$ are spiralling downwards and, if the absorbing support is present, they will be recaptured by the support film, and thus they do not contribute to the overall SEEBIC signal. The fraction of the emitted SEs can be estimated from their angular distribution. From the literature, it is known that SE trajectories can be described by Lambert's cosine law [23], meaning that the number of SE emitted by the surface along a certain direction is proportional to the cosine of the angle between this direction and the surface normal (**Figure 5.2 b**).

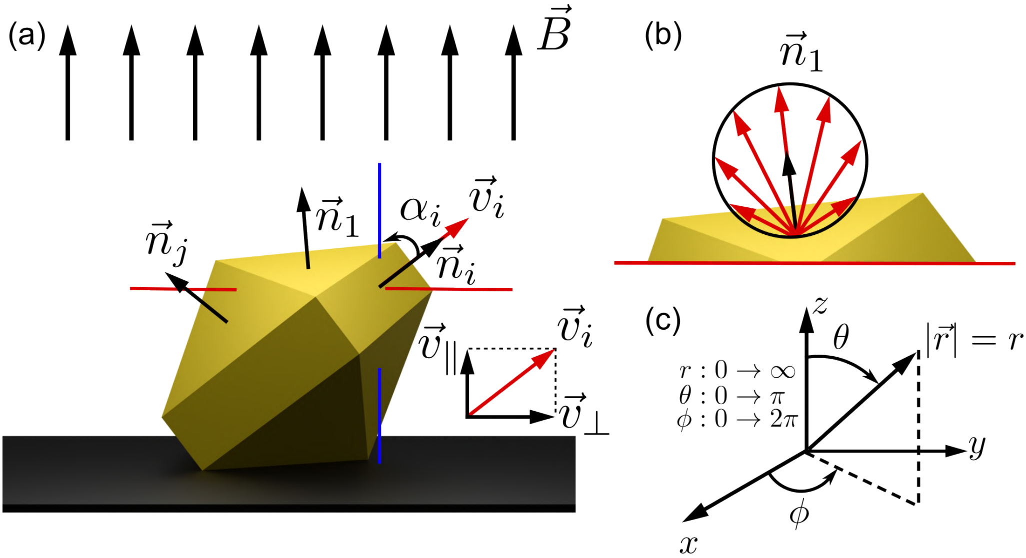

Figure 5.2: (a) Schematic representation of the imposed problem. (b) Emission of SEs according to Lambert's law. The lengths of the red arrows in panel (b) are proportional to the number of SEs emitted in their direction, black arrow indicates the surface normal $\vec{n}_1$. (c) The spherical coordinate system used in the problem solution.

The number of SEs that can escape without being re-captured by the support film and NP surface or, in other words, the intensity of detected SEEBIC signal for every scanning position can therefore be evaluated by simply integrating the angular distribution of the emitted SEs taking into account boundary conditions defined by the relative orientation of the surface and the support to magnetic field axis (primary electron beam direction). Considering the symmetry of the problem, the integration can be done in spherical coordinates (**Equation 5.3**) associated with the surface normal for every scanning position (**Figure 5.2 c**).

$$\begin{cases} x = r\sin(\theta)\cos(\phi) \\ y = r\sin(\theta)\sin(\phi) \\ z = r\cos(\theta) \end{cases} \tag{5.3}$$

The chance that an SE escapes in a direction $\vec{v}$ that makes an angle θ with the surface normal $\vec{n}$ is given by the cosine rule. We will therefore integrate $\cos(\theta)$ over the part of the unit sphere where SEs can escape without hitting the substrate or the surface of the NP as shown in **Equation 5.4**.

$$I_{2,i} = \int_0^{\phi(\alpha_i)} d\phi \int_0^{\theta_m(\phi(\alpha_i))} d\theta \sin(\theta)\cos(\theta), \tag{5.4}$$

where α_i is the angle between the i_{th} surface normal of the NP and primary electron beam. The limits of the integration are set according to boundary conditions defined by the absorption of SEs by the support film – all the SEs with $\vec{v}_{\parallel}$ antiparallel to $\vec{B}$ should be excluded from consideration. The dependence of the upper integration limits on α_i in **Equation 5.4** can be found from the geometry of the problem.

To find the region on the unit sphere that needs to be integrated, we need to consider two cases shown in **Figure 5.3**.

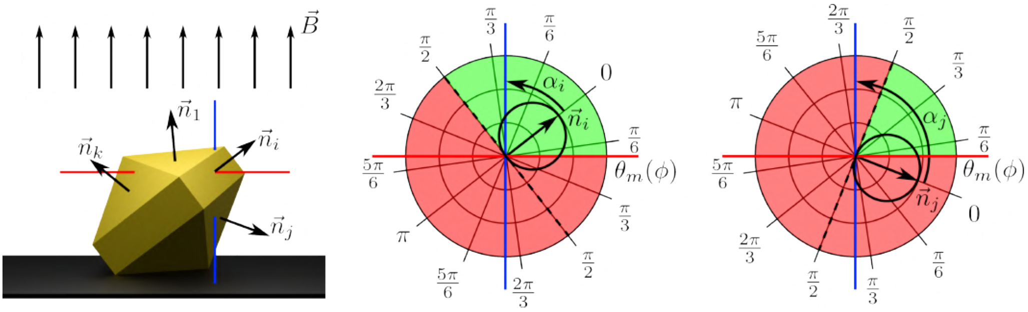

Figure 5.3: (a) Schematic representation of the imposed problem with indicated surface normals. (b)-(c) Auxiliary geometrical plots showing unit sphere section at $\phi = 0$ with integration limits at different values of α: (b) $\alpha \in \left[0, \frac{\pi}{2}\right]$, (c) $\alpha \in \left[\frac{\pi}{2}, \pi\right]$. The blue line shows the magnetic axis, and the red line is a plane perpendicular to the magnetic axis. Black circle around surface normals $\vec{n}_i$ and $\vec{n}_j$ represents Lambert's cosine law.

If $\alpha_i \in \left[0, \frac{\pi}{2}\right]$, we find

$$I_2 = \frac{1}{N} \cdot \left(\int_0^{\pi} d\phi \int_0^{\frac{\pi}{2}} d\theta \cos(\theta) \sin(\theta) + \int_{\pi}^{2\pi} d\phi \int_0^{\theta_m(\phi(\alpha_i))} d\theta \cos(\theta) \sin(\theta) \right) \tag{5.5}$$

and if $\alpha_i \in \left[\frac{\pi}{2}, \pi\right]$, we find

$$\begin{aligned} I_2 &= \frac{1}{N} \cdot \int_0^{\pi} d\phi \int_{\theta_m(\phi(\alpha_i))}^{\frac{\pi}{2}} d\theta \cos(\theta) \sin(\theta) = \\ &= \frac{1}{N} \cdot \left(\int_0^{\pi} d\phi \int_0^{\frac{\pi}{2}} d\theta \cos(\theta) \sin(\theta) - \int_0^{\pi} d\phi \int_0^{\theta_m(\phi(\alpha_i))} d\theta \cos(\theta) \sin(\theta) \right) \end{aligned} \tag{5.6}$$

with

$$N = \int_0^{2\pi} d\phi \int_0^{\frac{\pi}{2}} d\theta \cos(\theta) \sin(\theta) = \pi \tag{5.7}$$

The first integral in both equations is constant:

$$\int_0^{\pi} d\phi \int_0^{\frac{\pi}{2}} d\theta \cos(\theta) \sin(\theta) = \frac{\pi}{2} \tag{5.8}$$

Such that we have

$$I_2 = \begin{cases} \frac{1}{2} + \frac{1}{\pi} \int_{\pi}^{2\pi} d\phi \int_0^{\theta_m(\phi(\alpha_i))} d\theta \cos(\theta) \sin(\theta), \alpha_i \in \left[0, \frac{\pi}{2}\right] \\ \frac{1}{2} - \frac{1}{\pi} \int_0^{\pi} d\phi \int_0^{\theta_m(\phi(\alpha_i))} d\theta \cos(\theta) \sin(\theta), \alpha_i \in \left[\frac{\pi}{2}, \pi\right] \end{cases} \tag{5.9}$$

To find $\theta_m(\phi(\alpha_i))$, one needs to realize that it is given by the intersection of an inclined plane with the unit sphere as shown in **Figure 5.4**. The equation in Cartesian coordinates that describes the inclined plane is (i indices are further emitted for simplicity)

$$z = -y \tan(\alpha) \tag{5.10}$$

In spherical coordinates, we find

$$r \cos(\theta_m) = -r \sin(\theta_m) \sin(\phi) \tan(\alpha) \Rightarrow \theta_m(\phi(\alpha)) = -\arctan(\cot(\alpha) \csc(\phi)) \tag{5.11}$$

Therefore,

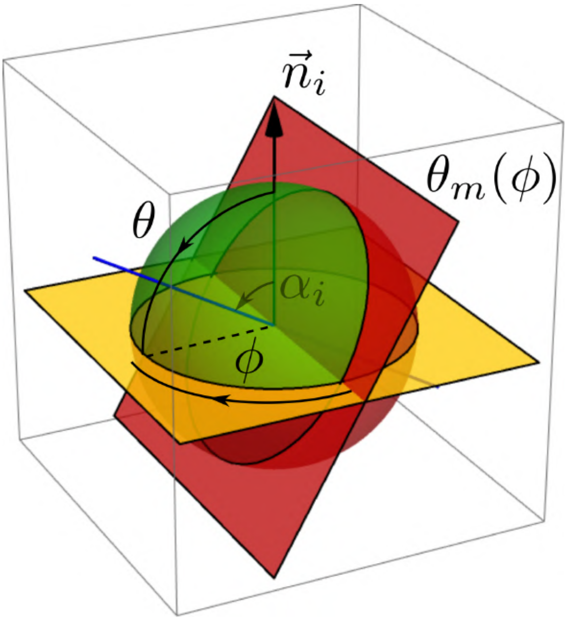

Figure 5.4: Auxiliary geometrical plots showing the intersection of an inclined plane with the unit sphere.

$$I_2 = \begin{cases} \frac{1}{2} + \frac{1}{\pi} \int_{\pi}^{2\pi} d\phi \int_0^{-\arctan(\cot(\alpha)\csc(\phi))} d\theta \cos(\theta)\sin(\theta), \alpha \in \left[0, \frac{\pi}{2}\right] \\ \frac{1}{2} - \frac{1}{\pi} \int_{0}^{\pi} d\phi \int_0^{-\arctan(\cot(\alpha)\csc(\phi))} d\theta \cos(\theta)\sin(\theta), \alpha \in \left[\frac{\pi}{2}, \pi\right] \end{cases} \tag{5.12}$$

The solution of the integral results in cosine-like law (see **Section 5.6** for the solution of the integral):

$$I_2 = \frac{1 + \cos(\alpha)}{2}, \alpha \in [0, \pi] \tag{5.13}$$

In general, we find that the intensity of a SEEBIC image is a function of the inclination angle α of the surface normal and the local thickness t of the specimen at the scan location as a product of two contributors to overall SEEBIC intensity $I_{1,i}$ and $I_{2,i}$ (**Figure 5.5**):

$$I_i(\alpha_i, t_i) \propto \frac{1 + \cos(\alpha_i)}{2} \min(t/d, |\sec(\alpha_i)|), \alpha_i \in [0, \pi] \tag{5.14}$$

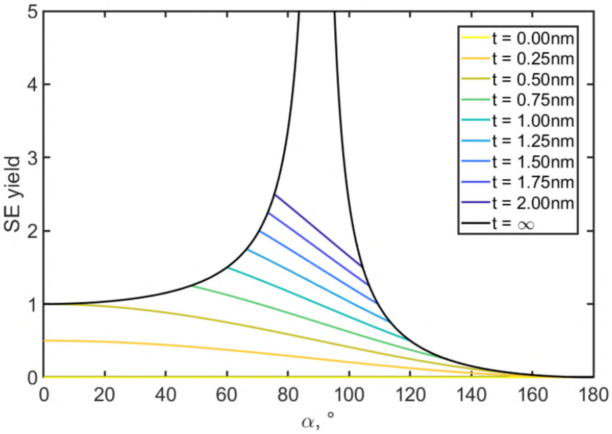

Figure 5.5: Dependence of SE yield on surface inclination angle relative to the primary electron beam and local sample thickness defined by **Equation 5.14**.

5.3 Materials and Methods

The proposed physical model of SEEBIC contrast formation allowed us to simulate SEEBIC images based on the surface structure extracted from experimental ET reconstructions. Experimental SEEBIC images were acquired using an aberration-corrected "cubed" Thermo Fisher Themis Z TEM operated at an acceleration voltage of 200 kV and a beam current of 500 pA. A custom-made transimpedance amplifier with a total gain of 2 GV/A (0.2 GV/A at the first amplification stage) and bandwidth of 8 kHz, electrically connected to the sample via a DENSsolutions Wildfire holder, was used to convert the SEEBIC signal into a voltage signal digitized by the Attollight OUDS II scan engine along with the amplified HAADF-STEM detector signal. No image filtering was applied during post-processing. Prior to analysis, the samples were Ar/O_2 plasma (3:1) cleaned to avoid a build-up of a layer of carbon contamination during the acquisition of SEEBIC data, as well as to remove surface ligands hindering topography imaging. Electron tomography data were acquired over ±72° with tilt increments of 3°, and reconstructions of tilt series were performed using the ASTRA Toolbox 1.90 for MATLAB 2022a. Visualization of 3D reconstructions was performed using the Amira 5.4.0 software.

Image simulations were performed in MATLAB 2022a using both synthetic 3D data and experimental data sets obtained using ET. The first step in the simulation algorithm is a transformation of the data into a binary volume using Otsu thresholding [100]. Next, experimental data are processed using the erode/dilate procedures to obtain smooth surfaces and remove artifacts related to the binarization of the data. Surface normals are calculated from the 3D image gradient of the volume, and α is calculated for each voxel at the edge of the volume. The thickness map obtained by re-projecting a volume into XY-plane and the intensity of the SEEBIC image is calculated using **Equation 5.10**.

5.4 Results and Discussion

We used our proposed model to simulate the SEEBIC image of Au nanorod (**Figure 5.6**). From the image, it can be appreciated that the simulated SEEBIC image qualitatively resembles the experimental one showing bright contrast at the edges of the nanorod. However, a closer look at the simulated data reveals a contour-like pattern in the centre of the nanorod (see inset in panel (b) of **Figure 5.6**). This pattern is a signature of the staircase artifact arising due to the voxel-based nature of the 3D volumetric data. This effect can be minimized using a finer resolution of the grid (bigger size of the volume) at the cost of increased computational resources. Additionally, advanced smoothing algorithms [101] can be applied to the volume to decrease the effect of staircase artifacts. Line profiles taken along long axes of nanorods demonstrate qualitative correlation. However, the sharp transition of the contrast can be noticed in simulated SEEBIC images (as shown with black arrow in **Figure 5.6 c**). This can be attributed to the fact that our model does not take into account SEs emitted from the support film, whereas in reality, SEs emitted from the support can escape from under the nanorod contributing to the overall SEEBIC signal, making a contrast transition at the edges of the nanorods smoother.

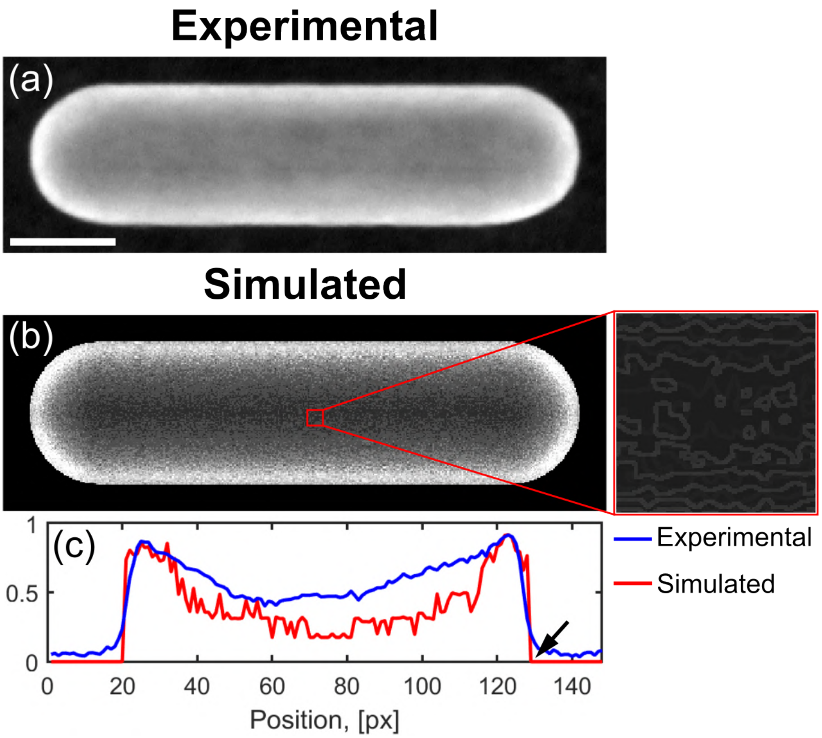

Figure 5.6: (a) Experimental and (b) simulated SEEBIC images of Au nanorod. (c) Line profile taken across the long axis of the nanorod for experimental and simulated SEEBIC images. Black arrow in panel (c) shows a sharp transition of the contrast between the nanorod and the background. Scale bar is 20 nm.

Next, we attempted to simulate the Ino decahedron (see previous chapter) to replicate the artifactual features that can be observed in **Figure 4.2**. We, therefore, created a model of an Ino decahedron and used it as an input for our simulation. **Figure 5.7** shows the comparison of experimental and simulated SEEBIC images. It can be seen that our model successfully replicates the line of bright contrast at the tip of the decahedron (as shown with a white arrow). Moreover, the simulated SEEBIC image shows areas of dark contrast that correlate with the experimental image (shown with a yellow arrow). It should be noted, that position and shape of these areas slightly deviate from the experimental images. This can be explained by the fact that we used a model of an Ino decahedron that has all the side facets of the same size, whereas, side facets of the real NP have different sizes as can be seen from ET reconstruction (**Figure 5.7 c**).

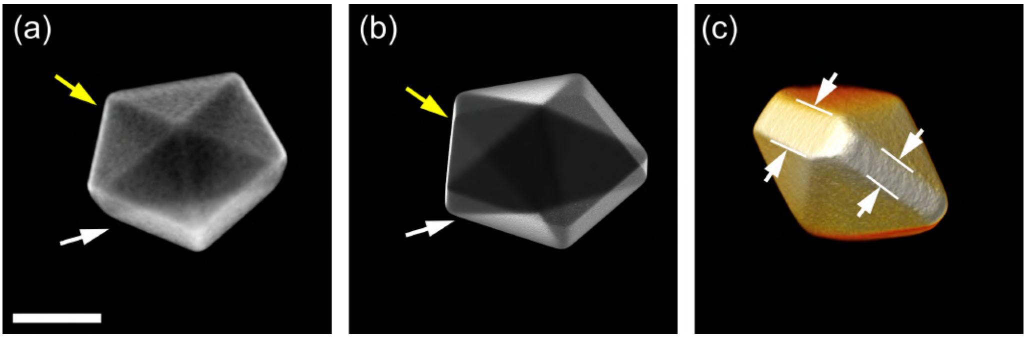

Figure 5.7: (a) Experimental and (b) simulated SEEBIC images of Au Ino decahedron. (c) ET reconstruction of NPs shown in panel (a). Scale bar is 50 nm.

A similar approach can be applied to the data obtained from the ET experiment. We used ET reconstructions of an Ino decahedron and triangular platelets shown in the previous chapter. **Figure 5.8** shows experimental SEEBIC images and simulated data based on ET reconstruction. Even though, simulated data suffer from artifacts related to the limited resolution of the 3D data, the main contrast features can be observed (e.g. line of bright contrast at the tip of the decahedron).

The proposed physical model and simulation results can be used as an aid for the interpretation of the contrasts arising in SEEBIC images that are not always straightforward to interpret. However, for reliable use of the simulated data, the simulation approach needs to be further improved. First of all, the proposed physical model does not take into account the parameters of the imaging system, the material of the specimen and the local electric fields of the sample. This can be achieved by coupling our model with Monte Carlo simulation. Another improvement of the model would be the addition of the ray tracing solver to account for the re-absorption of SEs by structural features of the sample itself which will allow us to simulate complex-shaped nanoparticles. The quality of the simulated data also needs to be improved by improving the quality of the input 3D models. This can be done using advanced smoothing techniques or using triangular mesh representation of 3D objects for the calculations. The use of triangular meshes for this task seems preferable, due to the fact that Monte Carlo simulations and ray tracing solvers work with triangular meshes.

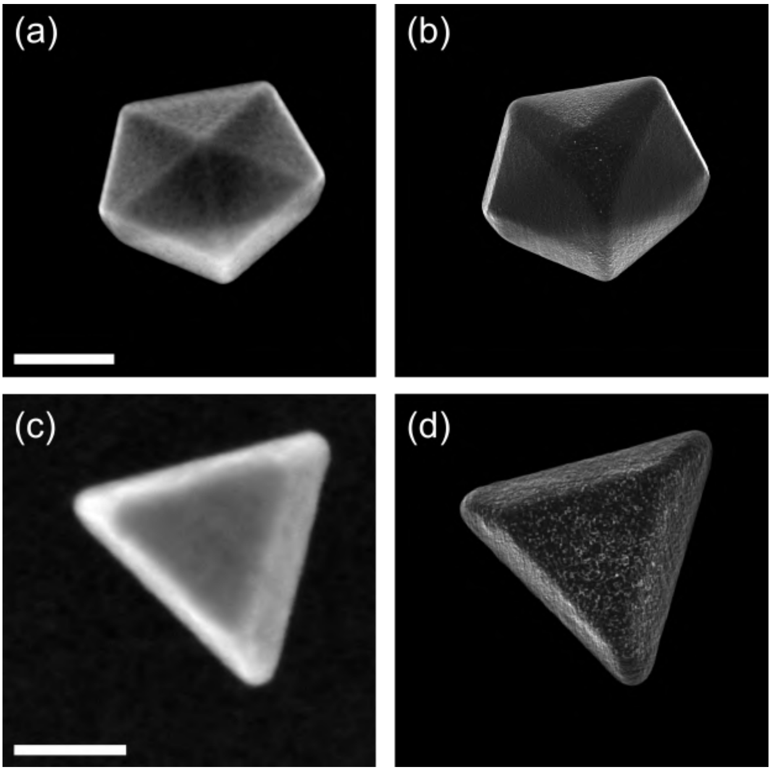

Figure 5.8: (a, c) Experimental and (b, d) simulated SEEBIC images of (a-b) Au Ino decahedron and (c-d) Au nanotriangles. Scale bars are (a) 50 nm, (c) 20 nm.

5.5 Conclusions

In this chapter, we derived a physical model of the interaction of the emitted SEs with the magnetic field of the objective lens that was used as a basis for the simulation of SEEBIC images. This physical model was used to simulate SEEBIC images based on synthetic 3D data and 3D data obtained from the ET experiment. Simulation data were shown to be capable of replicating contrast artifacts that can be seen in experimental SEEBIC images.

5.6 Appendix

$$I_2 = \begin{cases} \frac{1}{2} + \frac{1}{\pi} \int_{\pi}^{2\pi} \, d\phi \int_{0}^{-\arctan(\cot(\alpha)\csc(\phi))} \, d\theta \cos(\theta)\sin(\theta), \alpha \in \left[0, \frac{\pi}{2}\right] \\ \frac{1}{2} - \frac{1}{\pi} \int_{0}^{\pi} \, d\phi \int_{0}^{-\arctan(\cot(\alpha)\csc(\phi))} \, d\theta \cos(\theta)\sin(\theta), \alpha \in \left[\frac{\pi}{2}, \pi\right] \end{cases} \tag{5.15}$$

Using substitution $u = \cos(\theta)$, $du = -\sin(\theta)$

$$I_2 = \begin{cases} \frac{1}{2} - \frac{1}{\pi} \int_{\pi}^{2\pi} \, d\phi \int_{1}^{\cos(-\arctan(\cot(\alpha)\csc(\phi)))} \, duu, \alpha \in \left[0, \frac{\pi}{2}\right] \\ \frac{1}{2} + \frac{1}{\pi} \int_{0}^{\pi} \, d\phi \int_{1}^{\cos(-\arctan(\cot(\alpha)\csc(\phi)))} \, duu, \alpha \in \left[\frac{\pi}{2}, \pi\right] \end{cases} \tag{5.16}$$

With $\cos(\arctan(x)) = \frac{1}{\sqrt{x^2+1}}$, we get

$$\begin{aligned} I_2 &= \begin{cases} \frac{1}{2} - \frac{1}{2\pi} \int_{\pi}^{2\pi} \, d\phi \left(\frac{1}{1+(\cot(\alpha)\cos(\phi))^2} - 1 \right) \\ \frac{1}{2} + \frac{1}{2\pi} \int_{0}^{\pi} \, d\phi \left(\frac{1}{1+(\cot(\alpha)\cos(\phi))^2} - 1 \right) \end{cases} = \\ &= \begin{cases} \frac{1}{2} + \frac{1}{2\pi} \int_{\pi}^{2\pi} \, d\phi \frac{(\cot(\alpha)\csc(\phi))^2}{1+(\cot(\alpha)\csc(\phi))^2} \\ \frac{1}{2} - \frac{1}{2\pi} \int_{0}^{\pi} \, d\phi \frac{(\cot(\alpha)\csc(\phi))^2}{1+(\cot(\alpha)\csc(\phi))^2} \end{cases} = \\ &= \begin{cases} \frac{1}{2} + \frac{1}{2\pi} \int_{\pi}^{2\pi} \, d\phi \frac{1}{1+\tan^2(\alpha)\sin^2(\phi)}, \alpha \in \left[0, \frac{\pi}{2}\right] \\ \frac{1}{2} - \frac{1}{2\pi} \int_{0}^{\pi} \, d\phi \frac{1}{1+\tan^2(\alpha)\sin^2(\phi)}, \alpha \in \left[\frac{\pi}{2}, \pi\right] \end{cases} \end{aligned} \tag{5.17}$$

Using $1 = \sin^2(\phi) + \cos^2(\phi)$

$$I_2 = \begin{cases} \frac{1}{2} + \frac{1}{2\pi} \int_{\pi}^{2\pi} \, d\phi \frac{1}{\cos^2(\phi)+(1+\tan^2(\alpha))\sin^2(\phi)}, \alpha \in \left[0, \frac{\pi}{2}\right] \\ \frac{1}{2} - \frac{1}{2\pi} \int_{0}^{\pi} \, d\phi \frac{1}{\cos^2(\phi)+(1+\tan^2(\alpha))\sin^2(\phi)}, \alpha \in \left[\frac{\pi}{2}, \pi\right] \end{cases} \tag{5.18}$$

This integral has already been tabulated in [102]

$$I_2 = \begin{cases} \frac{1}{2} + \frac{(-1)!!}{2\sqrt{1+\tan^2(\alpha)}}, \alpha \in \left[0, \frac{\pi}{2}\right] \\ \frac{1}{2} - \frac{(-1)!!}{2\sqrt{1+\tan^2(\alpha)}}, \alpha \in \left[\frac{\pi}{2}, \pi\right] \end{cases} \tag{5.19}$$

We know that $(-1)!! = 1$, $\frac{1}{1+\tan^2(\alpha)} = |\cos(\alpha)|$, and

$$|\cos(\alpha)| = \begin{cases} \cos(\alpha), \alpha \in \left[0, \frac{\pi}{2}\right] \\ -\cos(\alpha), \alpha \in \left[\frac{\pi}{2}, \pi\right] \end{cases} \tag{5.20}$$

Such that

$$I_2 = \begin{cases} \frac{1}{2} + \frac{\cos(\alpha)}{2}, \alpha \in \left[0, \frac{\pi}{2}\right] \\ \frac{1}{2} + \frac{\cos(\alpha)}{2}, \alpha \in \left[\frac{\pi}{2}, \pi\right] \end{cases} \tag{5.21}$$

This gives the final expression

$$I_2 = \frac{1 + \cos(\alpha)}{2}, \alpha \in [0, \pi] \tag{5.22}$$

Chapter 6

High-throughput Morphological Helicity Quantification of Twisted and Wrinkled Gold Nanorods

---

This chapter introduces a high-throughput methodology that combines images acquired by SEEBIC with quantitative image analysis. As a result, the helicity of hundreds of nanoparticles can be quantified in less than one hour. When combining the drastic gain in data collection efficiency of SEEBIC with a limited number of electron tomography data sets, a better understanding of how the chiral structure of individual chiral nanoparticles translates into the ensemble chiroptical response can be reached.

6.1 Introduction to Chirality in Inorganic Nanoparticles

The possibility of transferring the concept of chirality to inorganic NPs has resulted in a new class of materials with exciting properties and promising applications [16, 103–105]. In the case of metal NPs, the combination of a chiral morphology and plasmonic properties results in unusually high optical activity, combining CD and optical rotatory dispersion, i.e., the differential extinction (absorption plus scattering) of left- and right-handed circularly polarized light. Differences in extinction up to 20% have been reported [106–110], which are orders of magnitude higher in comparison to CD effects typically observed for chiral molecules, primarily due to stronger light-matter interactions under circularly polarized light. Recent reports have demonstrated that

---

This chapter is based on the following paper:

Vlasov E., Heyvaert W., Ni B., Van Gordon K., Girod R., Verbeeck J., Liz-Marzán L.M., Bals S. High-throughput morphological chirality quantification of twisted and wrinkled gold nanorods (submitted to ACS Nano).

The contribution of the author of the thesis consisted of conducting SEEBIC experiments, acquisition and reconstructions of ET data; analysis and processing helicity quantification data. Synthesis of twisted nanorods was carried out by Dr. B. Ni at the University of Konstanz, Germany. Synthesis of wrinkled nanorods was done by Dr. K. Van Gordon at the BioNanoPlasmonics Laboratory at CIC biomaGUNE, Spain.

chiral metal NPs are excellent candidates for biosensing [111–113], separation [114–116], catalysis [117–119], treatment of diseases [120–122], and photonics [123–125]. However, reliable implementation of these and other applications requires a much deeper understanding of the connection between NP morphology and optical activity.

6.2 Growth and 3D Characterization of Chiral NP by ET

The colloidal synthesis of chiral NPs has recently emerged as a promising route for the fabrication of 3D chiral structures because of its scalability and low cost. A few synthesis procedures have been proposed to transfer chirality to inorganic NPs. One of them is a chiral ligand-mediated approach that relies on chiral ligands, amino acids, short peptides, and chiral derivatives. This approach uses enantioselective organic-inorganic interaction or templating to transfer chirality to achiral inorganic NPs. Using enantioselective organic-inorganic interaction, chiral morphologies can be achieved by controlling the adsorption of small chiral molecules on high Miller index surfaces $\{hkl\}$ ($h \neq k \neq l \neq 0$) [106, 108, 110, 126–128]. It was shown that combinations of specific chiral crystal facets with different types of chiral inducers lead to handedness-dependent changes in the surface orientation of chiral adsorbates on chiral crystal facets. For example, the enantioselective organic-inorganic interaction approach was used to synthesize chiral Au NPs from achiral seeds using cysteine enantiomers [106]. The chiral morphology, in this case, was attributed to the selective adsorption of cysteine molecules by $\{321\}^R$ and $\{321\}^S$ facets. A similar approach was used to synthesise chiral twisted Au nanorods (NR) that have diagonal edges with 4-fold symmetry (**Figure 6.1**). Twisted morphology was attributed to the development of chiral {521} facets in the form of protrusions (tilted ridges) on the initial NR [110].

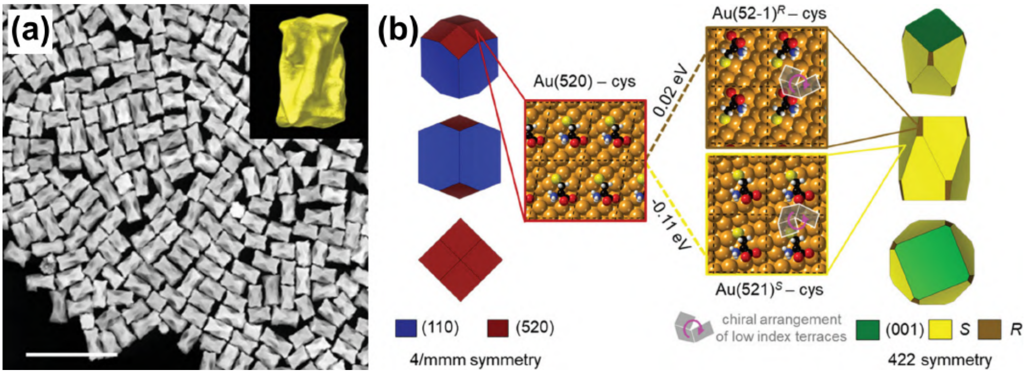

Figure 6.1: (a) Overview HAADF-STEM image of twisted Au NRs synthesised using L-cysteine chiral inducer. Inset in panel (a) show the 3D structure of individual NR. (b) Schematic showing growth mechanism: enantioselective adsorption of L-cysteine on (520) facets leads to the development of chiral {521} facets. Scale bar is 500 nm. Adapted from [110] under the terms of the CC BY 4.0 license.

The ability of surfactants to form micelles in aqueous solution and their tendency to adsorb at interfaces can also be used as a tool for chiral NPs production. Under specific physicochemical conditions, helical micelles can be formed and used as a template for chiral growth (**Figure 6.2**). Such surfactant-assisted growth allows the engineering of chiral gold nanorods using N,N,N-trimethylhexadecan-1-aminium chloride (CTAC) and dissymmetric molecules, e.g., 1,1′-bi-2-naphthol (BINOL) or 1,1′-binaphthyl-2,2′-diamine (BINAMINE) as shown in [107, 109].

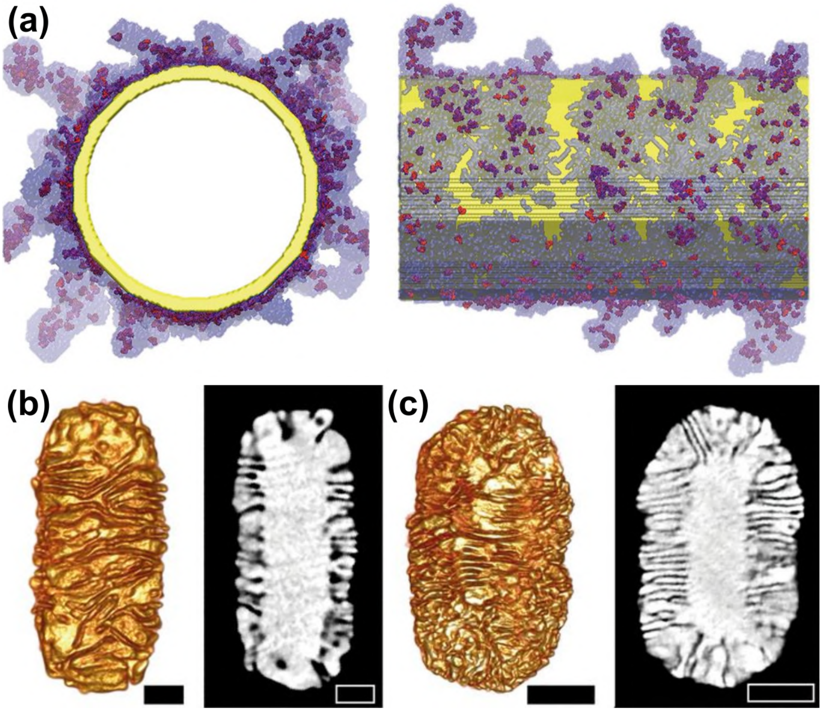

Figure 6.2: (a) Chiral CTAC-BINOL micelle. (b, c) ET visualization of wrinkled Au NRs of different dimensions. ET reconstructions reveal the surface topography of wrinkled NR, whereas orthoslices show the growth of wrinkles from the Au NR seeds and the internal structure of the wrinkle network. Scale bars: (b) 20 nm, (c) 50 nm. Reprinted with permission from [107]. Copyright 2020 American Association for the Advancement of Science.

As can be seen from **Figures 6.1-6.2**, chiral NPs often feature a complex morphology. The usual consideration of unavoidable polydispersity in colloidal systems becomes more relevant because, on top of potential variations in overall size and shape, each chiral NP presents slightly different morphological features. Hence, high-resolution characterization at the single particle level is required to comprehend structure-property relations for these systems. Therefore reliable 3D information about nm and sub-nm scale features is required. The conclusions on the chiral morphology and surface faceting can be made based on SEM images. However, the spatial resolution of SEM is limited by a few nm and does not allow to resolve fine structural features (e.g. similar to the ones shown in **Figures 6.2**). Therefore, electron tomography is used to evaluate the morphology of chiral NPs with high spatial resolution and get insights on chiral growth mechanisms [107, 109, 110].

Recently, quantitative methodology to objectively characterize the helical morphology of Au NR was reported [129]. In short, this method is based on analyzing a 3D reconstruction volume of a chiral Au NR, according to different cylindrical sections (**Figures 6.3**). For each section, the so-called directionality is computed, and the preferred orientation of the corresponding diagonal lines is identified, which corresponds to helical features in the 3D volume. In this manner, a "helicity function" is defined, which can be interpreted as a measure for the distribution of helical inclination angles of the surface features of a given NR (**Figure 6.4**).

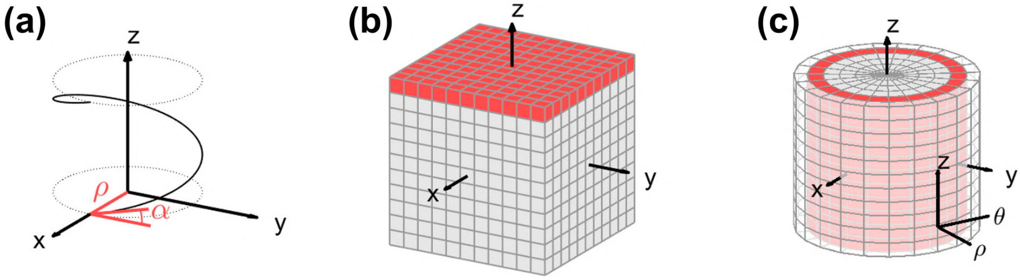

Figure 6.3: (a) Helix around the z-axis with radius ρ and inclination angle α; (b) discrete voxel grid in Cartesian coordinates; and (c) discrete voxel grid in cylindrical coordinates. Adapted from [129] under the terms of the CC BY 4.0 license.

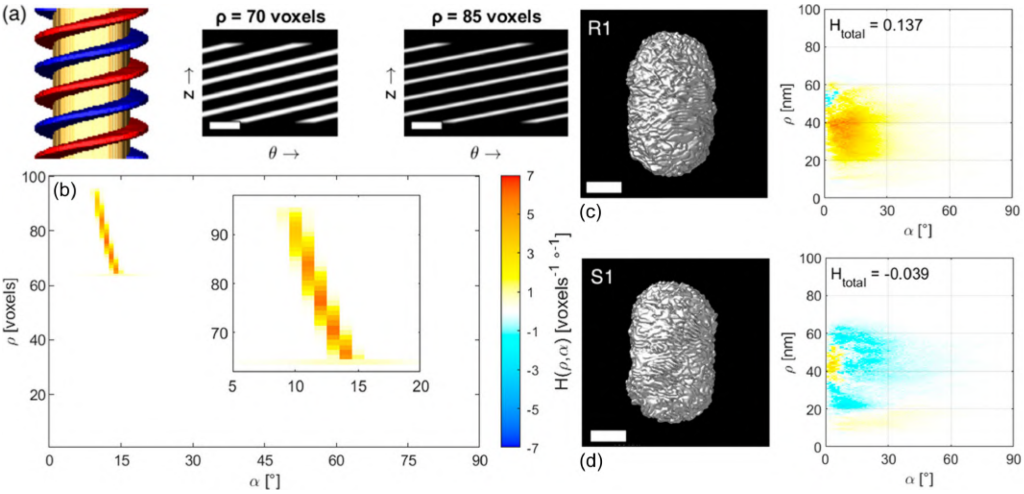

Figure 6.4: (a) Simulated helix with two of its cylindrical sections at ρ = 70 voxels and ρ = 85 voxels. Scale bars are 100 voxels. (b) Helicity function $H(\rho, \alpha)$ histogram and zoomed view (inset) of the peak corresponding to the helical shell of the model. (c, d) Isosurface visualizations of the ET reconstructions for chiral Au NRs along with a plot of the corresponding helicity function $H(\rho, \alpha)$ The total helicity H_{total} is also indicated for each Au NR. Scale bars are 50 nm. Adapted from [129] under the terms of the CC BY 4.0 license.

6.3 Motivation

A drawback of this methodology originates from the extremely time-consuming nature of electron tomography, which limits the number of NRs that can be investigated in practice. Acquisition times of 1 hour per particle are not uncommon, even though recent developments have enabled reducing acquisition time down to a few minutes using more advanced tomography approaches [42–44]. Nonetheless, the data processing and reconstruction steps that follow after the tilt series acquisition are time-consuming. Consequently, one can typically analyze approximately 10 NPs in a timeframe of one day, whereas extrapolation of single-particle properties to the ensemble level while considering polydispersity demands a high-throughput analysis of the chiral NP morphology so that average structural descriptors can be extracted with adequate statistical rigour. In this chapter, the use of SEEBIC images for high-throughput quantification of the helical morphology in nanomaterials and retrieval of ensemble-level information about the helical morphology is discussed.

6.4 Materials and Methods

Three different types of Au NRs were analyzed, each yielding a twisted or "wrinkled" morphology. Sample 1 is a left-handed sample of twisted Au NRs, which have large diagonal edges with 4-fold symmetry and were synthesized using D-cysteine as a chiral inducer, as described by Ni *et al.* [110] (**Figure 6.5 a, d** and **Figure 6.6 a-c**). Samples 2 and 3 are wrinkled Au NRs synthesized as described by González-Rubio *et al.* [107] (**Figure 6.5 b, e, c, f** and **Figure 6.6 d-i**). These two samples were synthesized with different (S)- and (R)- enantiomers of BINAMINE, using single crystalline Au NR seeds. The left column in **Figure 6.6** shows 2D projections of representative NRs, acquired using HAADF-STEM, a standard technique to investigate NPs.

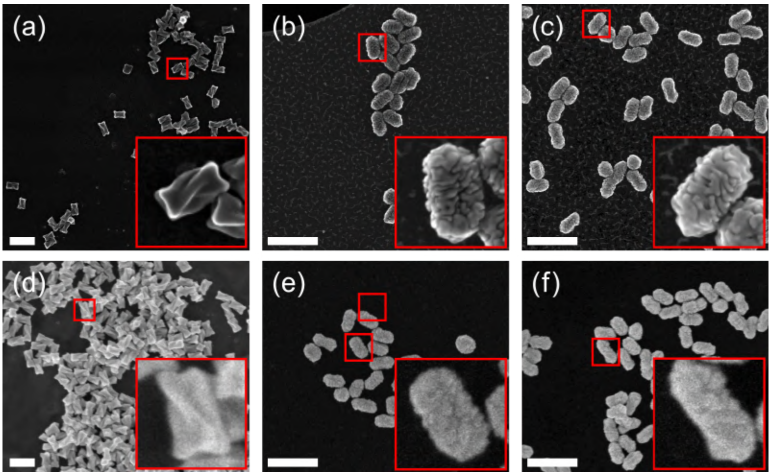

Figure 6.5: Overview (a-c) SEEBIC and (d-f) SEM images for (a, d) sample 1, (b, e) sample 2, and (c, f) sample 3. In each image, a selected particle is enlarged in the inset. Scale bars are 250 nm.

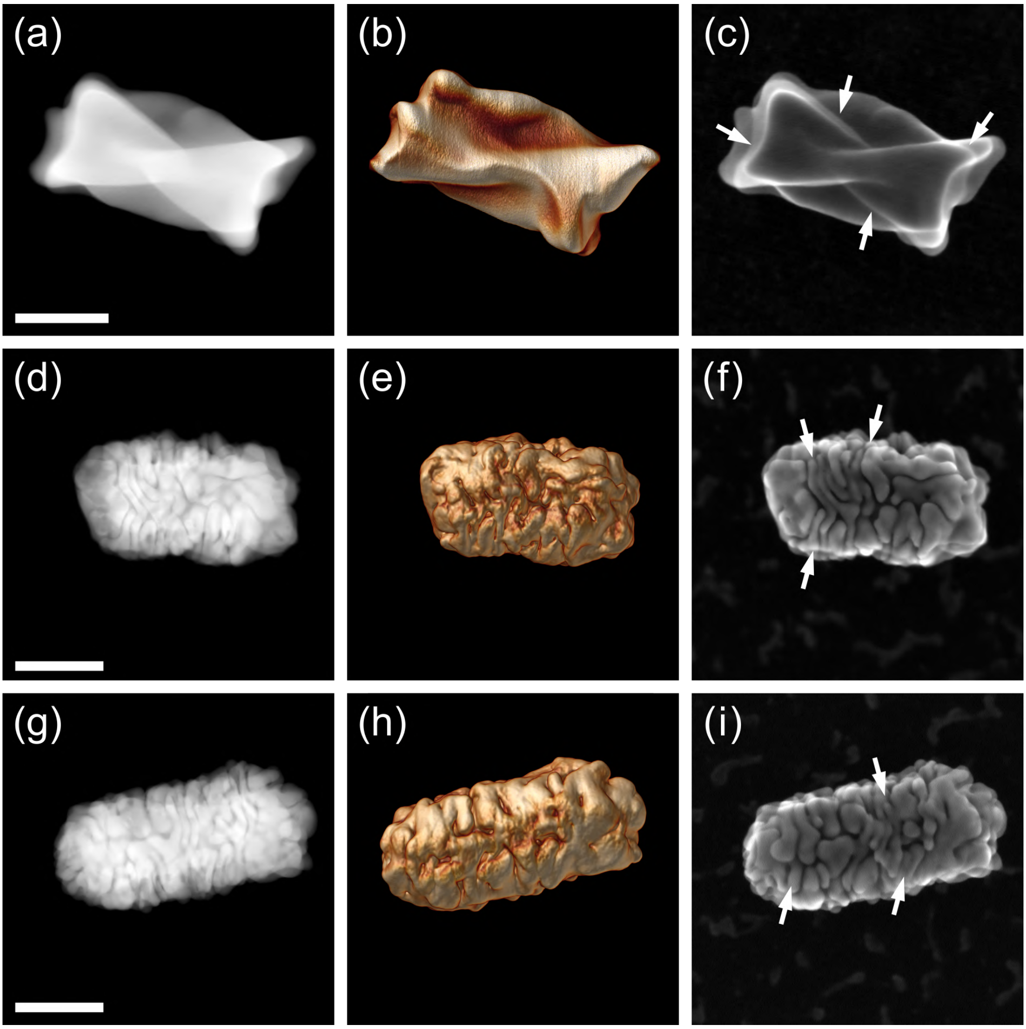

Figure 6.6: High-magnification (a, d, g) HAADF-STEM, (b, e, h) ET visualizations, and (c, f, i) SEEBIC images of a representative particle for (a-c) sample 1, (d-f) sample 2, and (g-i) sample 3. White arrows indicate discrepancies between SEEBIC and electron tomography data. Scale bars are 50 nm.

ET data were acquired over a tilt range of ±72°, with tilt increments of 3°, using an aberration-corrected "cubed" Thermo Fisher Themis Z TEM, operated at an acceleration voltage of 200 kV and a beam current of 50 pA. Reconstructions of the tilt series were performed using the SIRT algorithm implemented in ASTRA Toolbox 1.90 [25] for MATLAB 2022b. Visualization of 3D reconstructions was carried out using the Amira 5.4.0 software. SEEBIC imaging at the single-particle level was performed at an acceleration voltage of 200 kV and a beam current of 500 pA. A custom-made TIA with a total gain of 2×10^9 V/A and a bandwidth of 8 kHz, electrically connected to the sample via a DENSsolutions Wildfire holder, was used to convert the SEEBIC signal into a voltage signal digitized by the Attolight OUDS II scan engine, along with HAADF-STEM detector signal. No image filtering was applied during post-processing. High-throughput SEEBIC data were acquired at an acceleration voltage of 60 kV and a beam current of 500 pA.

SEEBIC images of 1024 × 1024 pixels were acquired with a dwell time of 200 μs, leading to a total acquisition time of approximately 3.5 minutes per image. HAADF-STEM images were acquired simultaneously with SEEBIC and used for automatic segmentation during the data processing step. SEM images were obtained using Thermo Fisher Helios Nanolab 650 with nominal spatial resolution down to 0.8 nm operated at an acceleration voltage of 5 kV and electron beam current of 50 pA.

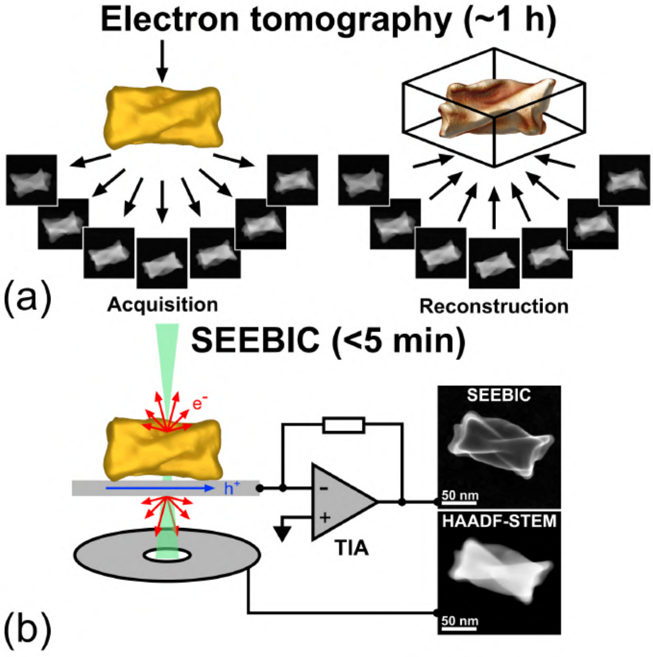

Figure 6.7: Schematic description of the working principles of (a) electron tomography, (b) SEEBIC. Red arrows in panel (b) indicate directions of SE emission from the NP surface; the blue arrow indicates the net hole current flowing into the TIA input.

6.5 Results and Discussion

6.5.1 Qualitative Comparison

Shown in the right column of **Figure 6.6** are SEEBIC images, acquired simultaneously with the HAADF-STEM images (left column). As already explained in previous chapters, SEEBIC relies on the detection of current arising from holes generated by the emission of SEs from the sample (**Figure 6.7**). The obtained SEEBIC images of chiral NRs in **Figure 6.6** are in close agreement with the results of ET experiments. For the latter, a tilt series of 51 HAADF-STEM images (with an approximate total acquisition time of about 1 hour) was used as input for 3D reconstruction, whereas the SEEBIC image was acquired in less than 5 minutes. Minor discrepancies between HAADF, SEEBIC and ET are also noticeable, which we attribute to three main effects: backside contribution, imperfect ET reconstructions and projection overlap. We assume that SEEBIC contrast predominantly originates from the NP surface and more specifically the top one, as most SEs generated at the bottom of the NP are reabsorbed by the support film. However, as seen in **Figure 6.6 c** (white arrows), a contribution from the bottom surface cannot be fully prevented because of gaps created by the helical ridges that provide an escape way for SEs (**Figure 6.8**). As further explained in the discussion on quantification of helicity, this effect has little impact on the overall statistics.

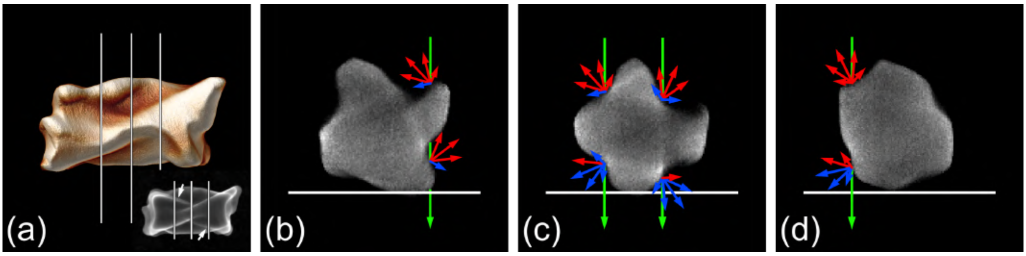

Figure 6.8: (a) ET visualisation of NP shown in **Figure 6.6** with indicated positions of taken orthoslices. (b-d) Orthoslices with an indication of SE emission. Red arrows indicate SEs escaping the surface of NPs without being absorbed by the support or structural features, and blue arrows indicate recaptured SEs. Lengths of red and blue arrows are indicative of the number of SEs emitted in each direction and proportional to the cosine angle between this direction and the surface normal. Green arrows indicate the primary electron beam. White arrows indicate regions with artifactual contrast.

The second type of discrepancy is seen in samples 2 and 3, where white arrows (**Figure 6.6 f, i**) indicate minor discrepancies between SEEBIC and ET, corresponding to a lack of wrinkled features in the ET reconstruction. This is likely related to imperfections during the ET process, e.g., resulting from missing wedge artifacts, which are known to result in a reduction of the reconstruction resolution and leading to blurring of the reconstructed volume (see **Figure 6.9**).

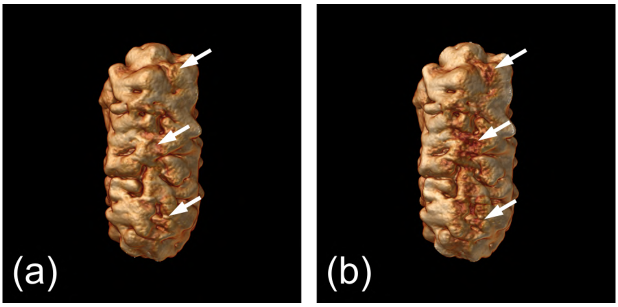

Figure 6.9: Volume renders of experimental data for sample 3 showing an influence of “missing wedge” on electron tomography reconstruction quality. (a) Original data with a tilt range of [−72°, +72°], (b) data with artificially increased “missing wedge” by reducing the original data tilt range to [−60°, +60°]. White arrows show discrepancies between reconstructions (a) and (b).

Finally, we also observed that the wrinkled features of samples 2 and 3 appear sharper in the HAADF-STEM images, in comparison to the ET reconstructions and SEEBIC images. As illustrated in **Figure 6.10** this is likely the result of overlapping of the features in projection images and not due to electron beam damage (**Figure 6.11**).

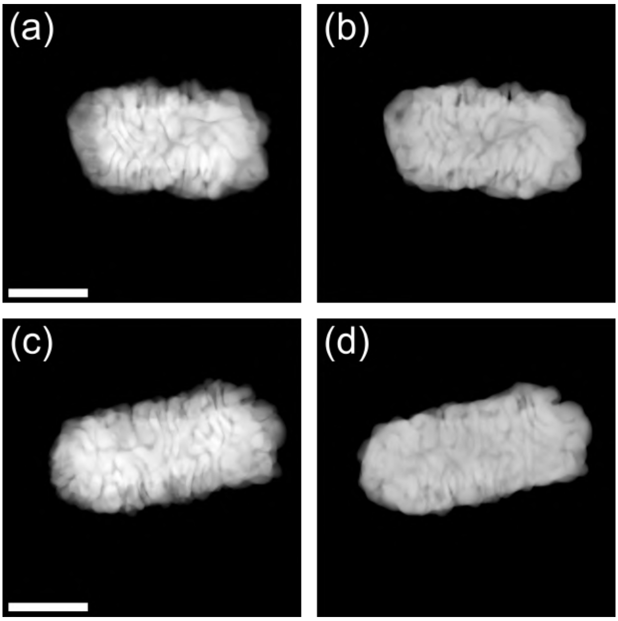

Figure 6.10: (a, c) HAADF-STEM images of "wrinkled" nanoparticles of (a) sample 2 and (c) sample 3, acquired simultaneously with SEEBIC images, prior to the acquisition of electron tomography data. (b, d) Re-projections of the electron tomography reconstruction corresponding to 0° tilt angle, taken from the same nanoparticles. Note that wrinkle sizes do not change between HAADF-STEM and re-projection images, indicating no significant re-shaping of the nanoparticles during electron tomography acquisition. Therefore, the sharpness of the wrinkles on HAADF-STEM images compared to electron tomography reconstructions and SEEBIC is related to their overlap. Scale bars are 50 nm.

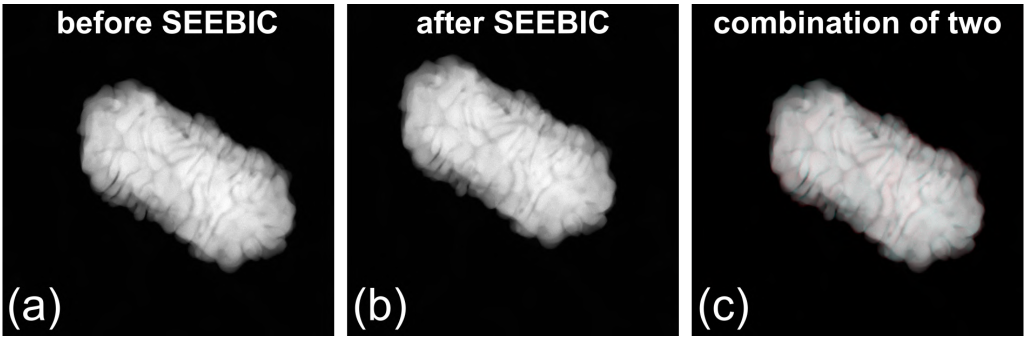

Figure 6.11: (a-b) HAADF-STEM images of a single NP (sample 1) acquired (a) before and (b) after SEEBIC imaging. (c) Stereoanaglyph constructed using images (a) and (b) after their alignment using a cross-correlation algorithm. Cyan and red colours in panel c are indicative of a degree of discrepancy between images (a) and (b).

6.5.2 Quantitative Comparison

Figures 6.6 illustrates that SEEBIC images provide a visualization of the surface morphology of chiral NPs with at least similar quality as that obtained by ET, but with a drastic gain in data collection efficiency. This gain can be further improved by selecting a relatively low magnification (see below), taking into account the overall size of the NPs, as well as the characteristic size of the structural features at their surface. In this manner, every SEEBIC image may display multiple particles dispersed on a TEM support, so that SEEBIC imaging of hundreds of NRs per hour becomes possible. The imaging magnification needs to be optimized so that all the relevant structural features can be distinguished from the image while keeping a sufficient number of NPs located within the field of view. For example, the samples studied in the current work have comparable particle sizes, but samples 2 and 3 have smaller surface features than those in sample 1 and therefore a higher magnification is required to resolve them (see **Section 6.7** of current chapter).

Quantification Method

Once SEEBIC images of hundreds of NRs have been acquired, their helicity can be readily analyzed. To this aim, we modified a methodology that was previously reported by our group to quantify the morphology of chiral NRs, based on ET experiments [129]. The current workflow is visualized in **Figure 6.12**. The particles are first localized in HAADF-STEM and SEEBIC images that are simultaneously acquired (**Figure 6.12**). In HAADF-STEM images, the NPs appear bright against a dark background. Using Otsu thresholding [100], followed by a connected-components analysis [130], the particle shapes are then segmented, and their outlines transferred to the corresponding SEEBIC images (**Figure 6.12**). Next, the long axis of the NRs is defined by fitting an ellipse to the segmentation results. This axis is assumed to correspond to the helical axis of the NR during further quantification. Then, the gradient of the intensity of the SEEBIC image is calculated to obtain, for each pixel, the gradient magnitude and its orientation with respect to the direction of the helical axis. We remap the orientation between [-90°, +90°], ultimately yielding the helical inclination angle α of the surface features for a given NR (**Figure 6.12**). To give more importance to well-defined topological features, which are encoded in the intensity changes of the SEEBIC image, we further attribute a weight to each pixel corresponding to its gradient magnitude. For quantification (**Figure 6.12**), the NR helical structure can then be presented as a weighted histogram of the obtained inclination angles. To accurately describe the handedness of a structure, we define the helicity function $H(\alpha)$ as the sum between the histogram bins with right-handed (positive) inclination angles and those with left-handed (negative) inclination angles. As such, the helicity function will be positive for a given value of α if the structure is dominantly right-handed at this inclination angle and *vice versa*. Importantly, these helicity histograms can be readily aggregated over many particles to yield the average plot of helicity and orientation in a polydisperse sample. In addition, and as we previously reported for ET, each histogram of a particle or an ensemble can be integrated over the orientation range. This yields a single, easily interpretable value representing the total helicity of a particle H_{seebic} or a sample H_{avg}. This value will be -1 for ideally left-handed structures, 0 for non-helical structures, and +1 for perfect right-handed structures.

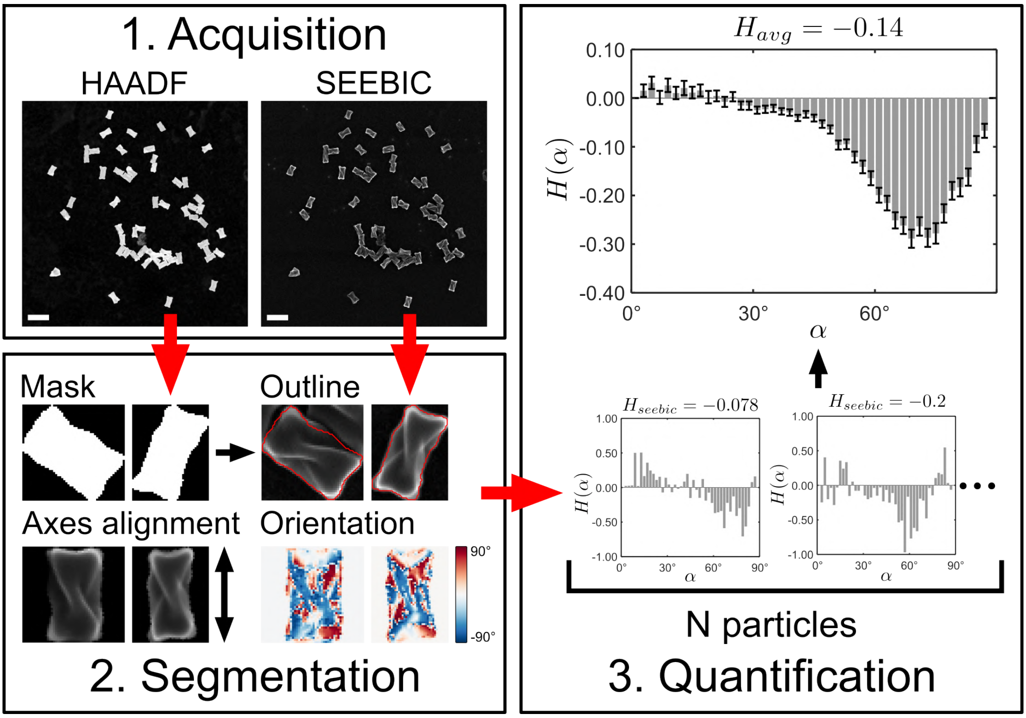

Figure 6.12: Proposed workflow to quantify the helical morphology of NRs imaged by simultaneous HAADF-STEM and SEEBIC acquisitions. First, a SEEBIC and a HAADF-STEM images are acquired simultaneously at low magnification. Next, the NRs in the HAADF-STEM image are segmented to separate their projected shapes from the background and a connected-components analysis is used to identify individual NRs (red boundaries). The helical inclination angle α is calculated from the gradient of the SEEBIC image. Finally, the helicity function is calculated separately for each NR, and all results are averaged to retrieve the helicity function of the ensemble. The total helicity H_{avg} can be calculated by integrating the helicity function for all NRs. The average helicity plot shows the data obtained from N particles, error bars represent the standard error for each data bin. Scale bars are 500 nm.

We first evaluated our method for helicity quantification by comparing optical characterization at the ensemble level (**Figure 6.13**) with SEEBIC average helicity (**Figure 6.14** - **Figure 6.16**). Optical activity plots show positive g-factors for samples 1 and 3 (optically left-handed) and a negative g-factor for sample 2 (optically right-handed). For SEEBIC characterization, seven images of sample 1 were acquired at a magnification of 28.5 k× (corresponding to a total field of view of approximately 2700 × 2700 nm^2), to analyze 327 NRs. For samples 2 and 3, fourteen and twelve SEEBIC images were acquired at a magnification of 57 k× (field of view of approximately 1300 × 1300 nm^2), to analyze 174 and 348 NRs, respectively. A complete overview of all SEEBIC images can be found in **Section 6.7**. From this analysis, the total average helicity was calculated to be -0.14 for sample 1, +0.033 for sample 2, and -0.039 for sample 3, indicating an average left-handed geometry for samples 1 and 3 and a right-handed one for sample 2. These results are in excellent agreement with the optical characterization and demonstrate that SEEBIC-based average helicity calculations are adequately describing the handedness of the ensemble.

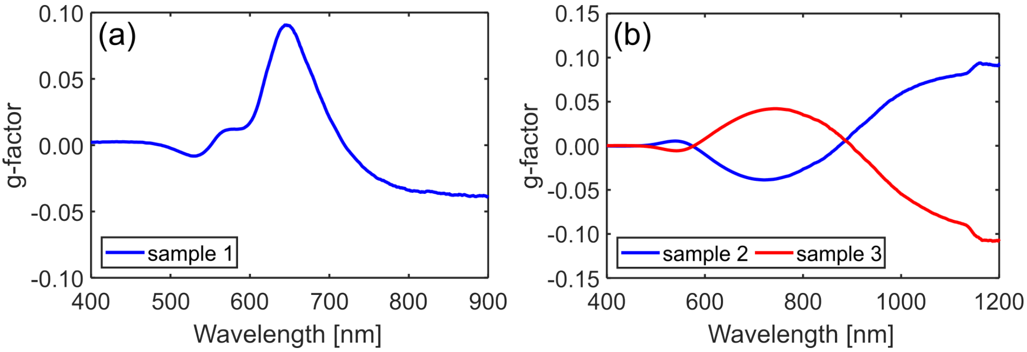

Figure 6.13: Optical activity (g-factor) plots for the studied samples: (a) sample 1, (b) samples 2 and 3.

Next, we compared the results of SEEBIC ensemble (**Figures 6.14 a, 6.15 a, 6.16 a**) and single-particle (**Figures 6.14 c, 6.15 c, 6.16 c**) helicity quantification with our previous approach based on the ET reconstruction for a single NR (**Figures 6.14 b, 6.15 b, 6.16 b**) [129]. The ET helicity plots show a distribution of chiral features, indicating the prevailing handedness at various distances from the helical axis and inclination angles. In other words, the approach "unwraps" a chiral NR layer-by-layer, such that the higher the radius (ρ), the closer the feature is located to the NR surface. The helicity function here is encoded in colours: red for right-handed (positive helicity function), blue for left-handed (negative helicity function) morphological features. As with SEEBIC, the plots can be integrated over the radius and orientation ranges to yield a pseudoscalar descriptor of the total helicity, H_{tomo}. While not strictly equal due to the differences in their calculation, the SEEBIC values (H_{seebic} or H_{avg}) and the total helicity from ET data H_{tomo} both integrate the orientation of surface features of chiral NPs and should therefore be correlated.

For sample 1, the angular distribution of helical features in **Figures 6.14 a** shows that the predominant left-handed helical features in these particles are oriented with rather steep inclination angles, around 70°, whereas right-handed features with low inclination angles are also present. The analysis based on the ET reconstruction of a representative NR, shown in **Figures 6.14 b**, also shows predominant left-handed features with angles around 60° (cloud of blue data points indicated with a blue arrow in the histogram) and a mixture of right- and left-handed features with small inclination angles (indicated with a red arrow in the histogram). This comparison demonstrates that quantification of the average structure using the SEEBIC approach for sample 1 is in good agreement with ET data. The main left-handed peak of the angular distributions in **Figures 6.14 a-b** corresponds to the diagonal edges of the NRs, whereas right-handed low-angle peaks can be attributed to the contribution of the edges on the NR tips (**Figures 6.17 - 6.19**). Maps in **Figures 6.18** show the distribution of inclination angles on the SEEBIC images, confirming that the NR tips have low inclination angles (see arrows and colour coding indicating low angle values on the tips). Quantification results with artificially removed tips confirmed our findings, showing no features at low angles in the quantification results (**Figures 6.19**). At the single particle level, tip edges do not appear to have a preferred orientation (see **Figures 6.14 b-c** and **Figures 6.17**), however, averaging over a large ensemble (327 particles) shows that they are predominantly right-handed. Quantitative data obtained from a SEEBIC image of the same NR used for ET are shown in **Figures 6.14 c**. Good agreement was found with both ensemble-averaged data obtained through SEEBIC and the results obtained by ET as negative helicity values were obtained.

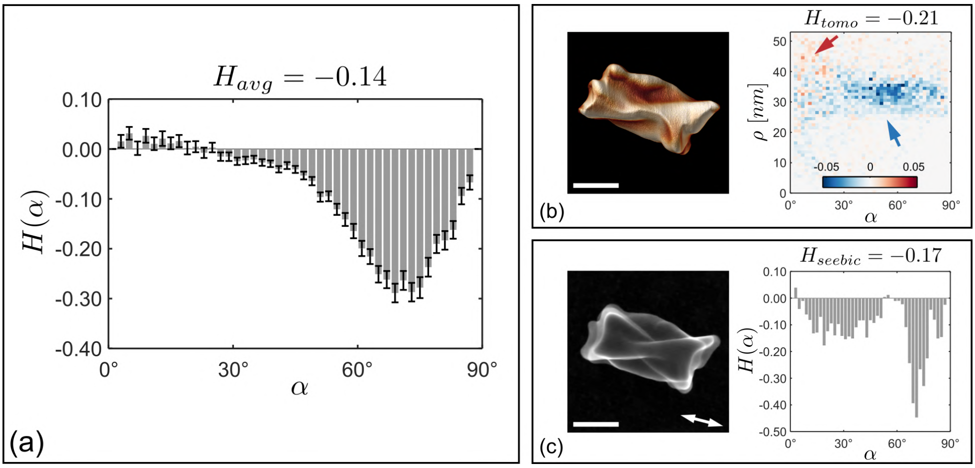

Figure 6.14: Results of chirality quantification for sample 1. (a) Helicity quantification of a NR ensemble, based on seven overview SEEBIC images; (b) Helicity analysis from an ET reconstruction; (c) Helicity analysis based on the SEEBIC image of a single particle. Plots in panels (a) and (c) show the angular distributions of morphological chiral features for the NRs present in the SEEBIC images. The plot in (b) shows the distribution of morphological chiral features, with various inclination angles and distances from the helical axis of the NR. The orientation of the helical axis in panel (c) is indicated by a double-headed arrow. Scale bars are 50 nm.

Sample 2 yields an average right-handed morphology, with a maximum of angular distribution around 50-60° (**Figures 6.15 a**). This correlates well with ET-based quantification results, thereby demonstrating the diffuse distribution of mainly right-handed features in the histogram, as shown by the red arrow in **Figures 6.15 b**. Both SEEBIC ensemble-averaged and ET-based results also show a presence of features with mixed handedness, oriented with low inclination angles ($< 30°$) (blue arrow in **Figures 6.15 b**). A thorough analysis of the experimental data (**Figure 6.20**, **6.21**) did not reveal a strong influence of edges, tips or SEEBIC artifacts on the orientation maps and on the helicity plots at the level of a single particle. From the standard error in **Figures 6.15 a**, it can be seen that these specific features are randomly distributed and cancel out each other's contribution when averaged over a large ensemble. In terms of absolute helicity, both SEEBIC and ET methods at the single particle level as well as the ensemble SEEBIC measurement reveal a less helical character than sample 1 with a 5-10 fold decrease in value. This again demonstrates the good correlation between the SEEBIC and ET approaches. Interestingly, the decrease in helicity also correlates with a lower peak g-factor (**Figure 6.13 b**), again showing the value of helicity measurements to link morphological chirality with optical properties. Sample 3, on the other hand, shows an average left-handed structure (**Figure 6.16 a**), in agreement with the analysis based on ET (**Figure 6.16 b**). However, the latter additionally shows the presence of both left- and right-handed features with small inclination angles (shown with a red arrow), which are located close to the NR surface (note high values of ρ for these features).

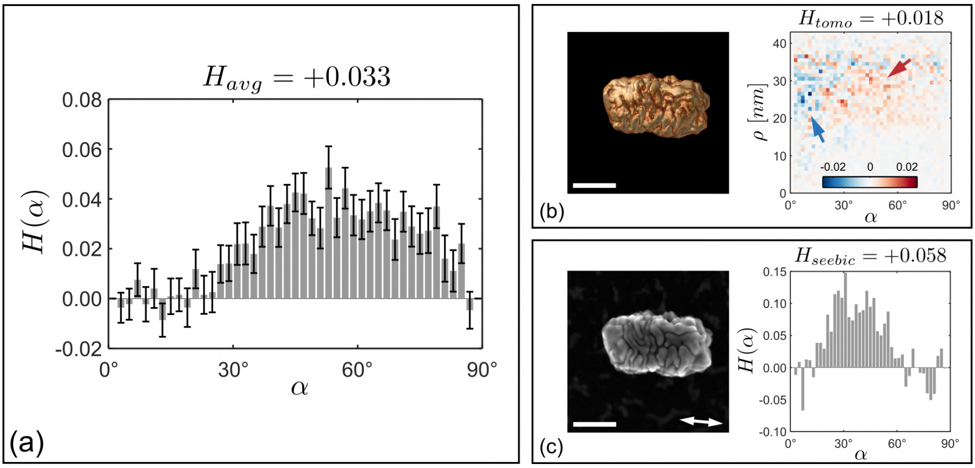

Figure 6.15: Results of chirality quantification for sample 2. (a) Helicity quantification of a NR ensemble, based on fourteen overview SEEBIC images; (b) Helicity analysis from an ET reconstruction; (c) Helicity analysis based on the SEEBIC image of a single particle. Plots in panels (a) and (c) show the angular distributions of morphological chiral features for the NRs present in SEEBIC images. The plot in (b) shows the distribution of morphological chiral features with various inclination angles and distances from the helical axis of the NR. The orientation of the helical axis in panel (c) is indicated by a double-headed arrow. Scale bars are 50 nm.

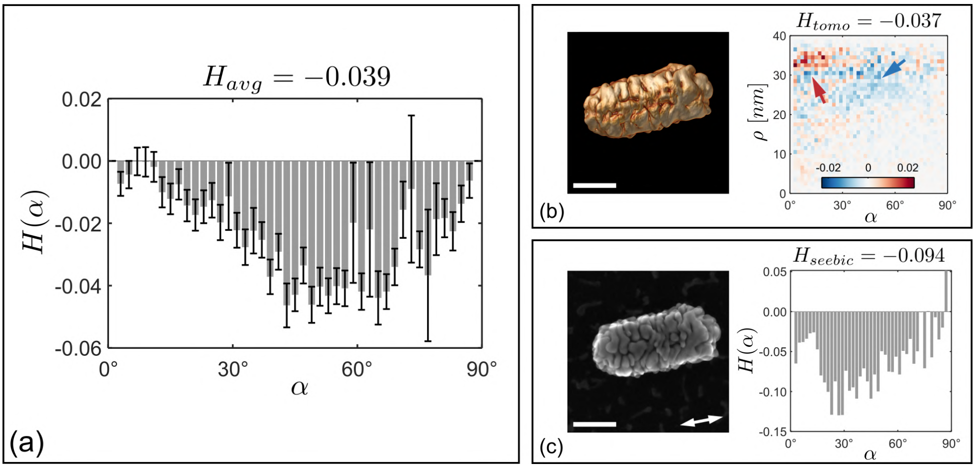

Figure 6.16: Results of chirality quantification for sample 3. (a) Helicity quantification of a NR ensemble based on twelve overview SEEBIC images; (b) Helicity analysis from an ET reconstruction; (c) Helicity analysis base d on the SEEBIC image of a single particle. Plots in panels (a) and (c) show the angular distributions of morphological chiral features for the NRs present in SEEBIC images. The plot in (b) shows the distribution of morphological chiral features with various inclination angles and distances from the helical axis of the NR. The orientation of the helical axis in panel (c) is indicated by a double-headed arrow. Scale bars are 50 nm.

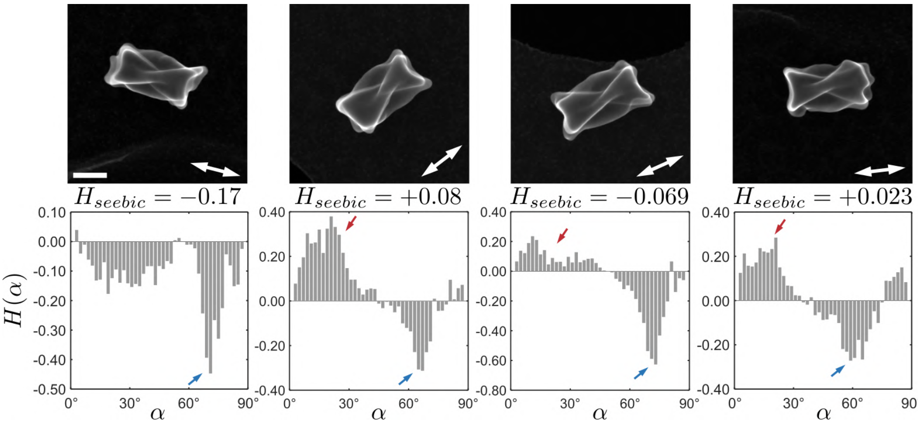

Figure 6.17: SEEBIC images of single NRs (sample 1) with the results of their quantification. The orientation of the helical axis in each SEEBIC image is indicated by a double-headed arrow. Scale bar is 50 nm.

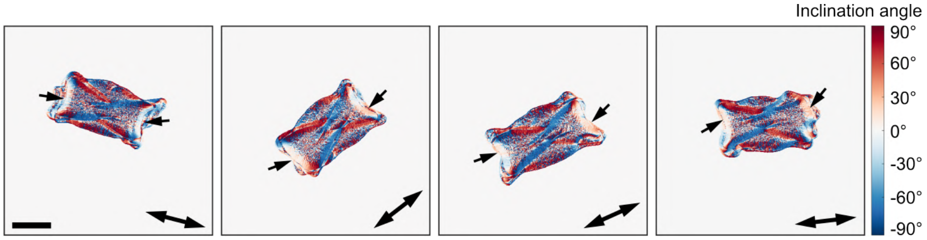

Figure 6.18: Coloured maps showing the distribution of inclination angles in SEEBIC images of single NRs (sample 1). Scale bar is 50 nm.

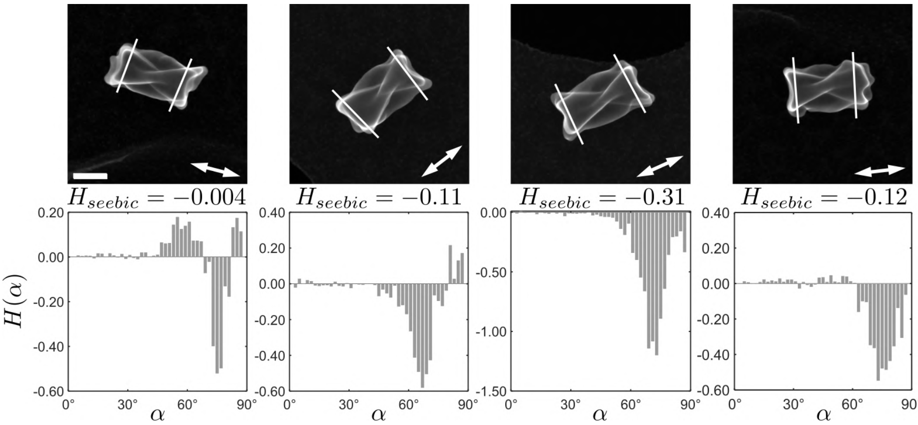

Figure 6.19: SEEBIC images of single NRs (sample 1) with the results of their quantification with artificially removed tips (as indicated by white lines in SEEBIC images). Scale bar is 50 nm.

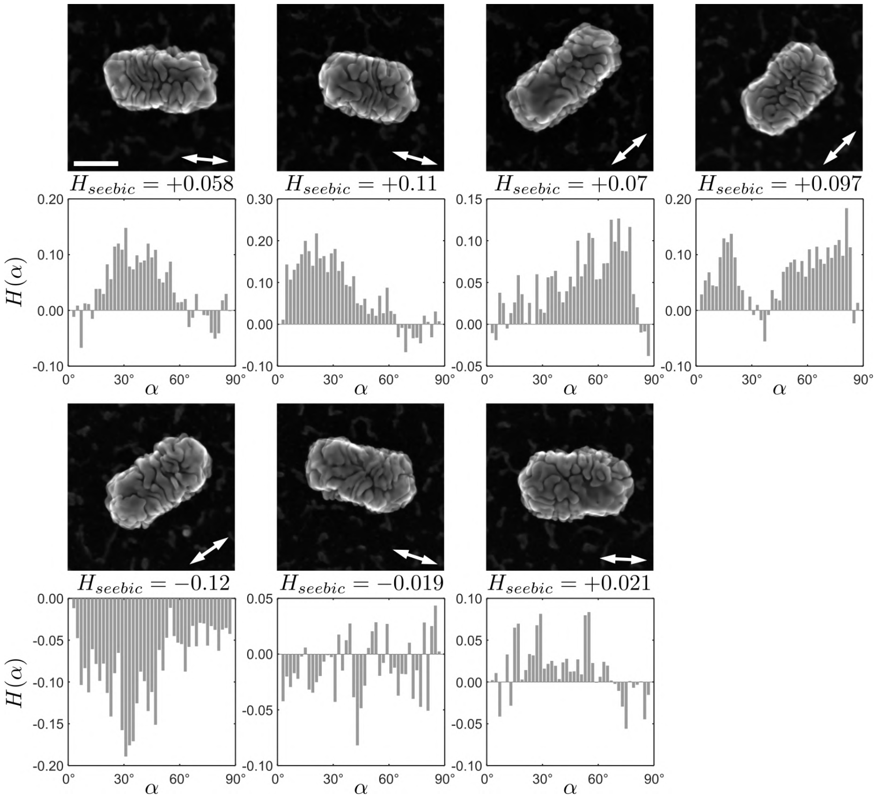

Figure 6.20: SEEBIC images of single NPs (sample 2) with the results of their quantification. Arbitrarily oriented NRs demonstrate a variety of morphologies and their contribution to the helicity function of the ensemble.The orientation of the helical axis in each SEEBIC image is indicated by a double-headed arrow. Scale bar is 50 nm.

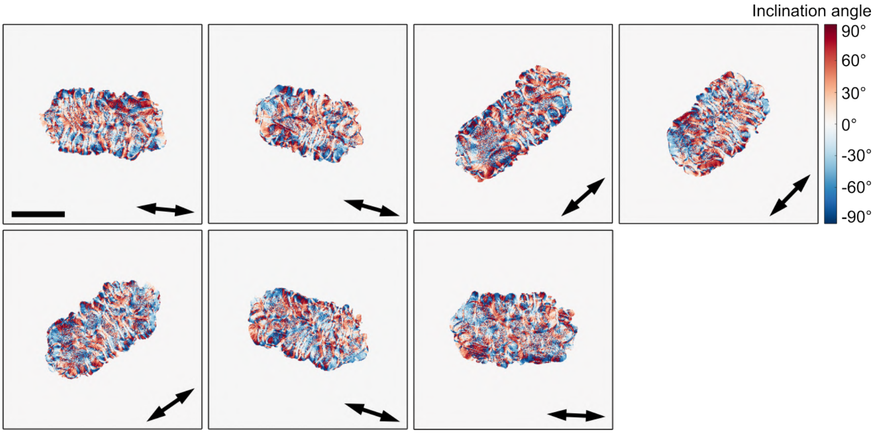

Figure 6.21: Coloured maps showing the distribution of inclination angles in SEEBIC images of single NRs (sample 2). Scale bar is 50 nm.

Despite the fact that quantification results for the average SEEBIC data and single-particle ET are globally matching, we find minor discrepancies in the positions and intensities of the peaks in the distributions. The observed difference can be understood in terms of morphological variations among individual particles. We thus conclude that individual ET reconstructions of single NRs are not always representative of the sample batch. This is not surprising because ET is indeed a very local technique, and this consideration is crucially important for a general understanding of the connection between structure and chiroptical properties. SEEBIC imaging is proposed as a route to overcome this limitation because the technique also enables local characterization, but at a higher throughput.

Although SEEBIC images are generally in good agreement with ET reconstructions, it is important to point out that inconsistencies may occur. For example, **Figure 6.22 a** shows mixed handedness compared to both ensemble-averaged SEEBIC (**Figure 6.14 a**) and ET data (**Figure 6.22 b**). Quantification results obtained from the SEEBIC image of a single NR in this case, show the presence of right-handed features with low inclination angles ($< 30°$) and very high inclination angles ($> 80°$), which are less obvious or even absent in quantification results based on ET. The right-handed morphological features in **Figure 6.22 a** have a contribution that is higher than the contribution of the left-handed features turning a positive total helicity value (H_{seebic}) that contradicts ensemble-averaged results (H_{avg}). In this case, the signature of the right-handed features is attributed to the contribution of the edges on NR tips (see **Figures 6.17 - 6.19**) and artifactual contrast due to the contribution of the backside of the NPs to the overall SEEBIC signal. It should be noted that the right-handed features appearing in SEEBIC images due to the contrast from the backside have little influence on average structure quantification because they are suppressed by a significantly higher contribution of the left-handed features, as shown by the high absolute value and low standard error at 70° in the ensemble plots (**Figure 6.14 a**).

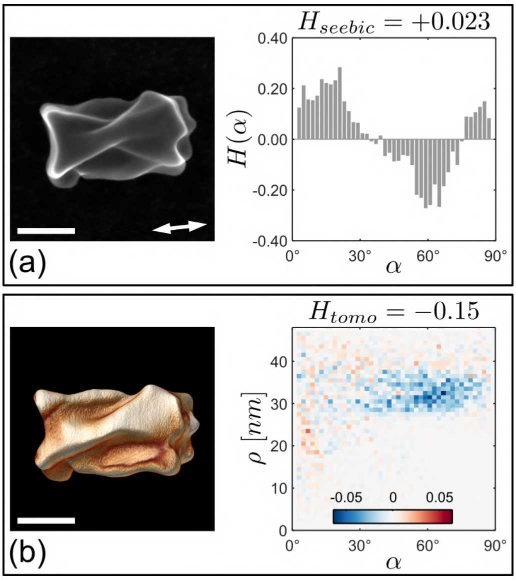

Figure 6.22: Results of helicity quantification for sample 1 showing the discrepancy between quantitative data obtained from (a) a single SEEBIC image and (b) ET reconstruction. The orientation of the helical axis in panel (a) is indicated by a double-headed arrow. Scale bars are 50 nm.

For sample 2, inconsistencies can also exceptionally be noted, e.g., when comparing **Figure 6.23 a** to **Figure 6.15 a** and **Figure 6.22 b**. In this case, the difference can be explained by a random distribution of nanoparticles on the support film, so that the top side of a specific NR has a predominant left-handed orientation, whereas the average NR morphology is right-handed. A volume render obtained from the ET reconstruction along the same viewing direction as the one for which the SEEBIC image was acquired, results in this NP visually appearing as a left-handed morphology (**Figure 6.24**). However, 3D renders from different orientations reveal predominantly right-handed morphologies (see **Figure 6.24**). The presence of features with different handedness corresponds to the idea that inorganic chiral NPs can yield a continuum of chiral features, which is in stark contrast to e.g., amino acids presenting binary chirality. It is thus important to acquire SEEBIC images or ET data sets from multiple NRs, to investigate the overall chirality coming from the ensemble of individual NRs in a given sample. The advantage of SEEBIC over ET is the possibility of acquiring the data with higher throughput. On the other hand, ET enables the investigation of the distribution of chiral features for entire NRs, whereas SEEBIC is currently only able to show the chiral morphology at the top surface. By combining HAADF-STEM and SEEBIC images of a given NR, it might be possible to extract a 3D mesh of the entire surface, but further work is required to reach this goal.

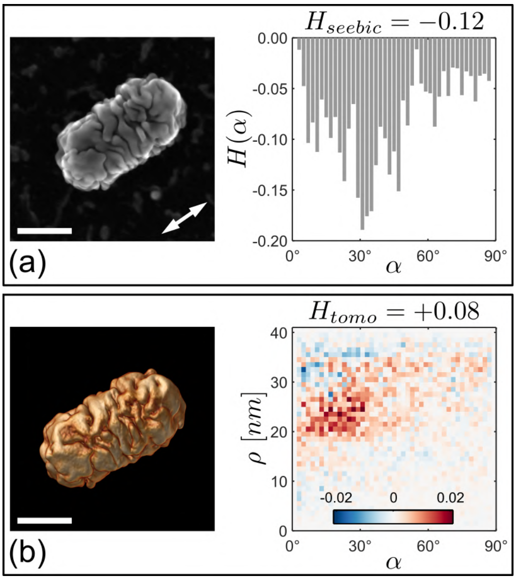

Figure 6.23: Results of helicity quantification for sample 2 showing the discrepancy between quantitative data obtained from (a) a single SEEBIC image and (b) ET reconstruction. The orientation of the helical axis in panel (a) is indicated by a double-headed arrow. Scale bars are 50 nm.

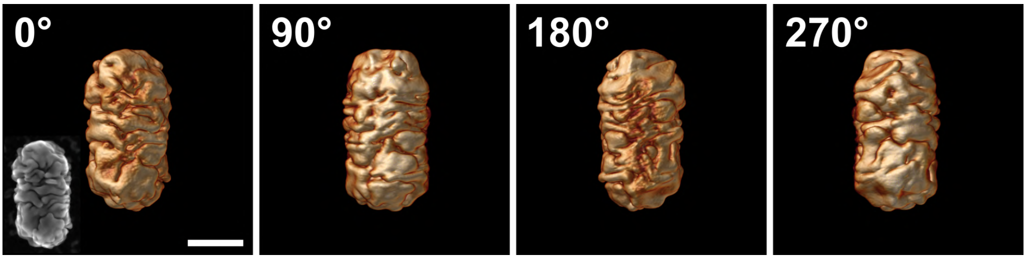

Figure 6.24: Electron tomography volume renders of a single NP corresponding to sample 2, obtained from different viewing directions. The inset shows a SEEBIC image corresponding to the 0° viewing direction. Scale bar is 50 nm.

We finally investigated how the variability in SEEBIC measurements at the single particle level affected the ensemble measurements. **Figure 6.25 a** (see **Figure 6.26** for the complete overview) shows arbitrarily oriented NRs with a variety of morphologies, which are representative of sample 2. The results of helicity quantification, based on these images, demonstrate that some NRs show chiral features that are characterized by low angles (30°), whereas others demonstrate opposite or even mixed handedness (**Figure 6.25 a**).

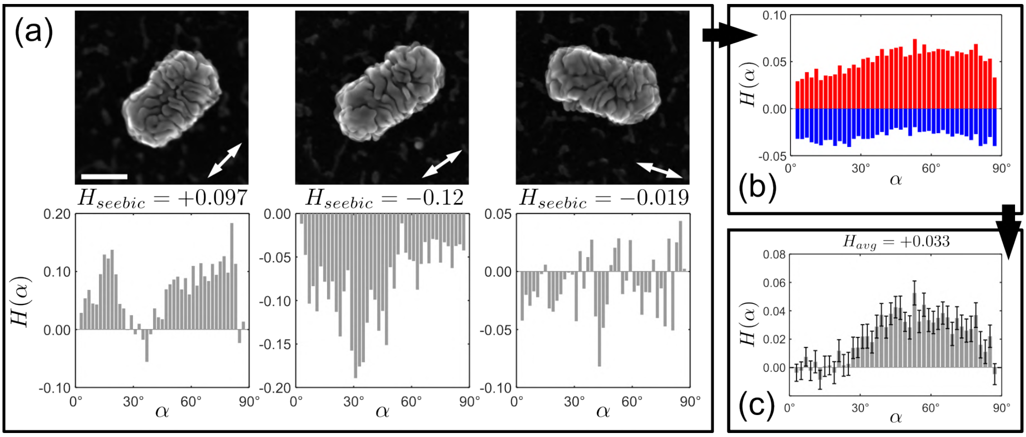

Figure 6.25: Illustration of how morphologies of single NRs translate to an average morphology of the ensemble for sample 2. (a) SEEBIC images of single NRs with the results of their quantification. (b) Results of helicity quantification of a NR ensemble, based on overview SEEBIC images for left-handed and right-handed features. Plots are encoded in colours: red for right-handed and blue for left-handed morphological features. (c) Helicity quantification of a NR ensemble, based on overview SEEBIC images with indicated standard error. The orientation of the helical axis in panel (a) is indicated by a double-headed arrow. Scale bar is 50 nm.

However, averaging arbitrarily oriented NRs over an ensemble (in this case comprising 174 NPs), results in cancelling low-angle features with opposite handedness (see **Figure 6.25 b**) leading to the distribution shown in **Figure 6.25 c**, where a high-angle (40-70°), right-handed morphology is predominant. It is likely that these high-angle features determine the optical properties measured by ensemble techniques (**Figure 6.13**). Plots showing a transition from the morphologies of single NRs to an average ensemble structure for samples 1 and 3 are provided in **Figure 6.17, 6.26 a, c and 6.27**. Our results show that, to fully retrieve information about both the average structure of a sample and the local NP morphology, and how these aspects are connected, a combination of multiple overview SEEBIC images and a few ET data sets will be required.

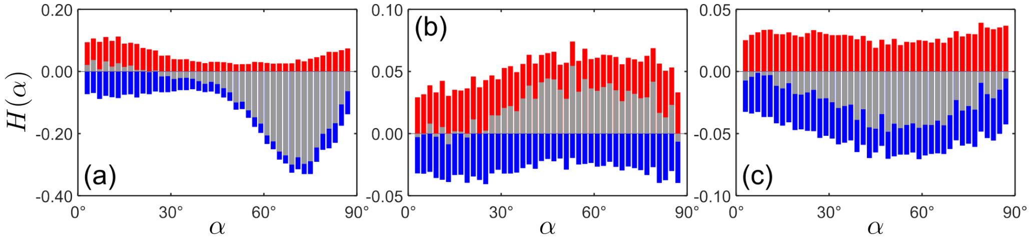

Figure 6.26: Results of chirality quantification of NR ensembles for (a) sample 1, (b) sample 2, and (c) sample 3, based on overview SEEBIC images. Plots are colour-coded: red for right-handed and blue for left-handed morphological features. Grey colour indicates the total helicity function.

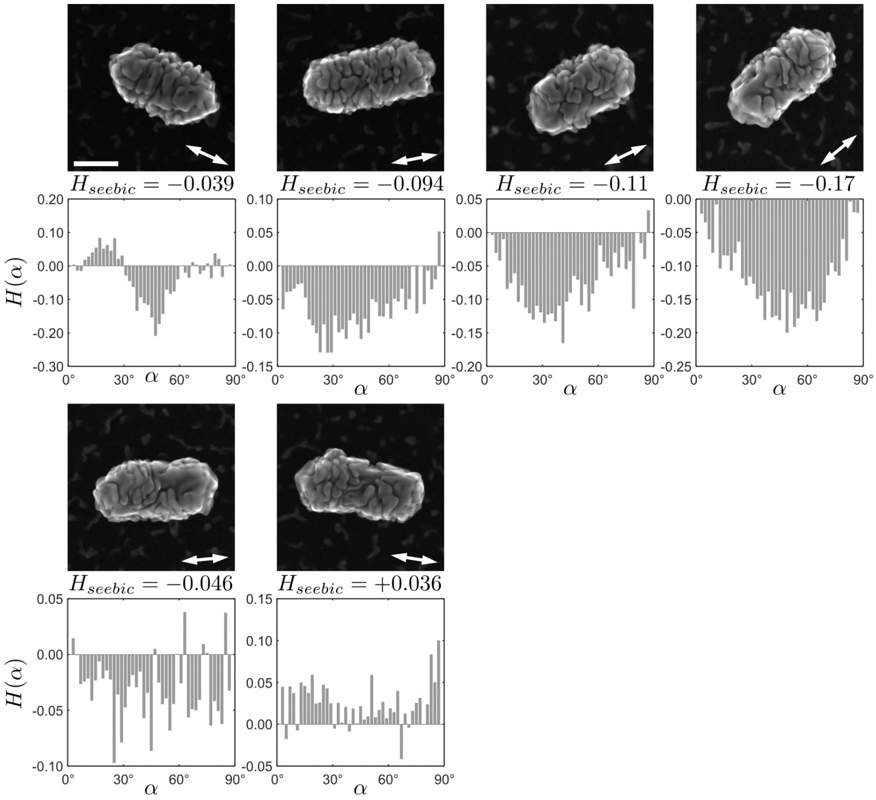

Figure 6.27: SEEBIC images of single NPs (sample 3) with the results of their quantification. Arbitrarily oriented NRs demonstrate a variety of morphologies and their contribution to the helicity function of the ensemble.The orientation of the helical axis in each SEEBIC image is indicated by a double-headed arrow. Scale bar is 50 nm.

6.6 Conclusions

We have shown that the helical morphology of chiral Au NRs, with significant polydispersity at the level of surface features (twists and wrinkles) can be efficiently quantified using high-throughput SEEBIC measurements. This approach overcomes the limitation of poor statistics obtained by ET, which is limited to analyzing only a few particles per sample batch because of long acquisition and processing times. By exploiting SEEBIC in combination with a dedicated quantification procedure to measure helicity, we were able to gain insights into the ensemble-level (chiral) characteristics of twisted and wrinkled nanoparticles within a timeframe of one experimental day. We found that the average helicity values, calculated for hundreds of NRs per sample batch were in good agreement with the optical properties of the sample, confirming that helicity measurements enable linking the nanoscale morphology with the chiroptical handedness. Further, we confirmed the robustness of the SEEBIC helicity quantification, showing that edge and backside effects are averaged out at the ensemble level. This accurate and statistically relevant morphological information combined with local characterization provides a route to connect ensemble properties to the morphologies of single NPs.

6.7 Experimental Images Used for Analysis

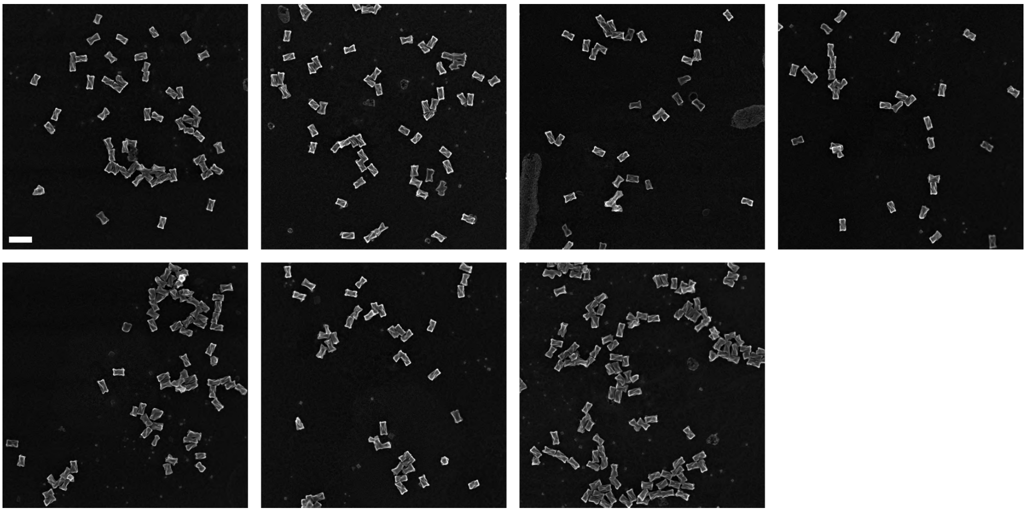

Figure 6.28: All acquired SEEBIC images for sample 1. Scale bar is 250 nm.

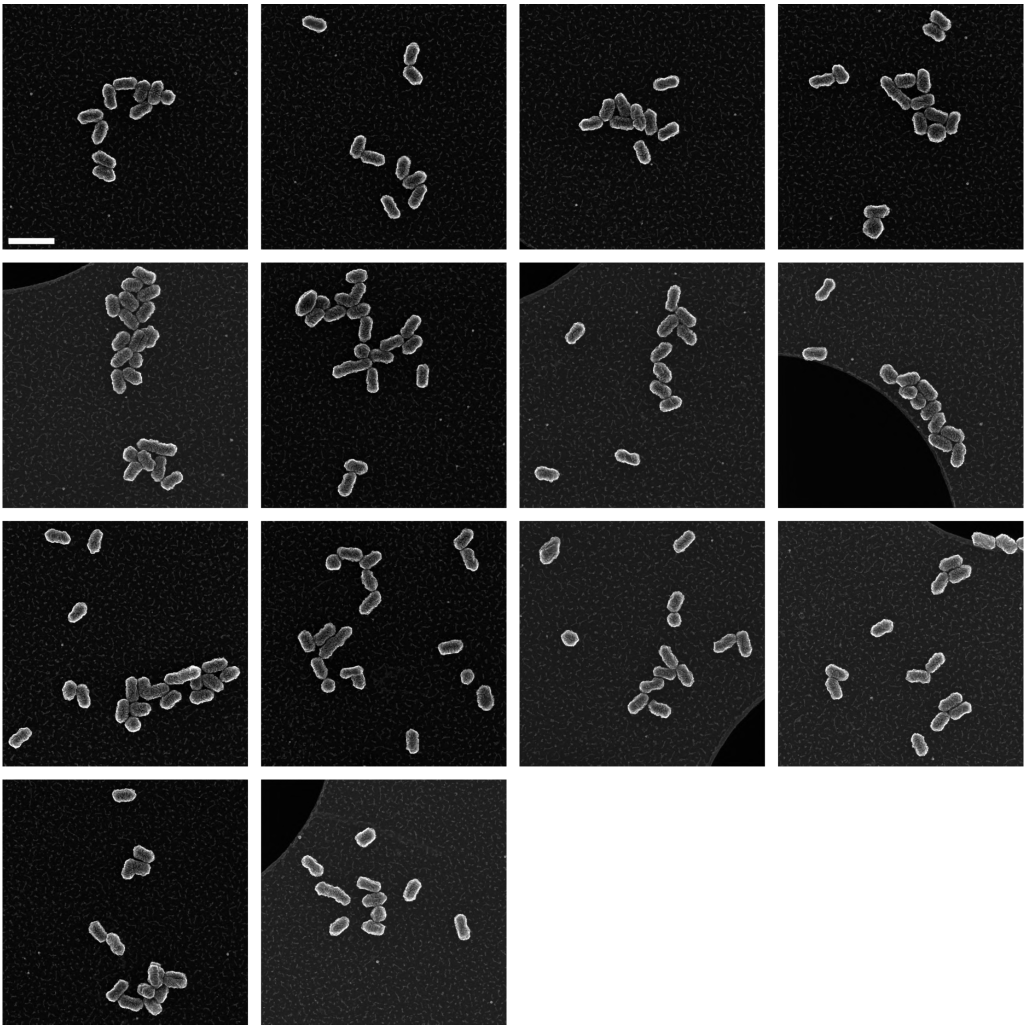

Figure 6.29: All acquired SEEBIC images for sample 2. Scale bar is 250 nm.

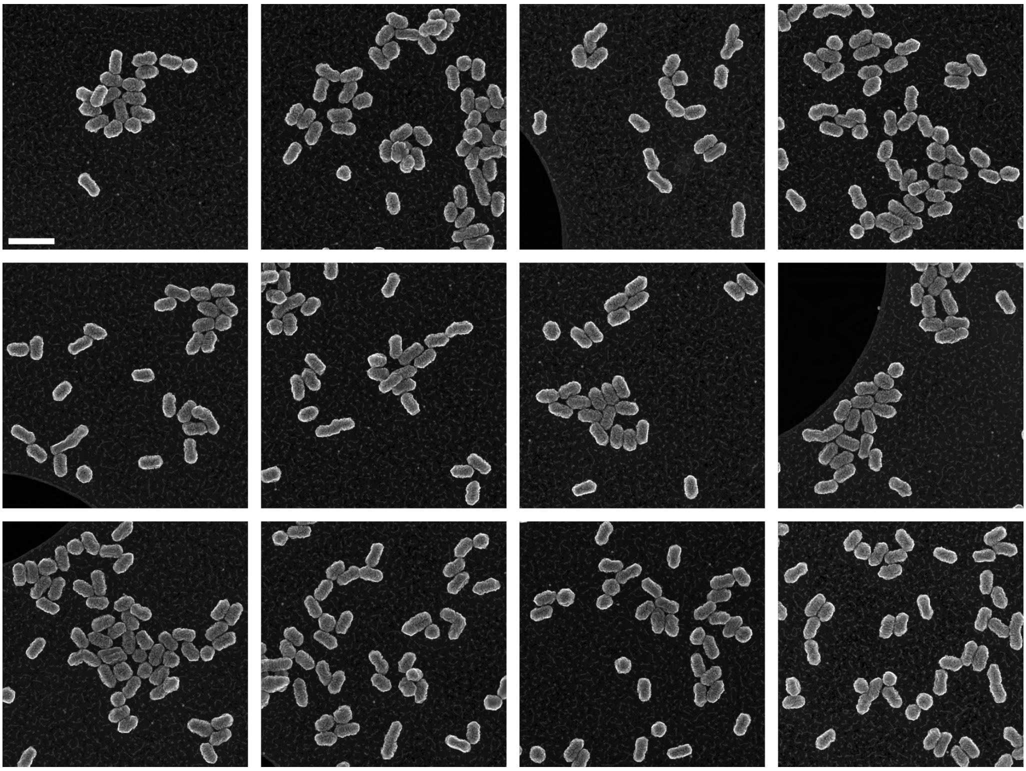

Figure 6.30: All acquired SEEBIC images for sample 1. Scale bar is 250 nm.

Chapter 7

General Conclusion

This chapter concludes this thesis by summarising the key research findings and discussing future perspectives for the presented research. It also demonstrates promising results that can motivate further exploration of this research field.

This PhD thesis was devoted to finding techniques for the characterization of the morphology of NPs that overcome the limitations of conventional ET. Here, SEEBIC was proposed as an alternative way for the visualization of the 3D structure of NPs with improved throughput and temporal resolution. To achieve this, an optimised SEEBIC setup, consisting of a custom-made TIA and PCB carrier board for the sample, was designed and characterized. The developed methodology and instrumentation allowed us to show that SEEBIC can be considered an attractive approach with shorter acquisition and processing times in comparison to ET and superior resolution in comparison to SEM. The contrast artifacts arising in SEEBIC images and their origin were unravelled. We discussed the importance of using a closed membrane to minimize imaging artifacts.

A physical model of SEEBIC topographical contrast formation that includes the angle-dependent escape rate of SEs and their contribution to the overall SEEBIC signal was proposed. This physical model was used to simulate SEEBIC images using synthetic 3D data or 3D data obtained from the ET experiment. It was shown that the proposed model is capable of replicating the SEEBIC image artifacts. It can further be used as an aid for the interpretation of SEEBIC images that are not always straightforward to interpret. Further improvements to the simulation workflow were proposed and discussed.

Next, it was shown that direct access to surface morphology obtainable on the order of minutes opens up the possibility of using SEEBIC for high-throughput analysis of the helical morphology of chiral Au NRs. The workflow to automatically quantify the helical morphology based on SEEBIC images and a dedicated image quantification procedure was developed and used to calculate the helicity function of the NP ensembles. Helicity function analysis revealed a significant polydispersity at the level of surface features. The results were compared with the quantification data obtained from single-particle ET reconstructions showing the advantages of the proposed quantification method for general understanding of the structure of the sample batch. Based on experimental observations and previous discussion, we propose a model of how morphologies of single NRs translate to an average morphology of the ensemble.

Chapter 8

Outlook

There are several directions for further development of the SEEBIC technique and its applications proposed in this thesis that remain to be explored. High-throughput capabilities of SEEBIC can be further expanded. For example, the algorithm used for helicity quantification can be adapted by introducing another measure for chirality rather than helicity function. This will allow to apply the algorithm to a broad range of chiral nanomaterials. Moreover, other geometrical descriptors can be introduced and quantified (e.g. roughness, porosity, pocketness, minimal accessible radius, etc.) with high statistical value.

Improved throughput and temporal resolution of SEEBIC imaging potentially can provide statistical analysis of the morphological changes occurring at elevated temperatures overcoming one of the limitations of *in situ* heating ET. Additionally, *in-situ* heating experiments could benefit from the use of SEEBIC for several reasons. First, if SEEBIC image acquisition is fast enough, there is no need to quench the sample in between the heating steps to "freeze" the structure for further imaging. Second, the sensitivity of SEEBIC to temperature variations can also be used to map inhomogeneities of temperature over the region of interest. However, the implementation of the heating experiment requires a dedicated system that allows simultaneous heating and SEEBIC measurements.

It should be noted that SEEBIC images (as conventional SEM images) provide a pseudo-3D perception of the object and resemble reflected light images. However, using state-of-the-art computer vision techniques, the real 3D information from sets of 2D images can be obtained. These techniques were adapted for SEM for the reconstruction of the surface morphology and potentially can be used for SEEBIC imaging. The reconstruction techniques can be divided into several groups: (1) single-view, (2) multiple-view, (3) hybrid, and (4) other approaches [92].

The single-view reconstruction techniques use 2D images from a single viewpoint with varying light directions to retrieve 3D information. The main algorithm of the single-view approach in SEM is shape-from-shading (SfS). The method is based on Lambert's angular distribution of BSEs and SEs. The implementation of this technique requires a set of detectors symmetrically arranged around the primary electron beam [92]. The combination of the signals from these detectors enables the estimation of the local surface inclinations (gradient) along the scanning line. The height map is processed by the integration of these gradient fields. In the case of SEEBIC, a similar effect could be obtained with an applied electric field surrounding the NPs which can be changed in magnitude or direction. The SfS technique can also be implemented to reconstruct the 3D surface morphology by analyzing the grayscale information of a single top-view SEM image [131].

The multi-view approach uses a set of 2D images (2 or more), where images are taken by tilting the specimen. The method is based on the theory of projective geometry, using different perspectives from different view angles to reconstruct the 3D structure. The stereo vision [132], and structure-from-motion (SfM) [133] algorithms are computational techniques that use pixels or feature-points matching to retrieve 3D information [134]. In traditional stereo vision, two cameras displaced from each other are used to obtain two different views of a scene similar to human vision. By comparing images from these cameras, the depth information can be obtained in the form of a disparity map, which encodes the difference in horizontal coordinates of corresponding image points. The values in this disparity map are proportional to the scene depth (heights in the third dimension). The SfM approach uses corresponding feature point detection in stereo pairs and their matching to reconstruct 3D structures by triangulation [134]. Both of the methods were successfully implemented in SEM [92].

The hybrid approach utilizes the advantages of both single- and multi-view 3D reconstruction techniques. The shading provides the best reconstruction results for homogeneous surfaces, while stereo techniques suit better for surfaces with a large number of features [92].

In this work, we attempted the SfM approach to reconstruct the surface of Au decahedral NP (**Figure 8.1**). The tilt series of 11 images were acquired (from -10° to +10°, increment of 2°). It was shown that the used algorithms are not efficient for 3D reconstructions based on SEEBIC data which requires further investigations. The efficiency can possibly be improved by increasing the number of input images or using advanced or hybrid algorithms for the detection and tracking of the feature points. Further implementation of this technique with SEEBIC would greatly benefit from a higher bandwidth TIA to reduce the time to acquire multiple images.

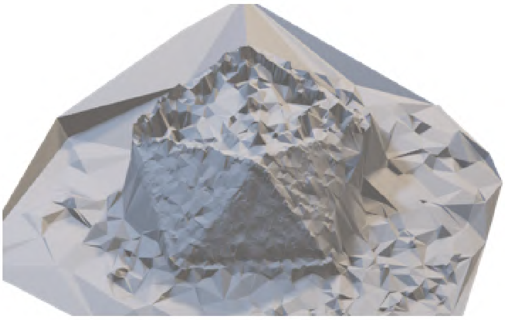

Figure 8.1: Structure-from-motion reconstruction of the surface of Au decahedral NP based on 11 SEEBIC images.

Another direction for innovation is the use of novel advanced algorithms of computer vision NeRF (Neural Radiance Fields) [135] and Plenoxels (Radiance Fields without Neural Networks) [136]. NeRF uses deep learning to model the volumetric scene for constructing a 3D scene from a set of 2D images. The core idea is to represent a scene as a continuous function that maps a 3D coordinate and a viewing direction to a colour and a density. This representation allows for high-quality rendering of complex scenes with realistic light and shadow effects. Plenoxels is another approach to rendering and understanding 3D scenes, but it does not rely on neural networks like NeRF. Instead, it uses a structure that is more direct and less computationally intensive. Plenoxels represent a scene using a grid of voxels, where each voxel stores information about light's behaviour at that point, such as colour and opacity. This allows for efficient rendering and editing of 3D scenes. Compared to NeRF, Plenoxels can be faster and require less computational resources, making them more accessible for real-time applications.

Bibliography

(1) Hornyak, G. L.; Tibbals, H.; Dutta, J.; Moore, J. J., *Introduction to Nanoscience and Nanotechnology*, 1st ed.; CRC Press: 2008.

(2) Hubenthal, F. In *Comprehensive Nanoscience and Technology*, Andrews, D. L., Scholes, G. D., Wiederrecht, G. P., Eds.; Academic Press: Amsterdam, 2011, pp 375–435.

(3) Wu, B.; Kumar, A. Extreme ultraviolet lithography: A review. *J. Vac. Sci. Technol. B* **2007**, *25*, 1743–1761.

(4) Chen, Y. Nanofabrication by electron beam lithography and its applications: A review. *Microelectron. Eng.* **2015**, *135*, 57–72.

(5) Yu, H.-D.; Regulacio, M. D.; Ye, E.; Han, M.-Y. Chemical routes to top-down nanofabrication. *Chem. Soc. Rev.* **2013**, *42*, 6006–6018.

(6) Li, P.; Chen, S.; Dai, H.; Yang, Z.; Chen, Z.; Wang, Y.; Chen, Y.; Peng, W.; Shan, W.; Duan, H. Recent advances in focused ion beam nanofabrication for nanostructures and devices: fundamentals and applications. *Nanoscale* **2021**, *13*, 1529–1565.

(7) Cushing, B. L.; Kolesnichenko, V. L.; O'Connor, C. J. Recent Advances in the Liquid-Phase Syntheses of Inorganic Nanoparticles. *Chem. Rev.* **2004**, *104*, 3893–3946.

(8) Heuer-Jungemann, A. et al. The Role of Ligands in the Chemical Synthesis and Applications of Inorganic Nanoparticles. *Chem. Rev.* **2019**, *119*, 4819–4880.

(9) Kravets, V. G.; Kabashin, A. V.; Barnes, W. L.; Grigorenko, A. N. Plasmonic Surface Lattice Resonances: A Review of Properties and Applications. *Chem. Rev.* **2018**, *118*, 5912–5951.

(10) Ai, B.; Fan, Z.; Wong, Z. J. Plasmonic–perovskite solar cells, light emitters, and sensors. *Microsyst. Nanoeng.* **2022**, *8*, 1–28.

(11) Sharifi, M.; Attar, F.; Saboury, A. A.; Akhtari, K.; Hooshmand, N.; Hasan, A.; El-Sayed, M. A.; Falahati, M. Plasmonic gold nanoparticles: Optical manipulation, imaging, drug delivery and therapy. *J. Control. Release* **2019**, *311-312*, 170–189.

(12) Mitchell, M. J.; Billingsley, M. M.; Haley, R. M.; Wechsler, M. E.; Peppas, N. A.; Langer, R. Engineering precision nanoparticles for drug delivery. *Nat. Rev. Drug. Discov.* **2021**, *20*, 101–124.

(13) Amirjani, A.; Amlashi, N. B.; Ahmadiani, Z. S. Plasmon-Enhanced Photocatalysis Based on Plasmonic Nanoparticles for Energy and Environmental Solutions: A Review. *ACS Appl. Nano Mater.* **2023**, *6*, 9085–9123.

(14) Grzelczak, M.; Pérez-Juste, J.; Mulvaney, P.; Liz-Marzán, L. M. Shape control in gold nanoparticle synthesis. *Chem. Soc. Rev.* **2008**, *37*, 1783–1791.

(15) Linic, S.; Christopher, P.; Ingram, D. B. Plasmonic-metal nanostructures for efficient conversion of solar to chemical energy. *Nature Mater.* **2011**, *10*, 911–921.

(16) Wang, F.; Yue, X.; Ding, Q.; Lin, H.; Xu, C.; Li, S. Chiral inorganic nanomaterials for biological applications. *Nanoscale* **2023**, *15*, 2541–2552.

(17) Williams, D. B.; Carter, C. B., *Transmission Electron Microscopy*; Springer US: Boston, MA, 2009.

(18) Ruska, E. The development of the electron microscope and of electron microscopy. *Biosci. Rep.* **1987**, *7*, 607–629.

(19) Reifsnyder Hickey, D.; Mkhoyan, K. A. Atomic-resolution analytical scanning transmission electron microscopy of topological insulators with a layered tetradymite structure. *APL Mater.* **2020**, *8*, 070902.

(20) Shindo, D.; Oikawa, T. In *Analytical Electron Microscopy for Materials Science*, Shindo, D., Oikawa, T., Eds.; Springer Japan: Tokyo, 2002, pp 81–102.

(21) Egerton, R., *Electron Energy-Loss Spectroscopy in the Electron Microscope*; Springer US: Boston, MA, 2011.

(22) Electron energy loss spectroscopy - Wikipedia, `https://en.wikipedia.org/wiki/Electron_energy_loss_spectroscopy`.

(23) Reimer, L., *Scanning Electron Microscopy: Physics of Image Formation and Microanalysis*; Hawkes, P. W., Lotsch, H. K. V., Eds.; Springer Series in Optical Sciences, Vol. 45; Springer Berlin Heidelberg: Berlin, Heidelberg, 1998.

(24) Scanning electron microscope - Wikipedia, `https://en.wikipedia.org/wiki/Scanning_electron_microscope`.

(25) Van Aarle, W.; Palenstijn, W. J.; De Beenhouwer, J.; Altantzis, T.; Bals, S.; Batenburg, K. J.; Sijbers, J. The ASTRA Toolbox: A platform for advanced algorithm development in electron tomography. *Ultramicroscopy* **2015**, *157*, 35–47.

(26) Weyland, M.; Midgley, P. A. In *Nanocharacterisation*, Kirkland, A. I., Haigh, S. J., Eds., 2nd ed.; The Royal Society of Chemistry: 2015, pp 211–299.

(27) Fitchard, E. E.; Aldridge, J. S.; Reckwerdt, P. J.; Mackie, T. R. Registration of synthetic tomographic projection data sets using cross-correlation. *Phys. Med. Biol.* **1998**, *43*, 1645.

(28) Gilbert, P. Iterative methods for the three-dimensional reconstruction of an object from projections. *J. Theor. Biol.* **1972**, *36*, 105–117.

(29) Shepp, L. A.; Vardi, Y. Maximum Likelihood Reconstruction for Emission Tomography. *IEEE Trans. Med. Imaging* **1982**, *1*, 113–122.

(30) Batenburg, K. J.; Bals, S.; Sijbers, J.; Kübel, C.; Midgley, P. A.; Hernandez, J. C.; Kaiser, U.; Encina, E. R.; Coronado, E. A.; Van Tendeloo, G. 3D imaging of nanomaterials by discrete tomography. *Ultramicroscopy* **2009**, *109*, 730–740.

(31) Goris, B.; Van den Broek, W.; Batenburg, K. J.; Heidari Mezerji, H.; Bals, S. Electron tomography based on a total variation minimization reconstruction technique. *Ultramicroscopy* **2012**, *113*, 120–130.

(32) Midgley, P. A.; Weyland, M.; Thomas, J. M.; Johnson, B. F. G. Z-Contrast tomography: a technique in three-dimensional nanostructural analysis based on Rutherford scattering. *Chem. Commun.* **2001**, 907–908.

(33) Midgley, P. A.; Weyland, M. 3D electron microscopy in the physical sciences: the development of Z-contrast and EFTEM tomography. *Ultramicroscopy* **2003**, *96*, 413–431.

(34) Bals, S.; Van Tendeloo, G.; Kisielowski, C. A New Approach for Electron Tomography: Annular Dark-Field Transmission Electron Microscopy. *Adv. Mater.* **2006**, *18*, 892–895.

(35) Midgley, P. A.; Dunin-Borkowski, R. E. Electron tomography and holography in materials science. *Nature Mater.* **2009**, *8*, 271–280.

(36) Bals, S.; Casavola, M.; van Huis, M. A.; Van Aert, S.; Batenburg, K. J.; Van Tendeloo, G.; Vanmaekelbergh, D. Three-Dimensional Atomic Imaging of Colloidal Core–Shell Nanocrystals. *Nano Lett.* **2011**, *11*, 3420–3424.

(37) Goris, B.; Bals, S.; Van den Broek, W.; Carbó-Argibay, E.; Gómez-Graña, S.; Liz-Marzán, L. M.; Van Tendeloo, G. Atomic-scale determination of surface facets in gold nanorods. *Nature Mater.* **2012**, *11*, 930–935.

(38) Bals, S.; Goris, B.; Liz-Marzán, L. M.; Van Tendeloo, G. Three-Dimensional Characterization of Noble-Metal Nanoparticles and their Assemblies by Electron Tomography. *Angew. Chem. Int. Ed.* **2014**, *53*, 10600–10610.

(39) Miao, J.; Ercius, P.; Billinge, S. J. L. Atomic electron tomography: 3D structures without crystals. *Science* **2016**, *353*, aaf2157.

(40) Goris, B.; De Beenhouwer, J.; De Backer, A.; Zanaga, D.; Batenburg, K. J.; Sánchez-Iglesias, A.; Liz-Marzán, L. M.; Van Aert, S.; Bals, S.; Sijbers, J.; Van Tendeloo, G. Measuring Lattice Strain in Three Dimensions through Electron Microscopy. *Nano Lett.* **2015**, *15*, 6996–7001.

(41) RealNANO ERC Consolidator project, `http://realnano.uantwerpen.be/`.

(42) Vanrompay, H.; Bladt, E.; Albrecht, W.; Béché, A.; Zakhozheva, M.; Sánchez-Iglesias, A.; Liz-Marzán, L. M.; Bals, S. 3D characterization of heat-induced morphological changes of Au nanostars by fast in situ electron tomography. *Nanoscale* **2018**, *10*, 22792–22801.

(43) Albrecht, W.; Bals, S. Fast Electron Tomography for Nanomaterials. *J. Phys. Chem. C* **2020**, *124*, 27276–27286.

(44) Vanrompay, H.; Skorikov, A.; Bladt, E.; Béché, A.; Freitag, B.; Verbeeck, J.; Bals, S. Fast versus conventional HAADF-STEM tomography of nanoparticles: advantages and challenges. *Ultramicroscopy* **2021**, *221*, 113191.

(45) Albrecht, W.; Bladt, E.; Vanrompay, H.; Smith, J. D.; Skrabalak, S. E.; Bals, S. Thermal Stability of Gold/Palladium Octopods Studied in Situ in 3D: Understanding Design Rules for Thermally Stable Metal Nanoparticles. *ACS Nano* **2019**, *13*, 6522–6530.

(46) Skorikov, A.; Albrecht, W.; Bladt, E.; Xie, X.; van der Hoeven, J. E. S.; van Blaaderen, A.; Van Aert, S.; Bals, S. Quantitative 3D Characterization of Elemental Diffusion Dynamics in Individual Ag@Au Nanoparticles with Different Shapes. *ACS Nano* **2019**, *13*, 13421–13429.

(47) Niu, W.; Xu, G. Crystallographic control of noble metal nanocrystals. *Nano Today* **2011**, *6*, 265–285.

(48) Li, Y.; Somorjai, G. A. Nanoscale Advances in Catalysis and Energy Applications. *Nano Lett.* **2010**, *10*, 2289–2295.

(49) Sepúlveda, B.; Angelomé, P. C.; Lechuga, L. M.; Liz-Marzán, L. M. LSPR-based nanobiosensors. *Nano Today* **2009**, *4*, 244–251.

(50) Atwater, H. A.; Polman, A. Plasmonics for improved photovoltaic devices. *Nature Mater.* **2010**, *9*, 205–213.

(51) Jain, P. K.; El-Sayed, I. H.; El-Sayed, M. A. Au nanoparticles target cancer. *Nano Today* **2007**, *2*, 18–29.

(52) Allen, R. M. Secondary electron imaging as an aid to STEM microanalysis. *Ultramicroscopy* **1982**, *10*, 237–245.

(53) Imeson, D.; Milne, R. H.; Berger, S. D.; McMullan, D. Secondary electron detection in the scanning transmission electron microscope. *Ultramicroscopy* **1985**, *17*, 243–249.

(54) Bleloch, A. L.; Howie, A.; Milne, R. H. High resolution secondary electron imaging and spectroscopy. *Ultramicroscopy* **1989**, *31*, 99–110.

(55) Liu, J.; Cowley, J. M. Imaging with high-angle scattered electrons and secondary electrons in the STEM. *Ultramicroscopy* **1991**, *37*, 50–71.

(56) Howie, A. Recent developments in secondary electron imaging. *J. Microsc.* **1995**, *180*, 192–203.

(57) Liu, J. Scanning transmission electron microscopy and its application to the study of nanoparticles and nanoparticle systems. *J. Electron Microsc.* **2005**, *54*, 251–278.

(58) Mitchell, D. R. G.; Casillas, G. Secondary Electron Imaging in an Aberration-Corrected STEM. *Microsc. Today* **2016**, *24*, 22–27.

(59) Zhu, Y.; Inada, H.; Nakamura, K.; Wall, J. Imaging single atoms using secondary electrons with an aberration-corrected electron microscope. *Nature Mater.* **2009**, *8*, 808–812.

(60) Inada, H.; Su, D.; Egerton, R. F.; Konno, M.; Wu, L.; Ciston, J.; Wall, J.; Zhu, Y. Atomic imaging using secondary electrons in a scanning transmission electron microscope: Experimental observations and possible mechanisms. *Ultramicroscopy* **2011**, *111*, 865–876.

(61) Wu, L.; Egerton, R. F.; Zhu, Y. Image simulation for atomic resolution secondary electron image. *Ultramicroscopy* **2012**, *123*, 66–73.

(62) Brown, H. G.; D'Alfonso, A. J.; Allen, L. J. Secondary electron imaging at atomic resolution using a focused coherent electron probe. *Phys. Rev. B* **2013**, *87*, 054102.

(63) Howe, J. Y.; Allard, L. F.; Bigelow, W. C.; Demers, H.; Overbury, S. H. Understanding catalyst behavior during in situ heating through simultaneous secondary and transmitted electron imaging. *Nanoscale Res. Lett.* **2014**, *9*, 614.

(64) Dyck, O.; Swett, J. L.; Evangeli, C.; Lupini, A. R.; Mol, J.; Jesse, S. Contrast Mechanisms in Secondary Electron e-Beam-Induced Current (SEEBIC) Imaging. *Microsc. Microanal.* **2022**, *28*, 1567–1583.

(65) Hubbard, W. A.; Mecklenburg, M.; Chan, H. L.; Regan, B. C. STEM Imaging with Beam-Induced Hole and Secondary Electron Currents. *Phys. Rev. Appl.* **2018**, *10*, 044066.

(66) Everhart, T.; Wells, O.; Matta, R. A novel method of semiconductor device measurements. *Proc. IEEE* **1964**, *52*, 1642–1647.

(67) Mecklenburg, M.; Hubbard, W. A.; Lodico, J. J.; Regan, B. C. Electron beam-induced current imaging with two-angstrom resolution. *Ultramicroscopy* **2019**, *207*, 112852.

(68) Hubbard, W. A.; Lingley, Z.; Theiss, J.; Sitzman, S.; Ayvazian, T.; Brodie, M.; Foran, B. Scanning transmission electron microscope mapping of electronic transport in polycrystalline BaTiO3 ceramic capacitors. *Appl. Phys. Lett.* **2019**, *115*, 133502.

(69) Hubbard, W. A.; Lodico, J. J.; Chan, H. L.; Mecklenburg, M.; Regan, B. C. Imaging Dielectric Breakdown in Valence Change Memory. *Adv. Funct. Mater.* **2022**, *32*, 2102313.

(70) Recalde-Benitez, O.; Jiang, T.; Winkler, R.; Ruan, Y.; Zintler, A.; Adabifiroozjaei, E.; Arzumanov, A.; Hubbard, W. A.; van Omme, T.; Pivak, Y.; Perez-Garza, H. H.; Regan, B. C.; Alff, L.; Komissinskiy, P.; Molina-Luna, L. Operando two-terminal devices inside a transmission electron microscope. *Commun. Eng.* **2023**, *2*, 1–8.

(71) Dyck, O.; Swett, J. L.; Lupini, A. R.; Mol, J. A.; Jesse, S. Imaging Secondary Electron Emission from a Single Atomic Layer. *Small Methods* **2021**, *5*, 2000950.

(72) Dyck, O.; Swett, J. L.; Evangeli, C.; Lupini, A. R.; Mol, J. A.; Jesse, S. Mapping Conductance and Switching Behavior of Graphene Devices In Situ. *Small Methods* **2022**, *6*, 2101245.

(73) Dyck, O.; Almutlaq, J.; Lingerfelt, D.; Swett, J. L.; Oxley, M. P.; Huang, B.; Lupini, A. R.; Englund, D.; Jesse, S. Direct imaging of electron density with a scanning transmission electron microscope. *Nature Commun.* **2023**, *14*, 7550.

(74) Hubbard, W.; Mecklenburg, M.; Regan, B. C. STEM EBIC Thermometry Calibration with PEET on Al Nanoparticles. *Microsc. Microanal.* **2020**, *26*, 3124–3125.

(75) Mecklenburg, M.; Hubbard, W. A.; Chan, H. L.; Regan, B. C. Adjusting the STEM sample holder potential for improved EBIC contrast. *Microsc. Microanal.* **2019**, *25*, 2354–2355.

(76) Rodríguez-Manzo, J. A.; Qi, Z. J.; Crook, A.; Ahn, J.-H.; Johnson, A. T. C.; Drndić, M. In Situ Transmission Electron Microscopy Modulation of Transport in Graphene Nanoribbons. *ACS Nano* **2016**, *10*, 4004–4010.

(77) Masih Das, P.; Drndić, M. In Situ 2D MoS2 Field-Effect Transistors with an Electron Beam Gate. *ACS Nano* **2020**, *14*, 7389–7397.

(78) Pivak, Y.; Perez-Garza, H. H.; Zintler, A.; Molina-Luna, L. In ASM International: 2017, pp 353–357.

(79) Han, C. W.; Ortalan, V. Secondary signal imaging (SSI) electron tomography (SSI-ET): A new three-dimensional metrology for mesoscale specimens in transmission electron microscope. *Micron* **2015**, *76*, 62–67.

(80) Graeme, J. G., *Photodiode amplifiers: op amp solutions*; McGraw-Hill: Boston, Mass., 1996.

(81) Asadi, F., *Essential Circuit Analysis using LTspice®*; Springer International Publishing: Cham, 2023.

(82) Hobbs, P. C. D., *Building Electro-Optical Systems: Making It all Work*, 2nd edition; Wiley: Hoboken, NJ, 2009.

(83) Lyman, C. 2023 Microscopy Today Innovation Awards. *Microscopy Today* **2023**, *31*, 12–16.

(84) 500MHz Ultra-Low Bias Current FET Input Op Amp, LTC6268; Analog Devices, 2017.

(85) Tao, A. R.; Habas, S.; Yang, P. Shape Control of Colloidal Metal Nanocrystals. *Small* **2008**, *4*, 310–325.

(86) Ino, S. Stability of Multiply-Twinned Particles. *J. Phys. Soc. Jpn.* **1969**, *27*, 941–953.

(87) Sánchez-Iglesias, A.; Winckelmans, N.; Altantzis, T.; Bals, S.; Grzelczak, M.; Liz-Marzán, L. M. High-Yield Seeded Growth of Monodisperse Pentatwinned Gold Nanoparticles through Thermally Induced Seed Twinning. *J. Am. Chem. Soc.* **2017**, *139*, 107–110.

(88) Scarabelli, L.; Coronado-Puchau, M.; Giner-Casares, J. J.; Langer, J.; Liz-Marzán, L. M. Monodisperse Gold Nanotriangles: Size Control, Large-Scale Self-Assembly, and Performance in Surface-Enhanced Raman Scattering. *ACS Nano* **2014**, *8*, 5833–5842.

(89) Ziaja, B.; van der Spoel, D.; Szöke, A.; Hajdu, J. Auger-electron cascades in diamond and amorphous carbon. *Phys. Rev. B* **2001**, *64*, 214104.

(90) Bailey, G.; Dimlich, R.; Alexander, K.; McCarthy, J.; Pretlow, T.; Zaluzec, N. J.; Kestel, B. J.; Henriks, D. Reactive Gas Plasma Specimen Processing for Use in Microanalysis and Imaging in Analytical Electron Microscopy. *Microsc. Microanal.* **1997**, *3*, 983–984.

(91) Winckelmans, N.; Altantzis, T.; Grzelczak, M.; Sánchez-Iglesias, A.; Liz-Marzán, L. M.; Bals, S. Multimode Electron Tomography as a Tool to Characterize the Internal Structure and Morphology of Gold Nanoparticles. *J. Phys. Chem. C* **2018**, *122*, 13522–13528.

(92) Tafti, A. P.; Kirkpatrick, A. B.; Alavi, Z.; Owen, H. A.; Yu, Z. Recent advances in 3D SEM surface reconstruction. *Micron* **2015**, *78*, 54–66.

(93) Heidari Mezerji, H.; Van den Broek, W.; Bals, S. A practical method to determine the effective resolution in incoherent experimental electron tomography. *Ultramicroscopy* **2011**, *111*, 330–336.

(94) Aschwanden, M. In *Self-Organized Criticality in Astrophysics: The Statistics of Nonlinear Processes in the Universe*, Aschwanden, M., Ed.; Springer Praxis Books; Springer: Berlin, Heidelberg, 2011, pp 83–110.

(95) Lin, Y.; Joy, D. C. A new examination of secondary electron yield data. *Surf. Interface Anal.* **2005**, *37*, 895–900.

(96) Hubbard, W. A.; Chan, H. L.; Mecklenburg, M.; Regan, B. C. Separation of EBIC Modes with Two-Channel STEM EBIC. *Microsc. Microanal.* **2022**, *28*, 2508–2509.

(97) Joy, D. C.; Joy, D. C., *Monte Carlo Modeling for Electron Microscopy and Microanalysis*; Oxford Series in Optical and Imaging Sciences; Oxford University Press: Oxford, New York, 1995.

(98) Babin, S.; Borisov, S. S.; Ito, H.; Ivanchikov, A.; Suzuki, M. Simulation of scanning electron microscope images taking into account local and global electromagnetic fields. *J. Vac. Sci. Technol. B* **2010**, *28*, C6C41–C6C47.

(99) Poirier-Demers, N.; Demers, H.; Drouin, D.; de Jonge, N. Simulating STEM Imaging of Nanoparticles in Micrometers-Thick Substrates. *Microsc. Microanal.* **2011**, *17*, 980–981.

(100) Otsu, N. A Threshold Selection Method from Gray-Level Histograms. *IEEE Trans. Syst. Man. Cybern.* **1979**, *9*, 62–66.

(101) Lempitsky, V. In *2010 IEEE Computer Society Conference on Computer Vision and Pattern Recognition*, 2010, pp 1197–1204.

(102) In *Table of Integrals, Series, and Products (Seventh Edition)*, Jeffrey, A., Zwillinger, D., Gradshteyn, I. S., Ryzhik, I. M., Eds.; Academic Press: Boston, 2007, pp 247–617.

(103) Kotov, N. A.; Liz-Marzán, L. M.; Weiss, P. S. Chiral Nanostructures: New Twists. *ACS Nano* **2021**, *15*, 12457–12460.

(104) Cho, N. H.; Guerrero-Martínez, A.; Ma, J.; Bals, S.; Kotov, N. A.; Liz-Marzán, L. M.; Nam, K. T. Bioinspired chiral inorganic nanomaterials. *Nat. Rev. Bioeng.* **2023**, *1*, 88–106.

(105) Liu, X.; Du, Y.; Mourdikoudis, S.; Zheng, G.; Wong, K.-Y. Chiral Magnetic Oxide Nanomaterials: Magnetism Meets Chirality. *Adv. Opt. Mater.* **2023**, *11*, 2202859.

(106) Lee, H.-E.; Ahn, H.-Y.; Mun, J.; Lee, Y. Y.; Kim, M.; Cho, N. H.; Chang, K.; Kim, W. S.; Rho, J.; Nam, K. T. Amino-acid- and peptide-directed synthesis of chiral plasmonic gold nanoparticles. *Nature* **2018**, *556*, 360–365.

(107) González-Rubio, G.; Mosquera, J.; Kumar, V.; Pedrazo-Tardajos, A.; Llombart, P.; Solís, D. M.; Lobato, I.; Noya, E. G.; Guerrero-Martínez, A.; Taboada, J. M.; Obelleiro, F.; MacDowell, L. G.; Bals, S.; Liz-Marzán, L. M. Micelle-directed chiral seeded growth on anisotropic gold nanocrystals. *Science* **2020**, *368*, 1472–1477.

(108) Lee, H.-E.; Kim, R. M.; Ahn, H.-Y.; Lee, Y. Y.; Byun, G. H.; Im, S. W.; Mun, J.; Rho, J.; Nam, K. T. Cysteine-encoded chirality evolution in plasmonic rhombic dodecahedral gold nanoparticles. *Nat. Commun.* **2020**, *11*, 263.

(109) Zhuo, X.; Mychinko, M.; Heyvaert, W.; Larios, D.; Obelleiro-Liz, M.; Taboada, J. M.; Bals, S.; Liz-Marzán, L. M. Morphological and Optical Transitions during Micelle-Seeded Chiral Growth on Gold Nanorods. *ACS Nano* **2022**, *16*, 19281–19292.

(110) Ni, B. et al. Chiral Seeded Growth of Gold Nanorods Into Fourfold Twisted Nanoparticles with Plasmonic Optical Activity. *Adv. Mater.* **2023**, *35*, 2208299.

(111) Li, S.; Xu, L.; Ma, W.; Wu, X.; Sun, M.; Kuang, H.; Wang, L.; Kotov, N. A.; Xu, C. Dual-Mode Ultrasensitive Quantification of MicroRNA in Living Cells by Chiroplasmonic Nanopyramids Self-Assembled from Gold and Upconversion Nanoparticles. *J. Am. Chem. Soc.* **2016**, *138*, 306–312.

(112) Kumar, J.; Eraña, H.; López-Martínez, E.; Claes, N.; Martín, V. F.; Solís, D. M.; Bals, S.; Cortajarena, A. L.; Castilla, J.; Liz-Marzán, L. M. Detection of amyloid fibrils in Parkinson's disease using plasmonic chirality. *Proc. Natl. Acad. Sci. U.S.A.* **2018**, *115*, 3225–3230.

(113) Wang, X. et al. Chiral CdSe nanoplatelets as an ultrasensitive probe for lead ion sensing. *Nanoscale* **2019**, *11*, 9327–9334.

(114) Shukla, N.; Bartel, M. A.; Gellman, A. J. Enantioselective Separation on Chiral Au Nanoparticles. *J. Am. Chem. Soc.* **2010**, *132*, 8575–8580.

(115) Gogoi, A.; Mazumder, N.; Konwer, S.; Ranawat, H.; Chen, N.-T.; Zhuo, G.-Y. Enantiomeric Recognition and Separation by Chiral Nanoparticles. *Molecules* **2019**, *24*, 1007.

(116) Sun, X.; Wang, N.; He, Y.; Kong, H.; Yang, H.; Liu, X. Molecule-specific vibration-based chiral differentiation of Raman spectra using cysteine modified gold nanoparticles: the cases of tyrosine and phenylalanine. *J. Mater. Chem. B* **2021**, *9*, 7167–7171.

(117) Li, S.; Liu, J.; Ramesar, N. S.; Heinz, H.; Xu, L.; Xu, C.; Kotov, N. A. Single- and multi-component chiral supraparticles as modular enantioselective catalysts. *Nat. Commun.* **2019**, *10*, 4826.

(118) Zhang, H.; Li, S.; Qu, A.; Hao, C.; Sun, M.; Xu, L.; Xu, C.; Kuang, H. Engineering of chiral nanomaterials for biomimetic catalysis. *Chem. Sci.* **2020**, *11*, 12937–12954.

(119) Wu, F.; Tian, Y.; Luan, X.; Lv, X.; Li, F.; Xu, G.; Niu, W. Synthesis of Chiral Au Nanocrystals with Precise Homochiral Facets for Enantioselective Surface Chemistry. *Nano Lett.* **2022**, *22*, 2915–2922.

(120) Liu, T.; Jin, R.; Yuan, P.; Bai, Y.; Cai, B.; Chen, X. Intracellular Enzyme-Triggered Assembly of Amino Acid-Modified Gold Nanoparticles for Accurate Cancer Therapy with Multimode. *ACS Appl. Mater. Interfaces* **2019**, *11*, 28621–28630.

(121) Zhang, M.; Zhang, H.; Feng, J.; Zhou, Y.; Wang, B. Synergistic chemotherapy, physiotherapy and photothermal therapy against bacterial and biofilms infections through construction of chiral glutamic acid functionalized gold nanobipyramids. *J. Chem. Eng.* **2020**, *393*, 124778.

(122) Li, Y.; Miao, Z.; Shang, Z.; Cai, Y.; Cheng, J.; Xu, X. A Visible- and NIR-Light Responsive Photothermal Therapy Agent by Chirality-Dependent MoO3-x Nanoparticles. *Adv. Funct. Mater.* **2020**, *30*, 1906311.

(123) Ayuso, D.; Neufeld, O.; Ordonez, A. F.; Decleva, P.; Lerner, G.; Cohen, O.; Ivanov, M.; Smirnova, O. Synthetic chiral light for efficient control of chiral light–matter interaction. *Nat. Photon.* **2019**, *13*, 866–871.

(124) Yan, J.; Feng, W.; Kim, J.-Y.; Lu, J.; Kumar, P.; Mu, Z.; Wu, X.; Mao, X.; Kotov, N. A. Self-Assembly of Chiral Nanoparticles into Semiconductor Helices with Tunable near-Infrared Optical Activity. *Chem. Mater.* **2020**, *32*, 476–488.

(125) Spreyer, F.; Mun, J.; Kim, H.; Kim, R. M.; Nam, K. T.; Rho, J.; Zentgraf, T. Second Harmonic Optical Circular Dichroism of Plasmonic Chiral Helicoid-III Nanoparticles. *ACS Photonics* **2022**, *9*, 784–792.

(126) Cho, N. H.; Byun, G. H.; Lim, Y.-C.; Im, S. W.; Kim, H.; Lee, H.-E.; Ahn, H.-Y.; Nam, K. T. Uniform Chiral Gap Synthesis for High Dissymmetry Factor in Single Plasmonic Gold Nanoparticle. *ACS Nano* **2020**, *14*, 3595–3602.

(127) Ma, Y.; Cao, Z.; Hao, J.; Zhou, J.; Yang, Z.; Yang, Y.; Wei, J. Controlled Synthesis of Au Chiral Propellers from Seeded Growth of Au Nanoplates for Chiral Differentiation of Biomolecules. *J. Phys. Chem. C* **2020**, *124*, 24306–24314.

(128) Xu, L. et al. Enantiomer-dependent immunological response to chiral nanoparticles. *Nature* **2022**, *601*, 366–373.

(129) Heyvaert, W.; Pedrazo-Tardajos, A.; Kadu, A.; Claes, N.; González-Rubio, G.; Liz-Marzán, L. M.; Albrecht, W.; Bals, S. Quantification of the Helical Morphology of Chiral Gold Nanorods. *ACS Mater. Lett.* **2022**, *4*, 642–649.

(130) Samet, H.; Tamminen, M. Efficient component labeling of images of arbitrary dimension represented by linear bintrees. *IEEE Trans. Pattern Anal. Mach. Intell.* **1988**, *10*, 579–586.

(131) Zhu, F.-Y.; Wang, Q.-Q.; Zhang, X.-S.; Hu, W.; Zhao, X.; Zhang, H.-X. 3D nanostructure reconstruction based on the SEM imaging principle, and applications. *Nanotechnology* **2014**, *25*, 185705.

(132) Cochran, S.; Medioni, G. 3-D surface description from binocular stereo. *IEEE Trans. Pattern Anal. Machine Intell.* **1992**, *14*, 981–994.

(133) Faugeras, O.; Lustman, F. Motion and structure from motion in a piecewise planar environment. *Int. J. Patt. Recogn. Artif. Intell.* **1988**, *02*, 485–508.

(134) Hartley, R.; Zisserman, A., *Multiple view geometry in computer vision*; Cambridge University Press: Cambridge, UK ; New York, 2000.

(135) Mildenhall, B.; Srinivasan, P. P.; Tancik, M.; Barron, J. T.; Ramamoorthi, R.; Ng, R. NeRF: representing scenes as neural radiance fields for view synthesis. *Commun. ACM* **2021**, *65*, 99–106.

(136) Fridovich-Keil, S.; Yu, A.; Tancik, M.; Chen, Q.; Recht, B.; Kanazawa, A. In *2022 IEEE/CVF Conference on Computer Vision and Pattern Recognition (CVPR)*, IEEE: New Orleans, LA, USA, 2022, pp 5491–5500.

List of Author’s Contribution

Peer-reviewed Publications:

- Gorbanev Y., Engelmann Y., van’t Veer K., Vlasov E., Ndayirinde C., Yi Y., Bals S., Bogaerts A., Al_2O_3-supported transition metals for plasma-catalytic NH_3 synthesis in a DBD plasma: metal activity and insights into mechanisms, *Catalysts* 2021, **11**, 1230.
- Vlasov E., Denisov N., Verbeeck J., Low-cost electron detector for scanning electron microscope, *HardwareX* 2023, **14**, e00413.
- Ndayirinde C., Gorbanev Y., Ciocarlan R.-G., De Meyer R., Smets A., Vlasov E., Bals S., Cool P., Bogaerts A., Plasma-catalytic ammonia synthesis: packed catalysts act as plasma modifiers, *Catalysis Today*, **419**, 114156.
- Vlasov E., Skorikov A., Sánchez-Iglesias A., Liz-Marzán L. M., Verbeeck J., Bals S., Secondary electron induced current in scanning transmission electron microscopy: an alternative way to visualize the morphology of nanoparticles, *ACS Mater. Lett.*, **5**, 1916.
- Ignatova K., Vlasov E., Seddon S., Gauquelin N., Verbeeck J., Wermeille D., Bals S., Hase T., Arnalds U., Phase coexistence induced surface roughness in V_2O_3/Ni magnetic heterostructures (submitted to *APL Mater.*).
- Meng S., Cui Z., Chen Q., Zhang H., Li S., Jafarzadeh A., Neyts E., Vlasov. E, Jenkinson K., *et al.*, Water-promoted C-C coupling reaction in CO_2 hydrogenation for ethanol production through plasma catalysis over Cu_2O/CeO_2 (submitted to *J. Am. Chem. Soc.*).
- Vlasov E., Heyvaert W., Ni B., Van Gordon K., Girod R., Verbeeck J., Liz-Marzán L.M., Bals S. High-throughput morphological chirality quantification of twisted and wrinkled gold nanorods (submitted to *ACS Nano*).

Poster Presentations:

- Vlasov E., Wang D., Verstraelen J., Heyvaert W., Béché A., Verbeeck J., Bals S., *Secondary electron imaging in scanning transmission electron microscopy for material science*, Microscopy Conference (MC 2023), Darmstadt (Germany), February 26 – March 2, 2023.

Acknowledgements

I would like to take this opportunity to express my sincere appreciation to all the people who supported me throughout my PhD journey marked by numerous challenges and moments of enlightenment.

First and foremost, I would like to express my gratitude to my supervisors, Prof. Sara Bals and Prof. Jo Verbeeck for giving me the opportunity to work in a world-class team on this exciting project. I am profoundly grateful for the chance to learn a lot from both of you, professionally and personally. Sara, your support and ability to inspire those around you to advance scientific knowledge have been truly remarkable. I am thankful for your trust in me and the autonomy you granted me in this challenging project. Jo, thank you for dragging me into electronics and for all your help throughout my PhD. Thank you for the long discussions and for all the things I've learnt from you.

I would also like to thank all the people that I have worked with in EMAT during these years, and who helped me in many aspects both professionally and beyond the work environment. It has been a pleasure working alongside each of you and being a contributing member of the team.

Особенно, я хочу выразить благодарность моим друзьям, которые разделяли со мной как трудные, так и радостные моменты за последние четыре с половиной года. Я бесконечно признателен судьбе за то, что вы есть в моей жизни. Кристина, я безмерно благодарен тебе за всю твою доброту, понимание и поддрежку. Я очень ценю нашу дружбу и наши совместные приключения. Мишаня, спасибо за твой здоровый пофигизм и за то, что был со мной «на одной волне» все это время. Юра, спасибо за литры выпитого с тобой пива, бесконечные байки и вкусную комбучу. Некич, спасибо за то, что остаешься настоящим «братом по оружию» со времен бакалавриата. Санёк, Слава, Вика, я признателен вам за то, что несмотря на расстояние, остаетесь со мной рядом.

И в завершение, я хочу выразить глубокую благодарность моим родителям за их неизменную заботу и поддержку. Мама, папа, я благодарен вам за всё, что вы сделали для меня. Спасибо, что воспитали меня в тяге к знаниям и поддерживали меня во всех моих начинаниях. Я вас люблю и безумно скучаю. Ваш Женя.

11.03.2024